Universidade de São Paulo
Instituto de Física

Estudos Teóricos de Captura de CO_2 em Gás Atmosférico por Nanopartículas Porosas

Alexsander Carvalho Vendite

Orientador(a): Prof.(a) Dr.(a) Kaline Coutinho

Dissertação de mestrado apresentada ao Instituto de Física da Universidade de São Paulo, como requisito parcial para a obtenção do título de Mestre(a) em Ciências.

Banca Examinadora:
Prof(a). Dr(a). Kaline Coutinho - Orientador (IFUSP)
Prof(a). Dr(a). Gustavo Roque da Silva Assi (EPUSP)
Prof(a). Dr(a). Thereza Amélia Soares da Silva (UFPE)

São Paulo
2021

FICHA CATALOGRÁFICA
Preparada pelo Serviço de Biblioteca e Informação do Instituto de Física da Universidade de São Paulo

Vendite, Alexsander Carvalho

Estudos teóricos de captura de CO2 em gás atmosférico por nanopartículas porosas / Theoretical studies of the CO2 capture in atmospheric gas by porous nanoparticles. São Paulo, 2021.

Dissertação (Mestrado) – Universidade de São Paulo. Instituto de Física. Depto. de Fisica Geral

Orientador: Profa. Dra. Kaline Rabelo Coutinho
Área de Concentração: Simulações Computacionais e Modelagem Molecular

Unitermos: 1. Física computacional; 2. Dinâmica dos gases; 3. Física molecular.

USP/IF/SBI-035/2021

University de São Paulo
Physics Institute

Theoretical Studies of the CO_2 Capture in Atmospheric Gas by Porous Nanoparticles

Alexsander Carvalho Vendite

Supervisor: Prof. Dr. Kaline Coutinho

Dissertation submitted to the Physics Institute of the University of São Paulo in partial fulfillment of the requirements for the degree of Master of Science.

Examining Committee:
Prof. Dr. Kaline Coutinho - Supervisor (IFUSP)
Prof. Dr. Gustavo Roque da Silva Assi (EPUSP)
Prof. Dr. Thereza Amélia Soares da Silva (UFPE)

São Paulo
2021

Acknowledgments

The current work was realized with support from CNPq, Conselho Nacional de Desenvolvimento Científico e Tecnológico - Brasil. This study was financed in part by the Coordenação de Aperfeiçoamento de Pessoal de Nível Superior - Brasil (CAPES) - Finance Code 001.

I wish to thank the brazilian funding agencies for supporting this work: the fellowship 2019/08465-9 of São Paulo Research Foundation (FAPESP); the grant 2014/50983-3 of FAPESP and 465259/2014-6 of CNPq from the National Institute of Science and Technology Complex Fluids (INCT-FCx); the grant 23038.004630/2014-35 of CAPES from the BioMol project; the grant 2017/11631-2 of FAPESP and Shell and the strategic importance of the support given by ANP (Brazil's National Oil, Natural Gas and Biofuels Agency) through the R&D levy regulation. Additionally, I thank the infrastructure of the Physics Institute of the University of São Paulo (USP) and the High Performance Computing of USP (HPC-USP).

This work was made possible by the resources provided from CNPq, CAPES, FAPESP and Shell, the last two with Grant Numbers 2017/11631-2 and 2019/08465-9, and the strategic importance of the support given by ANP (Brazil's National Oil, Natural Gas and Biofuels Agency) through the R&D levy regulation.

I wish to thank my supervisor, Professor Kaline Coutinho. Her experience and active participation was key on the quality of the work. Also for encouraging me to learn multiple approachings, which secured a solid foundation to my current knowledge.

I would like to thank Professor Thereza Soares for her insight on the work with a fresh perspective and her contribution on the writing of the external publication.

I would like to thank my colleagues Leandro, Matheus, Henrique, Júlio, Danillo, Ricardo, Arthur, Tárcius, Douglas and Thiago for all the provided help and suggestions. And also for their warm reception and companionship.

I would like to thank Denys for his prompt aid as the developer of SuAVE.

I would like to thank Fábio and Valdir for their assistance on the technical issues faced throughout all the work.

I would like to thank Fátima, Bianca, Edineusa and all the staff of IFUSP for their diligent organization and kind treatment.

I would like to thank all of my friends from IFUSP who brigthened my mind with fruitious discussions and happy thoughts. Also for their aid in times of need.

I would like to thank my old friends who provided support and entertainment during the off work time.

I would like to thank Fabiana for her emotional support and guidance when I needed the most.

Lastly, the acknowledgment for my family could not be fully written within this section. They were absolutely imperative on my endurance throughout this work. My most sincere gratitude to them.

I will not bow
I will not falter
To the manipulation of
What they have whispered from centuries ago
The limitation that binds us alone

Vintersea, *Old Ones (2019)*

Theoretical Studies of the CO_2 Capture in Atmospheric Gas by Porous Nanoparticles

Alexsander Carvalho Vendite

Abstract

Global warming is a huge threat for life on Earth and requires vast efforts to be tackled. It emerges mostly from the enhanced greenhouse effect, which has major contribution from atmospheric CO_2. Multiple procedures must be combined to lessen the impact of global warming, such as emission mitigations, development of environmental friendly technologies and atmospheric carbon capture. The theoretical study of the latter is the target of this work. Specifically, when performed by the metal-organic framework ZIF-8 on CO_2, H_2O, N_2, O_2 and Ar under atmospheric conditions. ZIF-8 was considered as a nanoparticle to evaluate how much its surface impacts the gas capture in proportion to the bulk. The surface groups were represented as unsaturated Zn atom, 2-methylimidazole or deprotonated 2-methylimidazole. Those options imply on different values of charge for the ZIF-8 nanoparticle as a whole. The study was heavily structured on molecular simulations, such as Classic Metropolis Monte Carlo, Classic Molecular Dynamics and Born-Oppenheimer Molecular Dynamics. Initially, parametrization of the classic force fields and subsequent validation were performed by electronic structure calculations. Afterwards, O_2 and Ar were found to have negligible interaction with ZIF-8. When considering pristine gases with ZIF-8, the absorption was only possible with CO_2, while the adsorption was dominated by H_2O, followed by CO_2, in energetic magnitude order. In the explicit competition between gases, the CO_2 absorption was greatly decreased when simulated with either H_2O or N_2. The CO_2 adsorption was mostly unchanged by the presence of N_2, while it was inhibited when H_2O was available. Also, both CO_2 uptake and selectivity were enhanced in lower temperatures and higher pressures. The ZIF-8 nanoparticle with more superficial Zn atoms excelled at capturing CO_2. Although it was the nanoparticle with the highest charge, increments of charge made by adding protons to the surface sites had no effect on the CO_2 capture. The effectiveness of ZIF-8 nanoparticles to capture CO_2 decreased as its size grew. From another perspective, absorbed CO_2 was compacted by ZIF-8 similarly to low density liquid CO_2. Additionally, adsorbed CO_2 was structured in a web that resembled solid phase CO_2. Those features highlight the importance of the ZIF-8 surface on the CO_2 capture and its potential to store compacted CO_2. Along with the specific results of gas capture by ZIF-8, this work also aimed to create guidelines on surface conditions treatment of MOFs.

Key-words: Molecular Simulation, CO_2 Capture, Nanomaterial, Electronic Structure, MOFs

Estudos Teóricos de Captura de CO_2 em Gás Atmosférico por Nanopartículas Porosas

Alexsander Carvalho Vendite

Resumo

Aquecimento global é uma enorme ameaça para a vida na Terra e requer extensos esforços para ser abrandado. Este emerge principalmente do intensificamento do efeito estufa, cuja maior contribuição é atribuída ao CO_2 atmosférico. Múltiplos procedimentos precisam ser combinados para aliviar o impacto do aquecimento global, como redução de emissões, desenvolvimento de tecnologias amigáveis com a natureza e captura de carbono atmosférico. O estudo teórico desta última é o objetivo do trabalho. Em especial, quando feita pela MOF chamada ZIF-8 em gases de CO_2, H_2O, N_2, O_2 e Ar sob condições atmosféricas. A ZIF-8 foi construída como uma nanopartícula para avaliar o impacto de sua superfície na captura de gases em proporção com a região interna. Os grupos superficiais foram representados como átomo de Zn insaturado, 2-metilimidazol ou 2-metilimidazol desprotonado. Estas opções implicam em diferentes valores de carga para a nanopartícula de ZIF-8 como um todo. O estudo foi profundamente estruturado em simulações moleculares, como Monte Carlo Metropolis Clássico, Dinâmica Molecular Clássica e Dinâmica Molecular de Born-Oppenheimer. Inicialmente, a parametrização dos campos de força clássicos, com subsequente validação, foram conduzidas por meio de cálculos de estrutura eletrônica. Em seguida, O_2 e Ar demonstraram interação desprezível com a ZIF-8. Ao considerar gases puros com a ZIF-8, a absorção foi possível apenas com CO_2, enquanto que a adsorção foi dominada por H_2O, seguida por CO_2, em ordem de magnitude energética. Na competição explícita entre os gases, a absorção de CO_2 foi fortemente reduzida quando H_2O ou N_2 foram simulados conjuntamente. A adsorção de CO_2 foi apenas levemente afetada pela presença de N_2, enquanto que ela foi inibida quando H_2O estava disponível. Além disso, a captação e a seletividade por CO_2 foram aumentadas sob menores temperaturas ou maiores pressões. A nanopartícula de ZIF-8 com maior número de átomos de Zn superficiais destacou-se na capacidade de captura de CO_2. Apesar de esta ser a nanopartícula de maior carga, incrementos de carga feitos adicionando prótons nos sítios superficiais não demonstraram nenhum efeito na captura de CO_2. A efetividade das nanopartículas de ZIF-8 na captura de CO_2 decaiu conforme seu tamanho aumentava. De outra perspectiva, CO_2 absorvido foi compactado pela ZIF-8 de forma similar à CO_2 em fase líquida de baixa densidade. Além disso, CO_2 adsorvido estruturou-se em uma rede semelhante à CO_2 em estado sólido. Estas observações ressaltam a importância da superfície de ZIF-8 na captura de CO_2 e seu potencial de armazenar CO_2 compactado. Juntamente com os resultados específicos sobre captura de gases pela ZIF-8, o trabalho atual também buscou estabelecer diretrizes no tratamento de superfícies de MOFs.

Palavras-chave: Simulação Molecular, Captura de CO_2, Nanomaterial, Estrutura Eletrônica, MOFs

List of Abbreviations

BECCS	—	Bio-Energy with Carbon Capture and Storage
BOMD	—	Born-Oppenheimer Molecular Dynamics
BSSE	—	Basis Set Superposition Errors
cc-pVDZ	—	Correlation-Consistent Polarized Valence with Double Zeta
CCS	—	Carbon Capture and Storage
CHELPG	—	Charges from Electrostatic Potentials using a Grid-based Method
DAC	—	Direct Air Capture
DFT	—	Density Functional Theory
DIIS	—	Direct Inversion of the Iterative Subspace
DZVP	—	Double Zeta for Valence Electrons plus Polarization
ESA	—	Electrical Swing Adsorption
ESP	—	Electrostatic Potential
GCMC	—	Grand Canonical Monte Carlo
GDIIS	—	Geometry Optimization Using Direct Inversion of the Iterative Subspace
GEDIIS	—	Geometry Optimization Using Energy-represented Direct Inversion of the Iterative Subspace
GGA	—	Generalized-Gradient Approximation
GPW	—	Gaussian and Plane-Wave
GTH	—	Goedecker-Teter-Hutter
HF	—	Hartree-Fock
LCAO	—	Linear Combination of atomic orbitals
LDA	—	Local (Spin) Density Approximation
LINCS	—	Linear Constraint Solver
MC	—	Monte Carlo
MD	—	Classic Molecular Dynamics
MEP	—	Molecular Electrostatic Potential
MOF	—	Metal-Organic Frameworks

MSA — Moisture Swing Adsorption
MSD — Mean Squared Displacement
NET — Negative Emission Technology
PBC — Periodic Boundary Conditions
PBE — Perdew-Burke-Ernzerhof
PSA — Pressure Swing Adsorption
PSCC — Point Source Carbon Capture
PTSA — Pressure and Temperature Hybrid Swing Adsorption
RDF — Radial Distribution Function
RFO — Rational Function Optimization
RMSD — Root-Mean-Square Deviation
SCF — Self-Consistent Field
TSA — Temperature Swing Adsorption
VSA — Vacuum Swing Adsorption
ZIF — Zeolitic Imidazolate Framework
ZIF-8 — Zinc-methylimidazolate Framework-8

List of Figures

List of Tables

Index

1

Introduction

In this chapter the overall conditions of CO_2 in the atmosphere are evaluated. Potential solutions are addressed, which pave the way to the ZIF-8 theoretical approach of the problem.

> *"Every avalanche begins with the movement of a single snowflake, and my hope is to move a snowflake."*
> Thomas Frey

1.1 Global warming

The greenhouse effect is an event which some atmospheric gases absorb infrared radiation and emit it back to the surface of Earth, see Fig. 1.1. This phenomenon is a key factor to understand global warming. It is caused by water vapor, carbon dioxide, methane and other atmospheric gases [1]. Note that the greenhouse effect is fundamental to nurture life in the current ecosystem of Earth, since it maintains heat on its surface. However, the anthropogenic intensification of the greenhouse effect is responsible for devastating environmental problems, such as rise of the water-level in sea, higher number of ocean storms, floods, etc., see Fig. 1.2 [2].

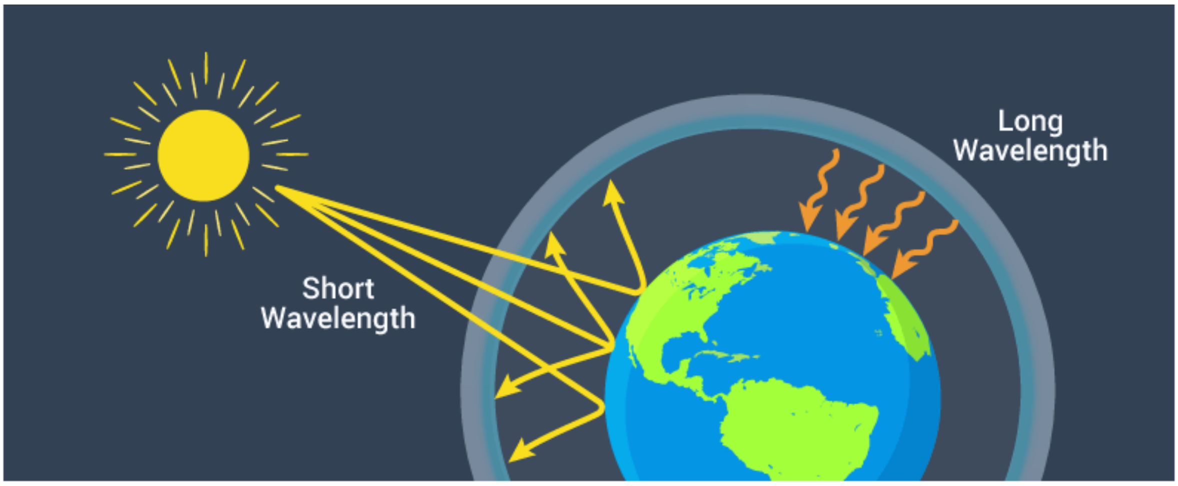

Figure 1.1: Representative diagram of the greenhouse effect – Source: [3]

Atmospheric carbon dioxide (CO_2) is responsible for approximately 55% of the global warming enhancement and for around 64% of the greenhouse effect increase [5, 6]. It should be noted that methane and chlorofluorocarbons (CFC's) pose a higher threat at global warming per mass of gas. However, due to the difference in proportion of the emissions, CO_2 displays a stronger effect [7, 8].

The RCP2.6 projection portrays a concentration of atmospheric CO_2 peaking at 441 ppm by 2050 and reducing to 420 ppm by 2100 [9]. In 2011, it was found that efforts to reduce emissions were underdeveloped and the outlook was considered worse than the expected at 2004 [10]. According to IPCC and within the RPC2.6 scenario, in 2100, the concentration of atmospheric CO_2 may be at 570 ppm [9]. It would cause the global temperature and sea level means to rise by about 1.9 ^oC and 3.8 m, respectively [11, 12]. In a less fortunate perspective, i.e. with the denial to progress towards mitigating emissions, by 2100 the world might be 6 ^oC warmer than in 2009 [13].

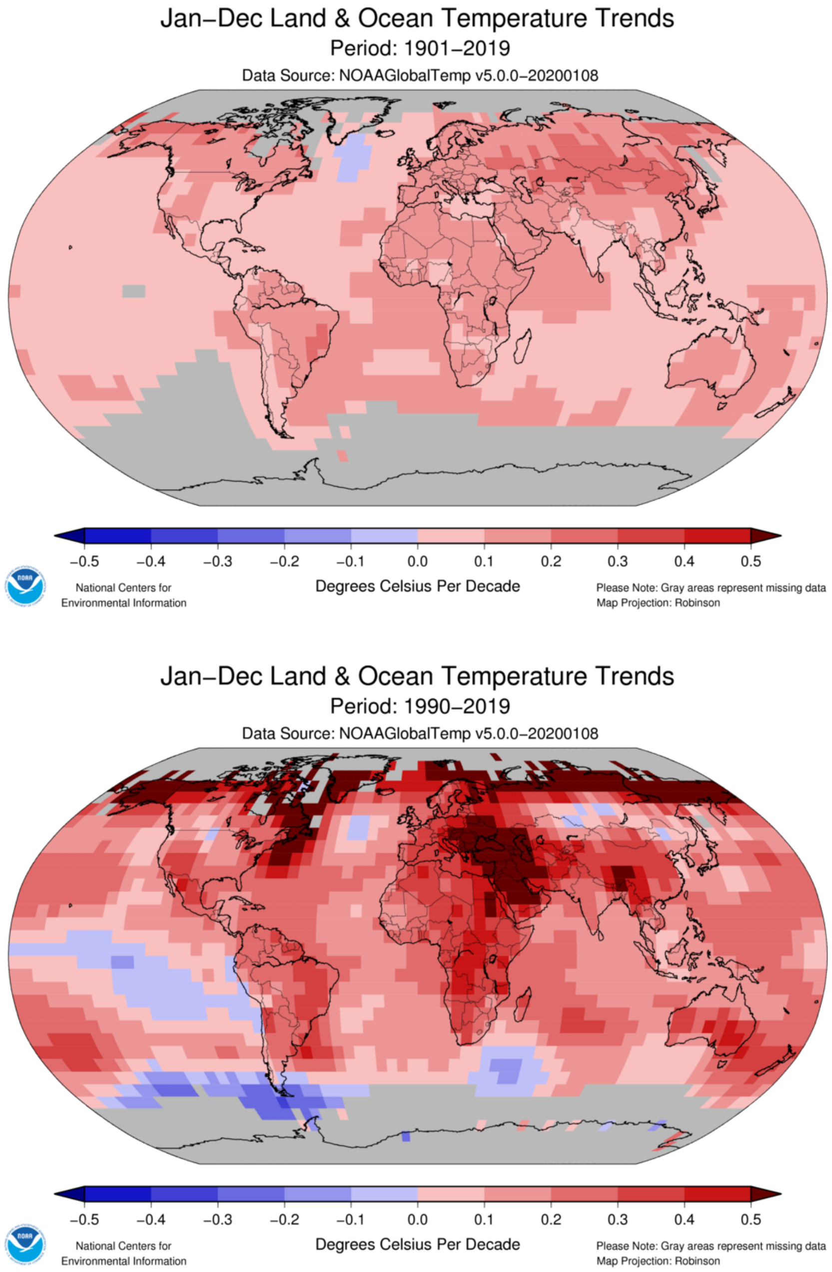

Figure 1.2: Temperature trends per decade around the globe considering different time intervals – Source: [4]

1.1.1 Sources

The increase of atmospheric CO_2 concentration is mostly due to emissions from combustion of fossil fuels, gas flaring, cement production and land use changes, such as deforestation and biomass burning [1]. The industry accounts for almost 40% of worldwide CO_2 emissions, with iron and steel, cement, chemical industries being responsible for 30, 26, 17% of the industrial emissions, respectively [14, 15]. Following closely behind, the fossil fuel power plants contribute to about 30% of worldwide CO_2 emissions [16].

Among all anthropogenic emissions, it is estimated that around 75% of the atmospheric CO_2 increase is due to burning fossil fuels [17]. Theoretically, carbon-free renewable and nuclear energy resources are enough for humankind's energy needs [18]. Therefore, a quick removal of fossil fuels from the power, heat, transportation and industry sectors is required [19–23]. Although a complete exchange for electricity in these sectors would be ideal, it is not readily possible. High temperature industrial heating, long-range aviation and marine transportation are expected to continue using fossil or synthetic fuels until at least 2050 [24]. Also, the cement industry and the non-energetic use of fossil fuels in the chemical industry, such as burning of plastic wastes, would still contribute to climate change [25].

1.2 Atmosphere

The atmospheric conditions considered when determining the constituent gases concentrations are refered to as standard atmosphere. The air is considered dry, as an ideal gas and within the hydrostatics domain. Also, at sea level, with temperature and pressure of 288.15 K and 101325 Pa, respectively. This way, the density and average molar mass are 1225 g/m^3 and 28.964 g/mol, respectively [26].

The five most abundant gases in the standard atmosphere account for almost all of the volume. They are N_2, O_2, Ar, CO_2 and Ne with volume concentrations of 78.084 %, 20.948 %, 0.934 %, 314–391 ppm and 18.18 ppm, respectively [26–30]. Note, however, that CO_2 is addressed within a range, since it is heavily dependent on human activity. Many other pollutants were also emitted, although with concentrations mostly between 1 ppm and 0.01 ppb. Common examples are nitric oxide and ammonia that when in excess can cause serious ambiental imbalances [31–33]. Another important remark is real atmosphere have humidity with 0–4 % of volume concentration depending on many factors [29].

The concentration of atmospheric CO_2 during the pre-industrial era (1750) was about 280 ppm [34–37], which increased to 367 ppm in 1999 [37] and to 379 ppm in 2005 [1]. According to the data of the Scripps CO_2 Program, the atmospheric volume concentration of CO_2 in the vicinity of Mauna Loa is higher than 410 ppm already, see Fig. 1.3 [38].

1.3 CO_2 capture methods

Currently, a wide array of CO_2 capture technologies are being studied. The most prominent ones, without any specific order, are: chemical absorption/adsorption (using amines, aqueous ammonia, Na_2CO_3 systems, zeolites, activated carbon, amine functionalized adsorbents, MOFs and ionic liquids), membrane separation or molecular sieves, carbamation, mineral carbonation, cryogenic separation [39–41].

Considering the chemical adsorption, the capture process relies on selective transition of CO_2 from gas phase to affix itself on an adsorbent material and a posterior regeneration [7]. The regeneration techniques available in the literature are pressure swing adsorption

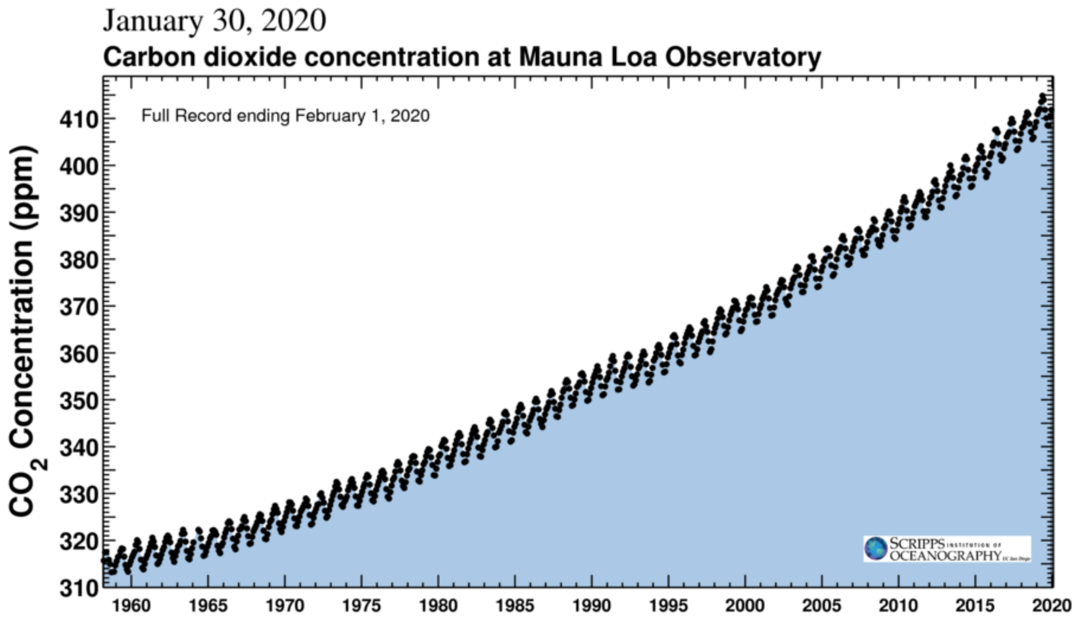

Figure 1.3: Carbon dioxide concentration at Mauna Loa Observatory until Feb/2020. The oscillations are due to natural fluctuations throughout the year – Source: [38]

(PSA), vacuum swing adsorption (VSA), temperature swing adsorption (TSA), electrical swing adsorption (ESA), pressure/temperature hybrid process (PTSA) and moisture swing adsorption (MSA) [7, 8, 42]. PSA consists of a regeneration by reducing the pressure due to a lower gas adsorptivity in the adsorbent material [43]. VSA is similar to PSA, however in the latter, typically the adsorption is done at higher than ambient pressures with the desorption being at ambient pressure. On the other hand, in VSA, the adsorption is usually performed at atmospheric pressure, while the desorption is conducted under lower pressures [7]. TSA is executed by elevating the temperature to reduce the adsoptivity of the adsorbent [43]. ESA is done by passing low voltage electric current through the adsorbent [7]. MSA is also known as washing and relies on the use of water to remove the adsorbed material [24]. Noting that hybrids are combinations of the technologies. Also, ESA costs less than both PSA and TSA, and is believed to be able to make CO_2 capture more cost-effective [44, 45].

In order to mitigate emissions, there are 3 procedures to capture CO_2, mainly at fossil fueled power plants: post-combustion, oxy-combustion and pre-combustion CO_2 captures.

Post-combustion CO_2 capture is the most straightforward method to retrofit in currently working power plants, however its efficiency is quite low. Post-combustion capture relies on the separation of CO_2 from the exhaust gas of fuel combustion [7, 46]. The CO_2 concentration of flue gases from natural gas power plants and from coal power plants contain around 3-5% and 10-15% of CO_2, respectively [47–49].

Oxy-combustion CO_2 capture needs a prior preparation of the air to perform the combustion. It is made in almost pure oxygen instead of atmospheric air, this way the flue gas is composed mostly of CO_2, with NO_x formation being suppressed. Another advantage is that O_2 production and CO_2 separation can be done by physical separation processes [7, 39, 46]. Oxy-combustion requires about half of the energy generation penalty of post-combustion CO_2 capture [7]. Also, oxy-combustion capture is quite promising since it does not demand huge costs for new installations [50].

Pre-combustion CO_2 capture relies on producing carbon-free fuel from fossil fuels. The latter is reacted with oxygen, air or steam, so mostly carbon monoxide and hydrogen are produced. Then, these are reacted with steam to obtain CO_2 and H_2. Finally, CO_2 is collected and H_2 is employed as fuel [7, 39, 46]. Pre-combustion capture is the most cost-efficient among the three methods [50]. However, the initial investment to construct a facility with pre-combustion capture is highly demanding [7].

1.3.1 Negative emission technologies

Point source carbon capture and storage (CCS) are reliable to reduce the CO_2 emissions, but not to halt them completely [51]. Furthermore, point source CCS would not be applicable to ships, planes, land use, agriculture, automobile and other small sources. Which means, emission reductions would not be enough to make a fossil-based system not a polluter [24, 52–54]. Such feat can only be achieved with an exchange of the energy matrix to environmentally cleaner ones and with negative emission technologies (NETs) [55].

The atmospheric CO_2 cannot stay limited below 450 ppm by 2100 if point sources with CCS maintain their emissions at more than 10% of the current rates [56]. Thus, NETs can aid the mitigation efforts to reduce the atmospheric CO_2 concentration peak and enable more economically viable options. However, that cannot be used as an excuse to reduce the development towards mitigation techniques [57, 58]. NETs can be used to avoid the irreversibility of the atmospheric CO_2 concentration increase, yet changes on the climate system due to the strain caused are not evaded [47].

In order to apply the RCP2.6 projection, strict emission reductions should be enforced and NETs implemented by around 2050. The proposition is to employ bio-energy with carbon capture and storage (BECCS), however a wide use of BECCS might negatively affect the food and biodiversity [9].

1.3.2 Direct air capture

Direct air capture (DAC) comprehend a collection of techniques in the NETs with the potential to undertake the food and loss of biodiversity considerations [59, 60]. Another outstanding advantage of DAC is the possibility to tackle emissions from both distributed and point sources [53, 61–63].

The comparison between DAC and point source carbon capture (PSCC) is recurring, although there are important distinctions to be estabilished [24]. PSCC can only diminish the CO_2 emission, while DAC works as a NET [64]. Furthermore, DAC is not location-specific and high concentration of degrading components present in flue gas (SO_x, NO_x, mercury, etc.) are not as prominent [53]. Finally, point source capture must increase the effectiveness, CO_2 capture per volume of processed air, to enhance the sequestration, while DAC just needs efficience, which means reducement of overall costs [63].

DAC was first implemented in the 1930s for cryogenic air separation plants and in life support systems of manned closed systems later on [54, 65, 66]. Such systems dated back to 1965 and were not regenerable [67], yet space shuttles contains regenerable Carbon Dioxide Removal Assembly (CDRA) to keep the inner air breathable [68–70]. The employed methods worked mostly by CO_2 reactions with solutions of strong alkali, such as $NaOH$ and KOH [71]. Unfortunately, those systems are unable to supply highly concentrated streams of CO_2, which would make it exceptionally costly on large scale purposes [24, 54].

An usual source of worry about DAC implementation is the localized exhaustion of CO_2. Also, footprint and land usage might become a problem [24]. An important study regarding that issue was made by analysing the capture potential of a flat sink in a model with 4 x 5^o latitude/longitude resolution. The CO_2 concentration was considered with 5 different scenarios and a three dimensional chemical transport model. The conclusion is that natural CO_2 concentration oscillations are heavier than the DAC depletion potential, hence DAC systems are not prone such issue [72].

DAC was tested with different adsorbents both in controled environments [46, 53, 61, 73, 74] and in a pilot plant [75]. Especially, Metal-organic frameworks (MOFs) were applied in experimental studies with promissing outcomes [74, 76–81].

Currently, a meaninful number of companies are active in the field of CO_2 DAC:

- Carbon Engineering [82] (since 2009) is a pioneer in wide use of high temperature aqueous solution-based DAC;
- Climeworks [83] (since 2009) possess an already solid base on low temperature solid sorbent-based DAC [84–89];
- Global Thermostat [90] (since 2010) is another low temperature DAC company. It has technology suited for CO_2 capture from both atmosphere and point source emissions [91–94];
- Antecy [95] (since 2010) also works on low temperature DAC capture and performs on temperatures of 80-100 ^oC for regeneration;
- Oy Hidrocell Ltd [73, 96] (since 1993) utilizes temperature vacuum swing adsorption (TVSA) at the lowest regeneration temperature among other companies [97, 98];

- Skytree [99, 100] (since 2008) revolves around ESA with moisturising desorption technologies;

- Infinitree [101] (since 2014) administers an ion exchange sorbent material applied to a MSA in order to enrich greenhouses [102–105].

Another decisive concern is regarding the costs of CO_2 capture, more specifically on DAC. A delicate balance to be considered is between the operating cost and the capital cost of the system. To optimize the costs, a minimum layout among both should be established, since they are inversely proportional [106].

Although DAC and point source capture have significant differences, as previously mentioned, the energy required for them can be compared. A general proportion usually agreed upon on the literature is that DAC requires around 3 times more energy than point source capture [47, 58, 107].

It is also estimated that if the CO_2 capture works with 5% of the second-law efficiency, the produced energy by a power plant with natural gas would be entirely consumed on the CO_2 capture [54]. Additionally, the expected efficiency for DAC is already below 10% of the second-law efficiency [58, 63, 106]. Which means, intensive work is required to make DAC commercially viable.

1.4 Applications for captured CO_2

An essential topic to incentivize the viability of CO_2 capture relies on the applications for the obtained gas. A summary of most relevant demands for CO_2 is presented below [73, 108–110].

- Enhanced Oil Recovery: the fossil reservoirs receive compressed CO_2 to provide a more thorough extraction.

- Urea Production: synthetic ammonia and CO_2 are consumed for the industrial production of urea.

- Polymer synthesis and processing: the usual production pathway relies on phosgene. However, the wide use of phosgene goes against the principles of green chemistry and can be replaced by CO_2 [111].

- Fuel and chemical synthesis: CO_2 can be used as a carbon supply to produce a chemical energy carrier from renewable energy sources. Some noteworthy ones are wind and photovoltaic powers, which might provide excess or lack of energy depending on the weather at the time. This way, energy storage can compensate to fulfill the demand [112].

- Biological utilization: planting production can be enhanced by adding extra CO_2 in the atmosphere of a greenhouse.

- Mineralization: carbonates can be used to confine CO_2 for longer periods of time. Carbonates barely enhance the overall value, yet they can be useful as building materials and soil amendments.

- Integrated biorefinery: the processes of ethanolic fermentation and biologic production of succinic acid can be coupled. The first emit CO_2 while the latter consumes it [113].

A more in-depth viewpoint of the state of the art in CO_2 utilization can easily be found in the literature [107, 108, 114–118].

1.5 Advantages of MOFs

When pursuing qualified adsorbent candidates, a broad array of traits should be considered. The most important ones are large CO_2 adsorption capacity, large surface area, rapid kinetics, large CO_2 selectivity, cheap regeneration conditions, stability through the capture process, tolerance to impurities, availability of tunable properties and low production cost [119].

Considering the aforementioned needed traits, Metal Organic Frameworks (MOFs), see Fig. 1.4, are regarded as highly promissing for CO_2 capture due to:

- Exceptionally large surface area, both pore structures and pore surface properties can be modified [39, 42, 120, 121];

- Versatility [53];

- Phenomenal prospects for researching grounds [55, 62, 121–125];

- Outstandingly positive outcomes regarding capture capacity, selectivity, recyclability, pore functionalization, pore size, pore shape, regeneration, stability and adsorbing kinetics [126–144];

- Promising CO_2 capture for ambients with high or intermediate CO_2 concentration [39, 76, 128, 136, 138–143, 145–147].

A quality of MOFs that deserves exclusive attention is the presence of open metal sites or coordinated unsaturated metal sites, see Fig. 1.5, [147, 148]. Those sites can incorporate extra reactivity [53], selective capture of carbon with reversible binding [55], increased CO_2 uptake capacity and selectivity [62]. Additionally, the localized charges of open metal sites are exceptionally effective when interacting with the quadrupole of CO_2 molecules [149].

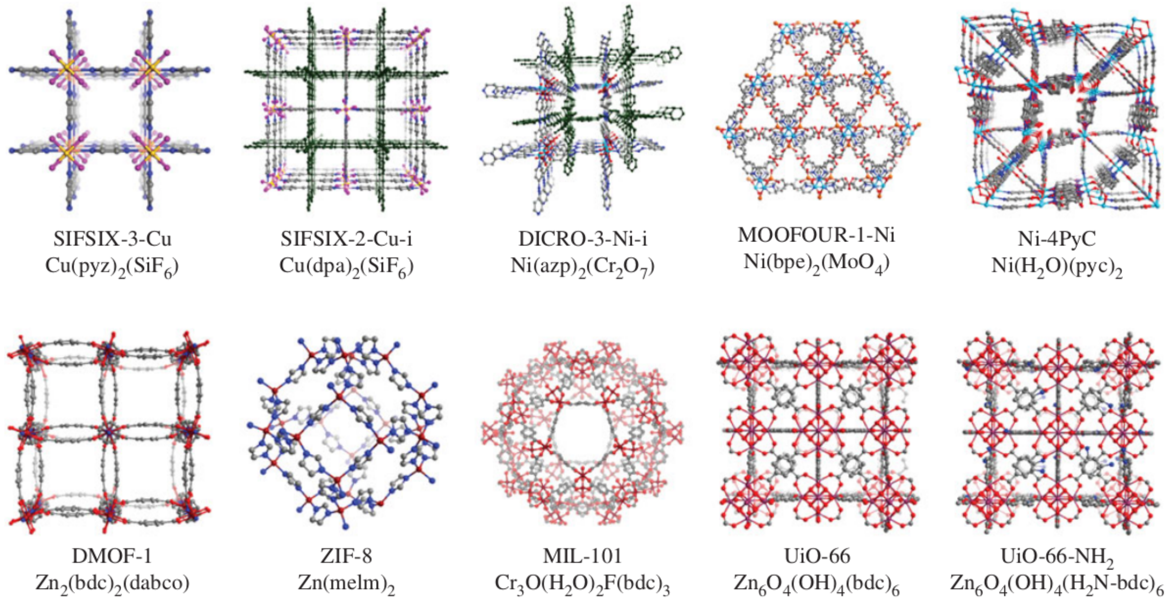

Figure 1.4: Molecular diagrams of a wide array of MOFs – Source: [77]

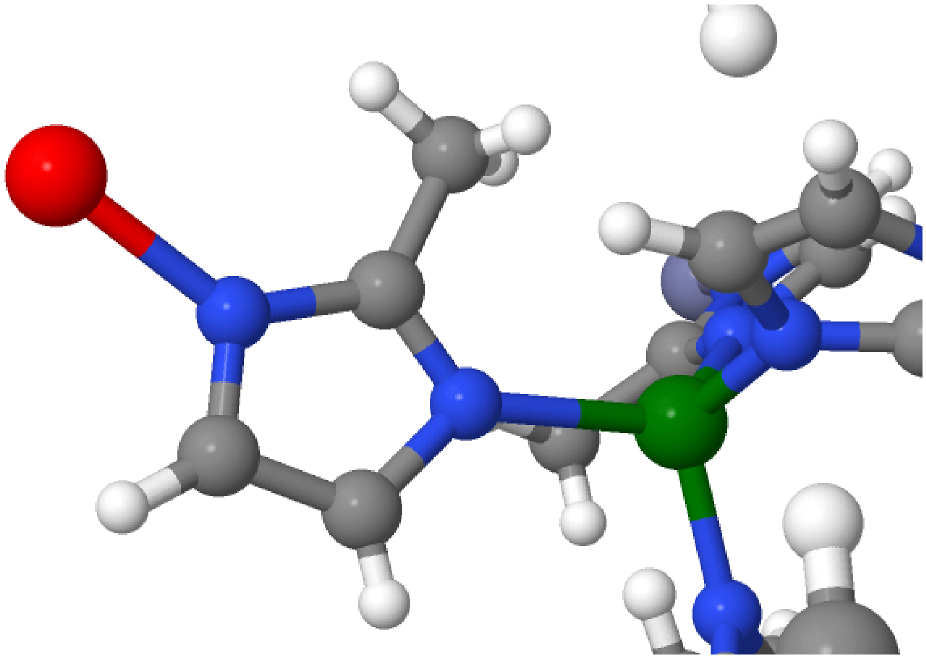

Figure 1.5: Molecular diagram of undercoordinated metal atom, in red, and a fully coordinated metal atom, in green, of ZIF-8

1.6 General results for CO_2 capture with different adsorbents

Several experimental results of adsorbents interacting with components of the atmosphere, especially CO_2, are available within the scientific literature. Concerning adsorbents in general, it was found that both the presence of H_2O and higher temperatures usually reduce the CO_2 uptake [74, 150].

1.6.1 Capture potential of MOFs

Narrowing the scope to MOFs only, H_2O reduces the CO_2 uptake in the majority of tests [39, 53, 62, 126] with rare exceptions [78]. Exposure to H_2O can even degrade the considered MOF [151, 152]. Higher temperatures also reduce the adsorption capacity of CO_2 [39, 153]. Impurities such as NO_x and SO_x can be damaging to the structure of the MOF [39]. Open metal sites strongly empower the CO_2 capture performance [79, 80, 126], however they bind preferentially and strongly with H_2O instead of CO_2 [126]. In-depth reviews providing an outlook on the CO_2 capture by MOFs are available as well [55, 154].

Glier et al. [155] provided a real setting assessment of post-combustion CO_2 capture based on functionalized amines and MOFs. Base plant considerations and process cost were evaluated and applied on a case study. It concluded that both types of solid sorbents are potential alternatives to liquid systems. Sinha et al. [156] addressed DAC design by two MOFs as adsorbents along with an economic analysis. The process is performed by temperature vacuum swing adsorption (TVSA) with energy requirements and cost estimatives. Both studies aimed to demonstrate the feasibility of CO_2 capture by MOFs when dealing with flue and atmospheric gases.

1.6.2 ZIF-8: CO_2 capture potential and stability

ZIF, zeolitic imidazolate framework, is a class of MOF usually constituted by tetrahedral units which accommodate one divalent transition metal and four imidazolate anions [157, 158]. ZIFs have remarkable thermal and chemical stability [159–161] and favorable CO_2 adsorption properties [154]. Also, unless the imidazole linkers of ZIFs are bonded with hydrophilic groups, ZIFs are innately hydrophobic, which greatly aids the CO_2 capture [162–164].

One extensively studied ZIF on selectivity of atmospheric gases is the ZIF-8 [141], or zincmethylimidazolate framework-8, see Fig. 1.6. ZIF-8 was found to be an exceptional canditate for CO_2 capture [165–168], CO_2 storage [169] and for DAC of CO_2 [77]. The structural stability of ZIF-8 was intensely studied due to apparently conflicting results [141, 157, 170, 171]. Different studies conducted with ZIF-8 observed stability in boiling water for 7 days [157] and reasonable stability in pure water for the same period of time [172]. On the other hand, instability was observed when storing ZIF-8 in water at 323 K for a day and in pure water for a year [172, 173]. Later, it was found that ZIF-8 kept the structure in water for a day at 353 K when the ZIF-8/H_2O ratio was 6.0 wt % but totally dissolved when that ratio was 0.060 wt % [174]. Finally, it was concluded that ZIF-8, CO_2 and H_2O react to form a complex carbonate [175]. This way, the stability of ZIF-8 in boiling water was due to low solubility of CO_2 in water at high temperatures. At room temperature, however, the solubility is superior and the reaction happens at a faster rate. Which means, the inlet gas must be dehydrated before ZIF-8 is exposed to it.

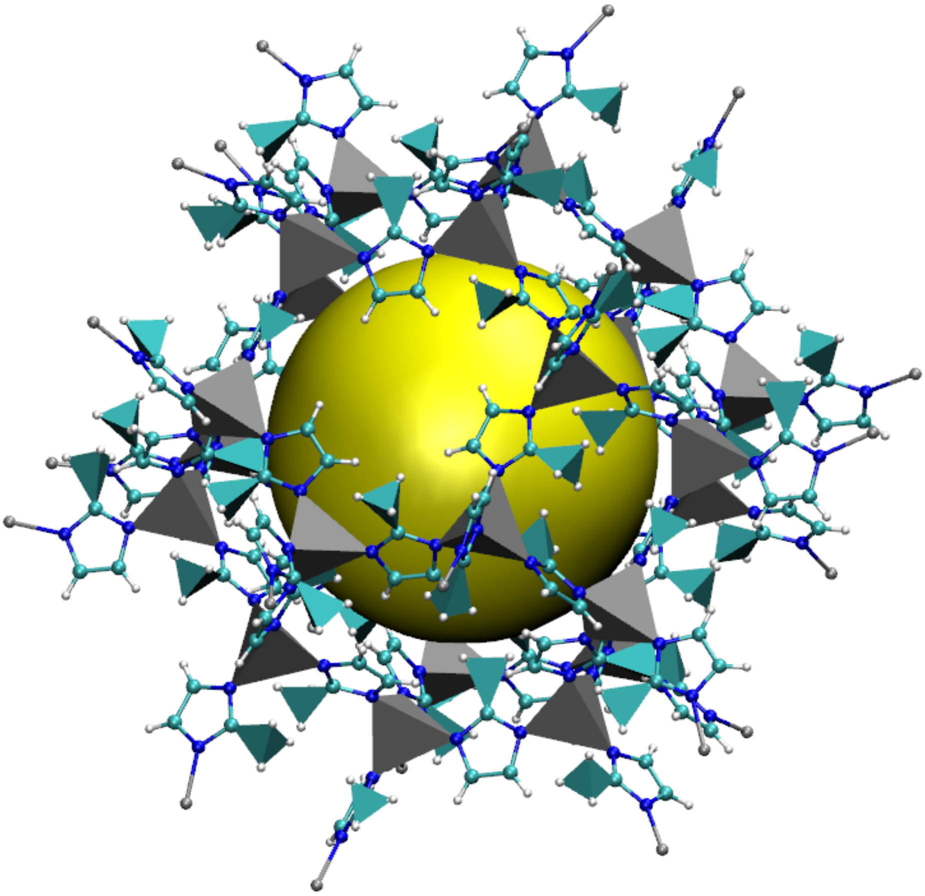

Figure 1.6: Molecular diagram of a ZIF-8 unit cell with Zn terminations

ZIF-8 exhibits stability in a rather diverse set of environments such as refluxing organic solvents and aqueous alkaline solutions [157]. ZIF-8 is susceptible to deterioration in acidic media [157, 176]. Remarkably, the bulk of ZIF-8 nanoparticles displayed stability when exposed to dilute solutions of aqueous SO_2 [177]. However, the surface suffered roughening and degradation. Cubic nanoparticles underwent a less intense degradation than the rhombic dodecahedra nanoparticles. The cubic structure presented superior stability due to smaller pores.

1.6.3 Simulations of CO_2 capture with ZIF-8

The theoretical literature with simulations about capture of atmospheric gases with ZIF-8 is abundant. The methods considered are Grand Canonical Monte Carlo (GCMC), with a rigid structure, Molecular Dynamics (MD), with a flexible structure, and GCMC/MD hybrids. Also, periodic boundaries on three dimensions and temperatures around 273 K were extensively used. The absorption sites for CO_2 on the bulk of ZIF-8 are close to the organic imidazolate group[166, 178], especially near the imidazolate rings and above the three methyl rings [179], proximal to the $C = C$ bond and in the cage center [180], near the H atoms [181], and on both sides of the six ring windows and above the four ring windows [182]. It was identified, in concordance with the experimental data, that the absorption amount of CO_2 increases with the pressure [179, 180, 183–186], decreases with an increase of temperature [184] and is higher than the N_2 amount [166]. Similarly, N_2, H_2O, O_2, CO_2/N_2 and CO_2/CH_4 absorptions increase with the pressure [184–187], however bulky absorption of H_2O only happens at high pressures [188]. The CO_2 selectivity and CO_2/N_2 separation were unaffected by the presence of O_2, H_2O or SO_2 [185], however higher CO_2/N_2 separation was observed on lower temperatures [178]. Furthermore, the CO_2/CH_4, CO_2/N_2, CO_2/H_2 selectivities towards CO_2 grew with the pressure [180, 183, 186, 187]. Also, the CO_2/CH_4 selectivity is dependent on the H_2O ratio and temperature [165]. Computational simulations indicate that the structural flexibility of bulky ZIF-8 grants a gate opening of the ZIF-8 windows, however only at high pressures with CO_2 or CO_2/N_2 [178, 189]. Overall, the structural flexibility displays an insignificant effect on absorption, although fundamental for the diffusion [165, 168, 180], especially when the pore window is smaller than the diffusing molecule [190]. The diffusivities of CO_2, pristine and at CO_2/CH_4, barely change with the pressure and the CO_2 diffusitivity in CO_2/CH_4 is similar to pristine CO_2 [180]. The mean residence time of CO_2 molecules inside of bulky ZIF-8 increases at higher pressures and lower temperatures [182]. Less commonly, force fields parameters for Classic Molecular Dynamics were developed with Born-Oppenheimer Molecular Dynamics (BOMD) [191].

Although multiple theoretical works are available regarding ZIF-8, there is a particular facet that is mostly disregarded: the superficial conditions of ZIF-8, which is the contrasting feature of the current work. There is one work that drifted from the usual method with a partially flexible GCMC of ZIF-8 [192]. ZIF-8 was represented both as a periodic bulk and as a nanoparticle. The neutral nanoparticle was constructed as a sphere, of 5 nm of diameter and about 3000 atoms, with undercoordinated Zn atoms terminated in imidazoles and all exposed N atoms protonated or with a hydroxyl group. The simulations have shown that non degenerative structural transition of ZIF-8 happens at a higher pressure in the bulk than in the nanoparticle and did not depend on the considered nanoparticle surface, however the model depends on the particle size.

1.6.4 Surface conditions of ZIF-8

The reported computational efforts were applied towards the bulk structure of ZIF-8, with few exceptions [192], while surface composition, surface structure and morphology of the ZIF-8 nanoparticles were mostly neglected. Yet, experimental studies draw attention to the effects of the aforementioned conditions of ZIF-8 nanoparticles on structural stability, adsorbate upload and diffusion rates, and surface reactivity [175, 177, 193–195], which means, a proper description of the nanoparticles surface lays the foundation to fully understand the interaction between ZIF-8 and the atmospheric gases.

Regarding the first topic, surface composition, there are many reported compositions for ZIF-8 nanoparticles. The values, in wt %, mainly revolve around 42.0 for C, 4.5 for H and 24.0 for N, with small deviations depending on the experimental conditions. However, the Zn proportion present more relevant deviations, with reported values within the range of 22-30 wt%. Which means that structures of ZIF-8 can be synthesized with different ratios of metal sites [176, 196–199]. There are also indications of O atoms in the structure, albeit in small proportions [193, 197].

Concerning the surface structure, a decisive factor in CO_2 capture is the presence of undercoordinated Zn atoms on the surface, mostly with 2 or 3 bonds [193, 197, 199–201]. In a work, nanoparticles of ZIF-8 were fully covered by an Au layer with a surfactant mediating the interaction [199]. The surfactant could only bond to dicoordinated Zn atoms. Thus, many dicoordinated Zn atoms were available on the surface to enable the coating. Hence, the variations in wt % ratio of Zn atoms might be related to the size of the nanoparticles, proportion between surface and bulk, and/or the terminations provided by the synthesis method. The presence of the following groups were identified on the surface of ZIF-8: undercoordinated Zn atoms, hydroxyl groups, NH groups, N^- sites, ZnO, molecular water and hydrogencarbonates [176, 193, 197, 199–201]. Such wide variety is achieved due to the high reactivity of the surface groups with H_2O and its dissociated products, OH^- and H^+, and with H_2CO_3. Similarly, a reaction can happen with fully coordinated amine to generate ammonium groups [176]. If the pH of the aqueous solvent with the ZIF-8 nanoparticle is lower than 9.6, then the zeta potential of the nanoparticle surface is positive [176]. Thus, in a neutral setting, the nanoparticle is expected to be positively charged or neutral.

Depending on the experimental procedure, the ZIF-8 nanoparticle is assembled in one of the following morphologies: cubic, with 6 (100) faces, rhombic dodecahedric, with 12 (110) faces, or truncated rhombic dodecahedric, with 6 (100) and 12 (110) faces [202]. Also, the theoretical surface density of unsaturated Zn atoms on the face (100) is higher than on the face (110) [199].

1.7 Molecular level considerations

Newcoming CO_2 separation technologies ought to mind the selectivity towards CO_2, since it is a vital aspect. High selectivity is desirable to perform an intense CO_2 separation. The interaction between CO_2 and the adsorbent is pressing to ensure effective capture. On the other hand, fierce interaction energy would culminate in high costs on desorption [55].

CO_2 can behave both as Lewis acid and basis [203]. This way, CO_2 can interact with negative and positive charges, by approximating the C atom or one of the O atoms, respectively [204, 205]. Those interactions can be seen as a side-on or an end-on geometries, correspondingly. According to experiments and calculations [206, 207], the CO_2 adsorption is organized in an intricate structure by both interactions simultaneously. It is constructed with interactions of CO_2-adsorbent and of CO_2-CO_2, which portrays the complexity of the formed fabric [208].

1.7.1 Importance of computational simulations

Amidst the scientific community, a few authors still frown upon the importance of computational simulations. In order to reassure those potential doubts, the following information is provided. Detailed nanoscopic information, inaccessible or hardly obtainable through experiments, can be achieved with computational analyses [209–211]. Also, simulations can restrain a wide list of potential candidates to guide future experimental explorations [212].

Nevertheless, to attain the aforementioned through classical means, a parametrization of the system must be conducted. Among the force field parameters, the determination of atomic charges constitute a large field of research. Regarding MOFs, several procedures are available, yet the most popular kinds are electrostatic potential (ESP) such as CHELPG. It relies on fitting a set of point charges centralized on each atomic nuclei to mirror an ab initio calculated ESP on the best way possible [55].

It is possible to study MOFs with quantum chemical simulations, which would remove the need of parametrization, however, feasible only with smaller fragments. Due to the high amount of atoms in the structure of MOFs, the literature is scarce of quantum chemical simulations with MOFs [208].

1.8 My contribution

In this work, the surface composition of ZIF-8 and its effect on the spontaneous diffusion of atmospheric gases (N_2, O_2, H_2O, Ar and CO_2) are studied through theoretical means. Simulations by Metropolis Monte Carlo (MC), Molecular Dynamics (MD) and an ab initio method named Born-Oppenheimer Molecular Dynamics (BOMD) were performed along with electronic structure calculations. ZIF-8 was studied as a nanoparticle to evaluate its surface effect on the gas capture, see Fig. 1.7. The study started by performing an atomic charge parametrization of ZIF-8 followed by a confrontation between the results from classic and ab initio methods to evaluate its quality. Note that force field parameters of ZIF-8 had already been obtained in the literature, however only for the bulk region. Then, different systems were considered to survey the impact from surface conditions, temperature, pressure, nanoparticle size and charge, and gas mixtures.

Additionally, tests with pristine CO_2 were carried out to compare its behavior with the adsorbed CO_2. It is expected to provide not only information about ZIF-8 but also to aid enlightening the path to approach other MOFs on similar feats.

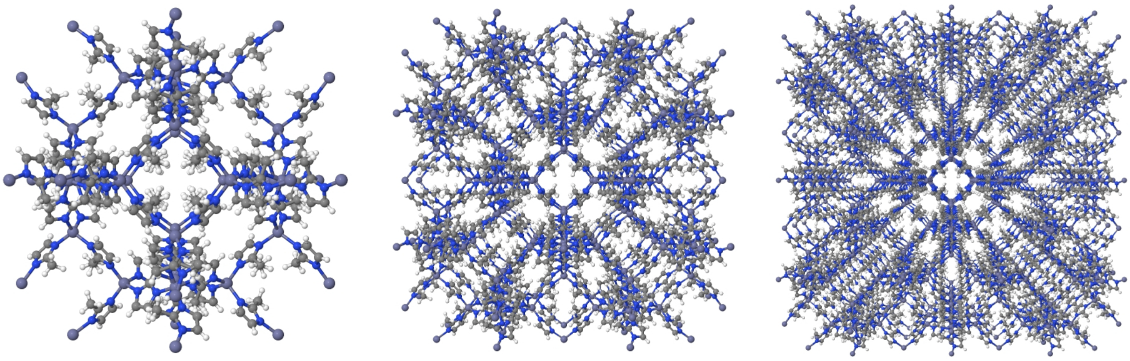

Figure 1.7: Structural model of ZIF-8 as 1x1x1, 2x2x2 and 3x3x3 packing nanoparticles

1.9 Summary of the next chapters

The following sections of this work start by describing the theory behind applied methods in the Chapter 2. It begins with Metropolis Monte Carlo (MC), in Section 2.1, and delves into relevant content for molecular simulations, such as ensembles, potential force field and periodic boundary conditions. Classical Molecular Dynamics (MD), in Section 2.2, are also described through the leap frog algorithm. Other peculiarities such as constraints and thermostat are adressed as well. At this point, the classical methods are concluded and another simulation procedure is looked into, Born-Oppenheimer Molecular Dynamics (BOMD) in Section 2.3. It depends on strict technical theory and is explored in a more superficial manner, just enough to understand its main concepts. The last major method is regarding Electronic Structure Calculations in Section 2.4. Its theory was partially described in the previous topic, so only the remaining parts had to be checked. The focus was aimed at geometry relaxation, charge calculations and binding energy evaluations. A small Section 2.5 finishes the theory with analysis methods, such as radial distribution function and diffusion coefficient.

The applied methodology is described in Chapter 3. It begins by exploring the simulation parameters in Section 3.1. The simulations performed are listed in the Section 3.2. Then, the electronic structure calculations approached are described in the Section 3.3. The relation of which systems were simulated for each result section is described in the Section 3.4. The criteria for captured gas molecules are defined in the Section 3.5.1. Other analysis methodologies, free volume and CO_2 diffusion coefficient calculations, were approached in Sections 3.5.2 and 3.5.3.

Moving on, the results are addressed in Chapter 4. It begins by developing the MC atomic charge parametrization, in Section 4.1, for the following simulations. Some tests were conducted to represent the intended atmospheric environment in a simulation box in Section 4.2. The MC force field parameters were validated by comparison of the interaction distances and energies in Section 4.3. With the basis for MC simulations, their results are discussed regarding the most abundant atmospheric gases and different values of temperature and pressure in Section 4.4. Then, different surface conditions for ZIF-8 were considered and compared among each other in Section 4.5. Up to this point, the MC simulations were employed, however were lacking on specific facets of the problem at hand. Then, parametrization for MD were performed in Section 4.6. Classical methodologies were combined to assess gas mixtures, densities of CO_2, both captured and pristine, and different ZIF-8 nanoparticle framework sizes in Sections 4.7 to 4.9. The time trajetory from MD enabled the study of dynamic quantities, such as CO_2 diffusivity and gas absorption characteristic times in Sections 4.10 and 4.11. Finally, the adsorbed CO_2 structure is checked in Section 4.12.

A summary of the found results are coupled with final discussions to conclude the work in Chapter 5.

2

Methods

In this chapter the theoretical basis used in the current work is on the spotlight. The Metropolis Monte Carlo, Classic Molecular Dynamics, Born-Oppenheimer Molecular Dynamics and Electronic Structure Calculations are the main focus. Their fundamental concepts and nuances relevant for this work are detailed.

> *"The whole point of getting things done is knowing what to leave undone."*
> Oswald Chambers

An immense variety of molecular simulations and calculation methods are available within the scientific literature. Among all options, Monte Carlo Metropolis, Classic Molecular Dynamics, Born-Oppenheimer Molecular Dynamics and Electronic Structure Calculations were employed in this work.

Different approaches were purposely chosen since representation and study of MOFs compose a complex field. Surface conditions, bulk composition, nanoparticle size and charge, interacting gases are all fundamental variables which must converge to compatible results through different methods. Ab initio procedures are important to construct a solid parametrization. While classic methods can enhance the size and diversity of the system due to its lower computational cost. Regarding the classic simulations, both theories excel at different areas. Dynamics provide a trajectory with time sequence and natural framework flexibility, while Monte Carlo disregards the potential barrier heights and allows good sampling of pressure-fixed simulations of gases.

The concepts behind the aforementioned theories are explained below.

2.1 Monte Carlo method

2.1.1 Metropolis algorithm

One objective of molecular simulations with great importance is to obtain the average of an observable A defined by Eq. 2.1.1 [213, 214].

$$\langle A_{total} \rangle = \frac{\int d\mathbf{p}^N d\mathbf{r}^N A(\mathbf{p}^N, \mathbf{r}^N) exp[-\beta \mathscr{H}(\mathbf{p}^N, \mathbf{r}^N)]}{\int d\mathbf{p}^N d\mathbf{r}^N exp[-\beta \mathscr{H}(\mathbf{p}^N, \mathbf{r}^N)]} \tag{2.1.1}$$

where $\mathbf{r}^N$ and $\mathbf{p}^N$ represent coordinates and momenta, respectively, of N particles, $\mathscr{H}(\mathbf{p}^N, \mathbf{r}^N)$ is the system Hamiltonian, $\beta = 1/k_B T$ with k_B being the Boltzmann constant and T the temperature.

The kinetic part of $\mathscr{H}$ depends quadratically on the momenta and its integral can be calculated analytically. However, the dependence on $\mathbf{r}^N$ can rarely ever be exactly integrated. Thus, numerical methods must be employed.

The average of A is evaluated on a multidimensional system and usual numerical integration methods, such as quadratures, become useless rapidly as the dimensionality grows. The reason is that taking m equidistant points in each axis would result in m^α calculations, with α being the dimension. Since the exponential function to be integrated in Eq. 2.1.1, the Boltzmann factor, varies rapidly, a tight mesh would be required. One way to address this issue is to exchange the homogeneous sampling procedure to an importance based one named Metropolis Monte Carlo [215]. The concept of importance sampling relies on considering many points in the region of reasonable Boltzmann factor and only a few elsewhere.

The problem being faced mainly revolves around expressions such as Eq. 2.1.2.

$$\langle A_{conformational} \rangle = \frac{\int d\mathbf{r}^N A(\mathbf{r}^N) exp[-\beta \mathscr{U}(\mathbf{r}^N)]}{\int d\mathbf{r}^N exp[-\beta \mathscr{U}(\mathbf{r}^N)]} \tag{2.1.2}$$

Let us denote the partition function Z by Eq. 2.1.3 and the probability density $\mathscr{N}(\mathbf{r}^N)$ by Eq. 2.1.4.

$$Z \equiv \int d\mathbf{r}^N exp[-\beta \mathscr{U}(\mathbf{r}^N)] \tag{2.1.3}$$

$$\mathscr{N}(\mathbf{r}^N) \equiv \frac{exp[-\beta \mathscr{U}(\mathbf{r}^N)]}{Z} \tag{2.1.4}$$

This way, the expression 2.1.2 can be rewritten as Eq. 2.1.5.

$$\langle A_{conformational} \rangle = \int d\mathbf{r}^N \mathscr{N}(\mathbf{r}^N) A(\mathbf{r}^N) \tag{2.1.5}$$

Generating points in configurational space following $\mathscr{N}(\mathbf{r}^N)$ would result in Eq. 2.1.6.

$$\mathscr{N}(\mathbf{r}_i^N) \approx \frac{n_i}{L} \tag{2.1.6}$$

where n_i is the number of points generated around $\mathbf{r}_i^N$ and L is the total generated points. Then , $\langle A \rangle$ can be calculated as Eq. 2.1.7.

$$\langle A \rangle \approx \frac{1}{L} \sum_{i=1}^{L} n_i A(\mathbf{r}_i^N) \tag{2.1.7}$$

The Metropolis scheme is then used to generate the points in the configurational space proportionally to $\mathscr{N}(\mathbf{r}^N)$. It is done through a Markov Chain by preparing a system configuration $\mathbf{r}^N$ denoted 'old'. Next, a small random displacement δ is applied in 'old' to obtain a trial one $\mathbf{r}'^N$ named 'new'. Consider the transition probability for the system to go from 'old' to 'new' as $\pi(old \longrightarrow new)$. An important constraint to ensure that the equilibrium is maintained once reached is the detailed balance, formulated in Eq. 2.1.8.

$$\mathscr{N}(old)\pi(old \longrightarrow new) = \mathscr{N}(new)\pi(new \longrightarrow old) \tag{2.1.8}$$

Each Monte Carlo move is made in 2 steps: conduct a trial move from 'old' to 'new'; acceptance, or not, of the move. The first is encoded by the transition matrix $\alpha(old \longrightarrow new)$ and the latter is denoted by the probability of acceptance $acc(old \longrightarrow new)$. Then, the transition probability $\pi(old \longrightarrow new)$ is obtained by the product of both, which means Eq. 2.1.9.

$$\begin{aligned}\mathscr{N}(old)\alpha(old \longrightarrow new) \times acc(old \longrightarrow new) = \mathscr{N}(new)\alpha(new \longrightarrow old) \\ \times\, acc(new \longrightarrow old)\end{aligned} \tag{2.1.9}$$

By the Metropolis method, α is chosen as symmetric, which means it follows Eq. 2.1.10.

$$\alpha(old \longrightarrow new) = \alpha(new \longrightarrow old) \tag{2.1.10}$$

Then, eqs. 2.1.9 and 2.1.4 can be rewritten as Eq. 2.1.11.

$$\frac{acc(old \longrightarrow new)}{acc(new \longrightarrow old)} = \frac{\mathscr{N}(new)}{\mathscr{N}(old)} = exp\{-\beta[\mathscr{U}(new) - \mathscr{U}(old)]\} \tag{2.1.11}$$

Which is solved by the choice of Metropolis *et al.* as Eq. 2.1.12.

$$\begin{aligned} acc(old \longrightarrow new) &= \mathscr{N}(new)/\mathscr{N}(old) \quad && if\ \mathscr{N}(new) < \mathscr{N}(old) \\ &= 1 && if\ \mathscr{N}(new) \geq \mathscr{N}(old) \end{aligned} \tag{2.1.12}$$

With eqs. 2.1.12 and 2.1.11, the probability of accepting the trial move is achieved as Eq. 2.1.13.

$$acc(old \longrightarrow new) = min\left(1, exp\{-\beta[\mathscr{U}(\mathbf{r}'^N) - \mathscr{U}(\mathbf{r}^N)]\}\right) \tag{2.1.13}$$

Lastly, the trial moves should be made in a way that guarantee the symmetry of α, which means a reverse trial move must be equally probable. In a rigid setting, each trial move consists of a translational and an orientational displacements. The translational trial moves were performed by adding a small uniformly distributed random value in the interval $[-\Delta/2, \Delta/2]$ for each of the coordinates x, y and z. The orientational trial moves were done by randomly generating an axis and applying a small, and random as well, angular displacement around it.

In this work the simulation length was measured by Monte Carlo cycles. One molecule of the system is randomly chosen, it undergoes through a translational and an orientational trial move, it is accepted or not based on the Boltzmann factor, then the process starts over with the other molecules until all were tried. Then, one Monte Carlo cycle is accounted.

2.1.2 Ensembles

The choice of ensembles is important since distinct ensembles are only guaranteed to yield same results in the thermodynamic limit. Plain Monte Carlo simulations sample the canonical ensemble, i.e., NVT ensemble. In that case the probability of acceptance follows Eq. 2.1.13.

Since the objective of this work is to perform DAC, it is of interest to evaluate the system under constant pressure as well. Thus, the isobaric-isothermal ensemble, i.e. NPT, is detailed below. Under those circumstances, the probability of finding a specific configuration of the N atoms with constant pressure P at a volume V is proportional to Eq. 2.1.14 [213, 214].

$$\mathscr{N}(\mathbf{r}^N, V) \propto exp\{-\beta[\mathscr{U}(\mathbf{r}^N, V) + PV]\} \tag{2.1.14}$$

In the NPT Monte Carlo procedure, V undergoes trial moves the same way as the coordinates $\mathbf{r}$. In that case, the volume is attempted to change as $V' = V + \Delta V$, where ΔV is chosen randomly. Note that trial could create an artificial vacuum region when $\Delta V > 0$ and expel molecules when $\Delta V < 0$. To avoid it, the coordinates $\mathbf{r}^N$ must be multiplied by $(V'/V)^{1/3}$, considering a cubic lattice, which generates $\mathbf{r}'^N$. When $\mathscr{N}$ is integrated to be normalized, a new term arises. The acceptance probability, calculated by 2.1.12, becomes Eq. 2.1.15.

$$\begin{split} acc(old \longrightarrow new) = min(1, exp\{-\beta[\mathscr{U}(\mathbf{r}'^N, V') - \mathscr{U}(\mathbf{r}^N, V) \\ + P(V' - V) - N\beta^{-1} ln(V'/V)]\}) \end{split} \tag{2.1.15}$$

2.1.3 Force field for rigid molecules

The potential force field consisted of electrostatic, see Eq. 2.1.16, and Lennard-Jones, see Eq. 2.1.17, interactions.

$$u_{ij}^{Q}(r_{ij}) = \frac{1}{4\pi\epsilon_0}\frac{q_i q_j}{r_{ij}} \tag{2.1.16}$$

$$u_{ij}^{LJ}(r_{ij}) = 4\epsilon_{ij}\left[\left(\frac{\sigma_{ij}}{r_{ij}}\right)^{12} - \left(\frac{\sigma_{ij}}{r_{ij}}\right)^{6}\right] \tag{2.1.17}$$

where ϵ_0 is the vacuum permittivity; r_{ij} is the distance between atoms i and j; ϵ_{ij} and σ_{ij} are parameters chosen for each atom pair ij; q_i are charge parameters set for each atom. In practice, ϵ_{ij} and σ_{ij} are determined by combining rules, named Lorentz-Berthelot, given by Eq. 2.1.18.

$$\begin{aligned} \sigma_{ij} &= \frac{1}{2}(\sigma_i + \sigma_j) \\ \epsilon_{ij} &= (\epsilon_i \epsilon_j)^{1/2} \end{aligned} \tag{2.1.18}$$

Then, due to the molecular rigidity, no intramolecular forces were applied and only 3 parameters were needed for each atom, $(\sigma_i, \epsilon_i, q_i)$.

The electrostatic potential is modeled as a r^{-1} decay, which is a simple function regarding r. On the other hand, the Lennard-Jones potential shape is more intricate, see Fig. 2.1. It portrays a "hard sphere" core with an attractive well.

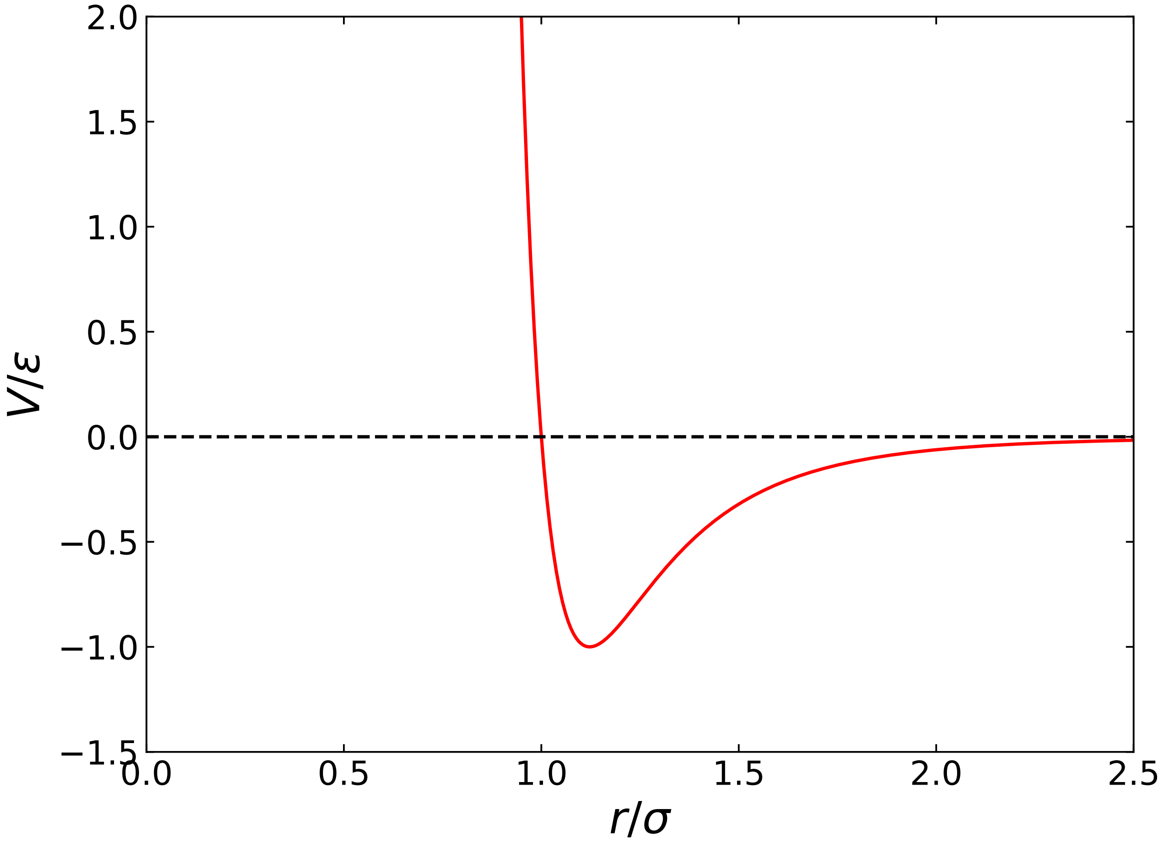

Figure 2.1: Lennard-Jones potential shape with minimum at $V = -\epsilon$ and $r = 2^{1/6}\sigma$

Regarding long-range interactions, the Lennard-Jones tail contribution decays by r^{-6}, while the electrostatic is slower, with r^{-1}. If the electrostatic long-range effect is controled, then both are regulated.

There are two main methods to apply tail corrections for the electrostatic potential. The more straightforward one relies on considering the region after a cutoff radius to be filled by an ideal continuous material defined by a dielectric constant. However, the solvent being studied is composed of gases and the average dielectric constant of gaseous media is minuscule. The second method would be an Ewald summation, which works by making copies of the simulation box to consider the interaction between the primitive box and its copies. It can only be used if the system in the primitive box is neutral. The ZIF-8 was treated as a charged nanoparticle and the only way to neutralize the system would by adding counterions. It is a potentially effective procedure for liquid solvents, however gaseous environment will probably be significantly impacted by the counterions. The latter might induce clusters of gas molecules to be formed around it or interact directly with ZIF-8 sites of interest. To minimize the adverse effects, long-range interactions were not treated after the truncated cutoff distance r_c, which was chosen as a large enough value to ensure it would work properly.

2.1.4 Periodic boundary conditions

In the current work, Monte Carlo molecular simulations intended to portray macroscopic samples. However, explicitly representing each atom of such system is impossible with the current processing power. Also, molecules on the borders would interact differently than the ones in the bulk, which could lead to unwanted border behavior. One way to address those issues is by enforcing periodic boundary conditions as represented in Fig. 2.2. In that case, the simulation box is treated as a primitive cell and is replicated in all of its sides. Each particle can interact with all other particles in this infinite periodic system. Then, to limit that infinite sum, a cutoff radius is determined based on the usual range of the interactions. Note the primitive cell lattice should be larger than two times the cutoff radius to avoid artificial events.

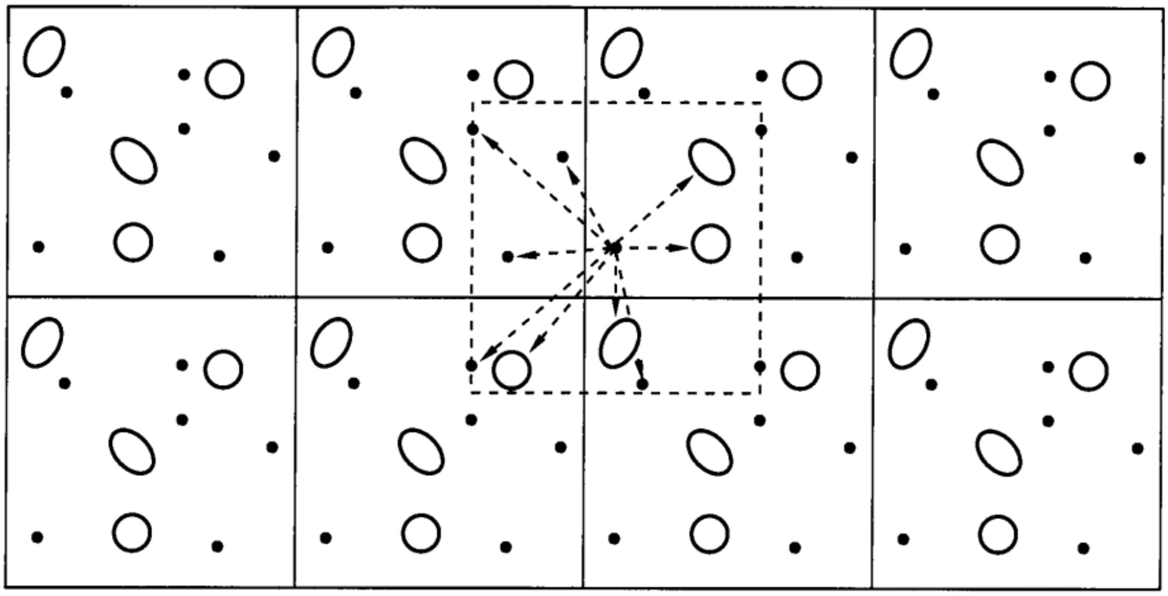

Figure 2.2: Representation of a system with periodic boundary conditions – Source: [213].

The algorithm simply transfers each molecule that trespass a side of the box to its opposing one. Do note it should be done with the whole molecule, not only the fragment that crossed a box side. Refusing to do so might generate artificial dipoles and compromise the whole simulation.

2.2 Classical molecular dynamics

The classical term implies that the nuclear motion of each atom of the system follows classical mechanics laws. That approximation can be satisfactorily employed depending on the used integration time step Δt. When the motion of light atoms, such as H, He, are allowed to freely evolve, Δt must be kept at 0.1 fs. By enforcing constraints on the aforementioned atoms, Δt can be increased while maintaining a reasonable classical approximation. Those methods are elaborated with more depth in the following sections.

2.2.1 Leap frog algorithm

Classical Molecular Dynamics operates by integrating the Newton's equations of motion for each particle of the system [213, 214]. Multiple numerical approaches can be applied, such as Verlet, velocity Verlet and Leap Frog algorithms. The construction of the latter starts by obtaining the Verlet algorithm. First of all, the coordinate of the particle is Taylor expanded around time t, Eq. 2.2.1.

$$r(t \pm \Delta t) = r(t) \pm v(t)\Delta t + \frac{f(t)}{2m}\Delta t^2 \pm \frac{\Delta t^3}{3!}\frac{d^3 r}{dt^3} + \mathcal{O}(\Delta t^4) \tag{2.2.1}$$

where $v(t)$ is the particle velocity, m is the particle mass and $f(t)$ is the force applied on the particle.

By adding both signs of Eq. 2.2.1, the Eq. 2.2.2 and its approximation Eq. 2.2.3 are obtained.

$$r(t + \Delta t) + r(t - \Delta t) = 2r(t) + \frac{f(t)}{m}\Delta t^2 + \mathcal{O}(\Delta t^4) \tag{2.2.2}$$

$$r(t + \Delta t) \approx 2r(t) - r(t - \Delta t) + \frac{f(t)}{m}\Delta t^2 \tag{2.2.3}$$

On the other hand, subtracting both signs of Eq. 2.2.1 results in Eq. 2.2.4, which can be reordered into Eq. 2.2.5.

$$r(t + \Delta t) - r(t - \Delta t) = 2v(t)\Delta t + \mathcal{O}(\Delta t^3) \tag{2.2.4}$$

$$v(t) = \frac{r(t + \Delta t) - r(t - \Delta t)}{2\Delta t} + \mathcal{O}(\Delta t^2) \tag{2.2.5}$$

Then, the Verlet algorithm is concluded. The Eq. 2.2.3 can be used to evolve the system and the Eq. 2.2.5, to compute kinetic energy or others velocity-dependent quantities.

The Leap Frog algorithm is equivalent to the Verlet one and can be obtained from the latter. It starts by defining the half-step velocities as Eq. 2.2.6.

$$\begin{aligned} v(t - \Delta t/2) &\equiv \frac{r(t) - r(t - \Delta t)}{\Delta t} \\ v(t + \Delta t/2) &\equiv \frac{r(t + \Delta t) - r(t)}{\Delta t} \end{aligned} \tag{2.2.6}$$

Then, the evolution of the coordinates can be written as Eq. 2.2.7.

$$r(t + \Delta t) = r(t) + v(t + \Delta t/2)\Delta t \tag{2.2.7}$$

By applying Eq. 2.2.6 on Eq. 2.2.3, the velocity evolution can be written as Eq. 2.2.8.

$$v(t + \Delta t/2) = v(t - \Delta t/2) + \Delta t\frac{f(t)}{m} \tag{2.2.8}$$

It should be noted the Leap Frog algorithm proceeds by alternating between iterations of position and velocity, see Fig 2.3.

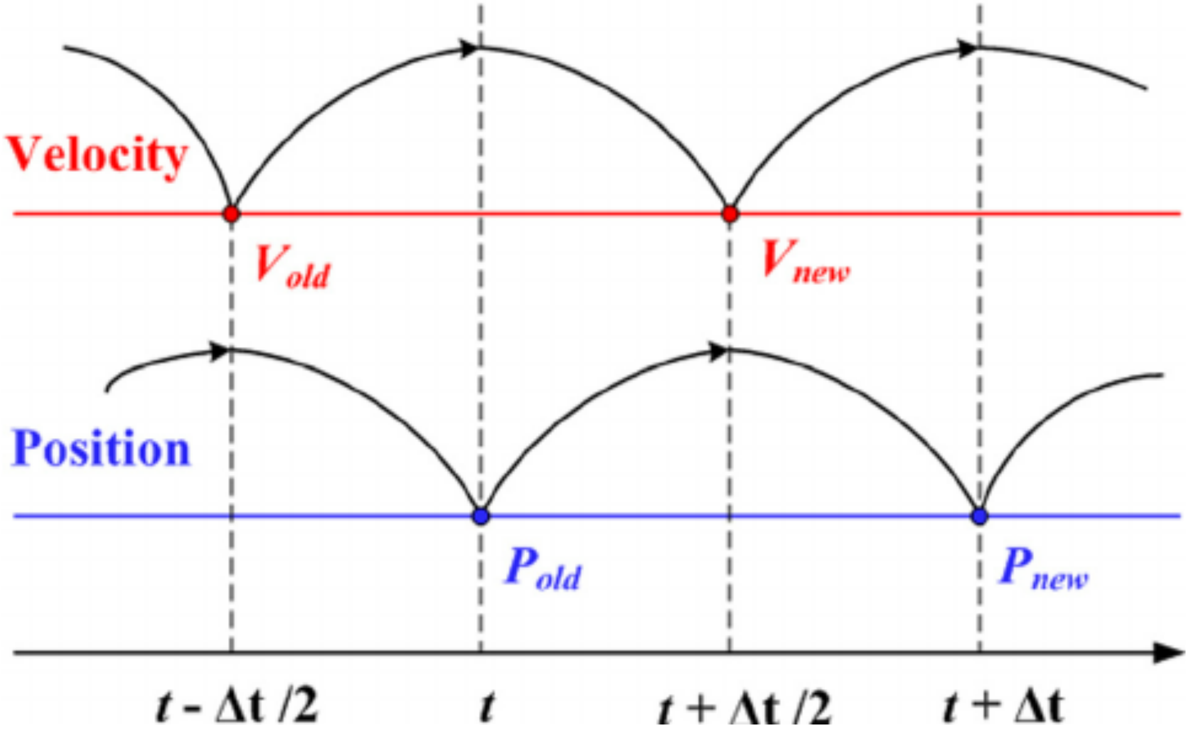

Figure 2.3: Leap frog scheme representation where position and velocities are evolved with a time difference of $\Delta t/2$ – Source: [216]

2.2.2 AMBER force field

The force field used in Molecular Dynamics simulations is the AMBER force field [217]. It is divided in two parts, non-bonded and bonded interactions. The first consists of Lennard-Jones and Coulomb potentials, previously considered as Eqs. 2.1.17 and 2.1.16. Non-bonded interactions were truncated beyond a cutoff radius and no long range corrections were employed. Similarly to the Monte Carlo simulations, huge values of cutoff radius were used to avoid artifacts due to the abrupt truncations.

Atoms of the same molecule can interact with non-bonded potentials. Within the force field model of AMBER, atoms that are neighbors or separated by two consecutive bonds do not interact via non-bonded terms. Atoms separated by three consecutive bonds interact through non-bonded potentials in the following way: Lennard-Jones potential is divided by 1/2 and Coulomb potential, by 1/1.2. Further atoms interact fully by non-bonded terms.

The bonded interactions are exclusive to flexible structures and are represented by Eq. 2.2.9.

$$
\begin{aligned}
V_{non-bonded} = & \sum_{bonds} k_b(r - r_0)^2 + \sum_{angles} k_\theta(\theta - \theta_0)^2 \\
& + \sum_{dihedrals} \sum_{n=1}^{3} V_n[1 + \cos(n\phi - \gamma)] + \sum_{improper} V_p[1 - \cos(2\phi)]
\end{aligned}
\tag{2.2.9}
$$

The first term is the harmonic potential of bond stretching. Its strength is quantified by the force constant k_b and the equilibrium bond length is given by r_0. Those parameters must be defined for each pair of bonded atom types in the simulated molecules.

The second term codifies the harmonic angle potential of each ordered triplet of atoms. k_θ is a force constant and θ_0 is a phase constant.

The third term refers to the dihedral, or torsional, potential of four atoms bonded in a row. Naming the chain of atoms as a, b, c, d, a dihedral is the angle between the planes defined by the atoms a, b, c and b, c, d. V_n is a force constant, n possibilits varied periodicities and γ is a phase constant.

Lastly, the fourth term is a tool to maintain certain structures within a plane. Named improper dihedral, it works in a similar way to dihedrals, however the atoms a, b, c, d are not consecutive. The atom c is bonded to the other three and remains in the middle of the triangle formed by a, b, d.

Do note that dihedral interactions can have periodicity higher than 3 and improper dihedrals can be written in a more general way to reinforce out-of-plane structures. However, this current work employed only the possibilities within Eq. 2.2.9.

2.2.3 Constraints

The classical approximation of Molecular Dynamics can be successfully applied with larger values of time steps if faster movements, such as vibration of H atoms, are constrained. The method utilized in this work is the LINCS algorithm [218].

LINCS works by implementing a matrix correction on the positions to fix the bond lengths while retaining its directions. This algorithm consists of two steps for each bond to be constrained after an unconstrained position update, see Fig. 2.4. First, the projection of the updated bond on the previous one is set to be equal to the latter. Second, the bond is corrected due to rotational lengthening with Eq.2.2.10.

$$\begin{aligned} l &= d\,cos\theta \\ p &= (2d^2 - l^2)^{1/2} \end{aligned} \tag{2.2.10}$$

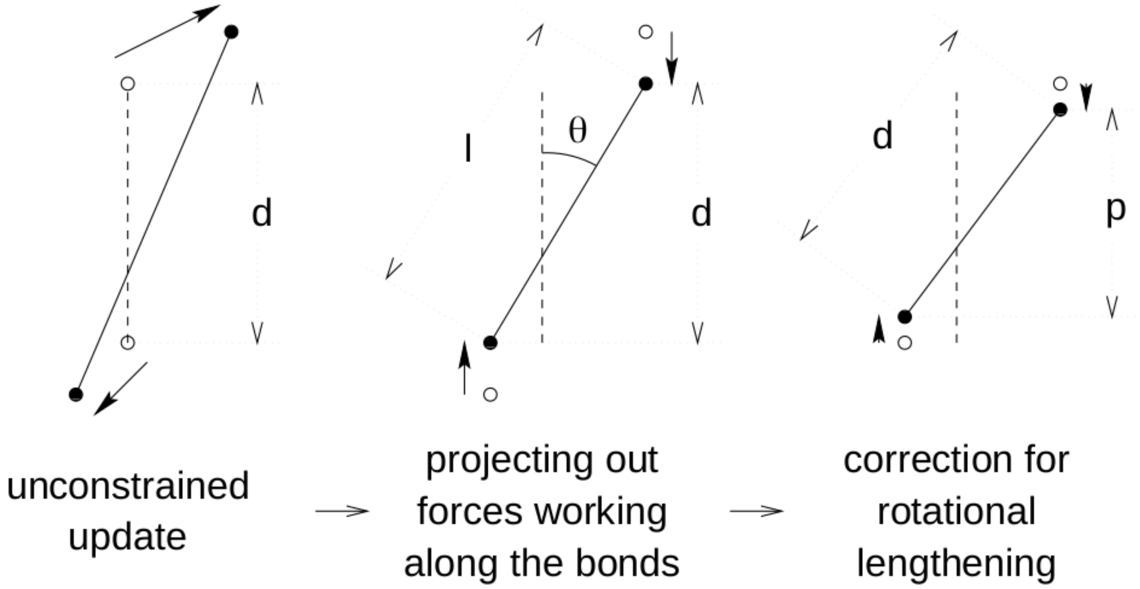

Figure 2.4: Representative diagram of LINCS procedure – Source: [219]

The full matricial treatment can be found in the original work [218].

2.2.4 Thermostat – velocity-rescale

The conventional Molecular Dynamics operate on the microcanonical ensemble, i.e., NVE ensemble. However, to establish a proper comparison with the Monte Carlo simulations, it is of interest to have the same ensemble on both. Then, to enforce a NVT ensemble, a thermostat is required. Many options are available within the literature, such as Berendsen, Nosé-Hoover, Andersen and Velocity-rescale thermostats. The latter was chosen due to its efficiency and proper generation of the canonical ensemble [220].

The most basic Velocity-rescale thermostat simply multiplies the velocity module of all particles to enforce a fixed temperature. However, that crude method creates an abrupt change of the velocities when applied. An enhanced method is the Berendsen thermostat in which temperature is slowly corrected by Eq. 2.2.11.

$$\frac{dT}{dt} = \frac{T_0 - T}{\tau} \tag{2.2.11}$$

where T_0 is the expected temperature and τ is a time constant.

The value of τ can be changed to adapt the coupling strength. However, variations of kinetic energy included by the Berendsen thermostat do not provide the generation of a proper canonical ensemble. Then, to restore those fluctuations, a noise is added by an auxiliary continuous stochastic dynamic procedure and the Velocity-rescale thermostat is complete. The stochastic dynamic step can be chosen arbitrary as long as it conserves the canonical distribution. In this work, the kinetic energy K with the stochastic term is given by Eq. 2.2.12.

$$dK = (K_0 - K)\frac{dt}{\tau_T} + 2\sqrt{\frac{KK_0}{N_f}}\frac{dW}{\sqrt{\tau_T}} \tag{2.2.12}$$

where N_f is the number of degrees of freedom, dW is a Wiener process and τ_T can be related to τ by Eq. 2.2.13.

$$\tau = \frac{2C_v\tau_T}{N_f k_B} \tag{2.2.13}$$

where C_v is the heat capacity of the system and k_B is the Boltzmann constant.

2.2.5 Periodic boundary conditions

The periodic boundary was applied in the same way as the one for Monte Carlo simulations, except that the periodic removal of the center of mass translational motion was employed. Since temperature is calculated by the average kinetic energy of the system, anomalous effects can take place such as freezing of the system. If most energy is applied on center of mass translation, it would freeze the internal movements of the system, while maintaining a wrongly apparent constant temperature.

2.3 Ab initio simulations

2.3.1 Born-Oppenheimer molecular dynamics

The concept of Ab Initio Molecular Dynamics is to evolve a system with classical point particles driven by quantum-mechanical formalism [221]. It starts with the time-dependent Schrödinger Eq. 2.3.1 with the Hamiltonian given by Eq. 2.3.2.

$$i\hbar\frac{\partial}{\partial t}\Phi(\{\mathbf{r}_i\},\{\mathbf{R}_I\};t) = \mathscr{H}\Phi(\{\mathbf{r}_i\},\{\mathbf{R}_I\};t) \tag{2.3.1}$$

$$\begin{aligned}\mathscr{H} = & -\sum_I \frac{\hbar^2}{2M_I}\nabla_I^2 - \sum_i \frac{\hbar^2}{2m_e}\nabla_i^2 \\ & + \frac{1}{4\pi\varepsilon_0}\sum_{i<j}\frac{e^2}{|\mathbf{r}_i - \mathbf{r}_j|} - \frac{1}{4\pi\varepsilon_0}\sum_{I,i}\frac{e^2 Z_I}{|\mathbf{R}_I - \mathbf{r}_i|} + \frac{1}{4\pi\varepsilon_0}\sum_{I<J}\frac{e^2 Z_I Z_J}{|\mathbf{R}_I - \mathbf{R}_J|} \\ = & -\sum_I \frac{\hbar^2}{2M_I}\nabla_I^2 + \mathscr{H}_e(\{\mathbf{r}_i\},\{\mathbf{R}_I\})\end{aligned} \tag{2.3.2}$$

where $\{\mathbf{r}_i\}$ and $\{\mathbf{R}_I\}$ are the electronic and nuclear degrees of freedom, respectively; M_I is the mass and Z_I is the atomic number of nucleous I, m_e is the electron mass, $-e$ is the electron charge and ε_0 is the vacuum permittivity.

Then, consider the nuclei to be fixed points in space, i.e. constant $\{\mathbf{R}_I\}$. The electronic Hamiltonian $\mathscr{H}_e$ can be written as Eq. 2.3.3 with orthonormalized eigenfunctions Ψ_k. Noting that $\mathscr{H}_e$, Ψ_k and E_k have parametric denpendance with $\{\mathbf{R}_I\}$.

$$\mathscr{H}_e(\{\mathbf{r}_i\};\{\mathbf{R}_I\})\Psi_k(\{\mathbf{r}_i\};\{\mathbf{R}_I\}) = E_k(\{\mathbf{R}_I\})\Psi_k(\{\mathbf{r}_i\};\{\mathbf{R}_I\}) \tag{2.3.3}$$

A complete set of all eigenfunctions $\{\Psi_k\}$ of $\mathscr{H}_e$ along with the time-dependent nuclear wave functions $\{\chi_k\}$ can be combined to express the total wave function as Eq. 2.3.4. It separates the light electrons and heavy nuclei due to different order of magnitude of the characteristic times of their motion.

$$\Phi(\{\mathbf{r}_i\},\{\mathbf{R}_I\};t) = \sum_{l=0}^{\infty} \Psi_l(\{\mathbf{r}_i\};\{\mathbf{R}_I\})\chi_l(\{\mathbf{R}_I\};t) \tag{2.3.4}$$

Applying Eq. 2.3.4 in Eq. 2.3.1 with left multiplication by $\Psi_l^*(\{\mathbf{r}_i\};\{\mathbf{R}_I\})$ and integration over $\{\mathbf{r}_i\}$ leads to a group of coupled differential equations. It is further developed by assuming $\Psi_l \in \mathbb{R}$ and by implementing the adiabatic approximation, where non-diagonal couplings are removed. Lastly, diagonal couplings are also neglected as the Born-Oppenheimer approximation and and the evolution for the nuclei motion is obtained as Eq. 2.3.5.

$$\left[-\sum_I \frac{\hbar^2}{2M_I}\nabla_I^2 + E_k(\{\mathbf{R}_I\})\right]\chi_k = i\hbar\frac{\partial}{\partial t}\chi_k \tag{2.3.5}$$

However, in Eq. 2.3.5 all nuclei are represented by a single wave equation in a specific electronic state, while molecular dynamics requires considering nuclei as individual classical points. To do so, the nuclei wave function is expanded as Eq. 2.3.6.

$$\chi_k(\{\mathbf{R}_I\};t) = A_k(\{\mathbf{R}_I\};t)exp[iS_k(\{\mathbf{R}_I\};t)/\hbar] \tag{2.3.6}$$

where $A_k, S_k \in \mathbb{R}$ and $A_k > 0$.

Substituting Eq. 2.3.6 in Eq. 2.3.5, considering only the real part and applying the classical limit of $\hbar \to 0$ results in Eq. 2.3.7.

$$\frac{\partial S_k}{\partial t} + \sum_I \frac{1}{2M_I}(\nabla_I S_k)^2 + E_k = 0 \tag{2.3.7}$$

The Eq. 2.3.7 has a important similarity with the Hamilton-Jacobi formulation as in Eq. 2.3.8.

$$\begin{aligned} &\frac{\partial S_k}{\partial t} + H_k(\{\mathbf{R}_I\}, \{\nabla_I S_k\}) = 0 \\ &H_k(\{\mathbf{R}_I\}, \{\mathbf{P}_I\}) = T(\{\mathbf{P}_I\}) + V_k(\{\mathbf{R}_I\}) \end{aligned} \tag{2.3.8}$$

Finally, consider a given conserved energy E_k^{tot} and the definition for conjugate canonical momenta $\mathbf{P}_I \equiv \nabla_I S_k$. Then, the solutions of Eq. 2.3.7 from the Hamilton-Jacobi formulation are written as Eq. 2.3.9.

$$M_I \ddot{\mathbf{R}}_I(t) = -\nabla_I V_k^{\mathrm{BO}}(\{\mathbf{R}_I(t)\}) \tag{2.3.9}$$

with $V_k^{\mathrm{BO}}(\{\mathbf{R}_I(t)\})$ given by $\min_{\Psi_k}\{\langle\Psi_k|\mathscr{H}_e|\Psi_k\rangle\}$. Then, Eqs. 2.3.3 and 2.3.9 can be rewritten as Eq. 2.3.10 for the electronic ground state.

$$\begin{aligned} M_I \ddot{\mathbf{R}}_I(t) &= -\nabla_I \min_{\Psi_0}\{\langle\Psi_0|\mathscr{H}_e|\Psi_0\rangle\} \\ E_0\Psi_0 &= \mathscr{H}_e\Psi_0 \end{aligned} \tag{2.3.10}$$

In summary, the procedure is made by: I) Finding the Born-Oppenheimer potential energy surface E_k of the electronic Hamiltonian given by Eq. 2.3.3 of state k at the static nuclei coordinates $\{\mathbf{R}_I(t)\}$. II) Evolving the nuclei positions via classical mechanics with an effective potential V_k^{BO} constructed from the E_k surfaces.

Do note the quantum problem is reduced to a time-independent Schrödinger equation with parametric dependence of $\{\mathbf{R}_I\}$, alternated with classical mechanics.

2.3.2 Electronic structure method - density functional theory

The following concern is about estabilishing a method to calculate $\langle\Psi|\mathscr{H}_e|\Psi\rangle$. The density functional theory (DFT) starts with the Hohenberg-Kohn theorems, which enables the development of a many-body theory with electron density ρ as the main quantity [221–224]. In this case, the ground state energy can be written as Eq. 2.3.11.

$$E_0 = \min_{\rho}\left(T[\rho(\mathbf{r})] + E_{ee}[\rho(\mathbf{r})] + E_{Ne}[\rho(\mathbf{r})] + E_{NN} + E_{XC}[\rho(\mathbf{r})]\right) \tag{2.3.11}$$

where $T[\rho(\mathbf{r})]$ is the kinetic energy functional, $E_{ee}[\rho(\mathbf{r})]$ is the Coulomb interaction energy functional between electrons, $E_{Ne}[\rho(\mathbf{r})]$ is the Coulomb interaction energy functional between electron and nucleous, E_{NN} is the Coulomb interaction energy functional between nuclei and $E_{XC}[\rho(\mathbf{r})]$ is the exchange and correlation energy functional.

Up to this point, the electron density ρ is exact, however it is not readily known in a many-body system. Kohn-Sham reduced the many-body problem into a set of orthonormal one-particle functions, named Kohn-Sham orbitals $\{\phi_i\}$. Initially, the electrons are considered as uncharged fermions, so without interactions between them. Slater determinants can be used to represent exact wave functions of uncharged fermions. Then, a non-interacting reference system can be achieved with the electronic one-body density as Eq. 2.3.12 satisfying $\langle\phi_i|\phi_j\rangle = \delta_{ij}$.

$$n(\mathbf{r}) = \sum_i^{occ} f_i \left|\phi_i(\mathbf{r})\right|^2 \tag{2.3.12}$$

where $\{f_i\}$ are integer occupation numbers. Then, the energy functionals were rewritten as Eq. 2.3.13.

$$E_0 = \min_{\{\phi_i\}} \left(T_S[\{\phi_i\}] + E_{Ne}[n] + E_{ee}[n] + E_{NN} + E_{XC}[n]\right) \tag{2.3.13}$$

where each of the terms, except $E_{XC}[n]$, are explained and expanded into their explicit form:

- Non-interacting kinetic energy functional $T_S[\{\phi_i\}]$ as Eq. 2.3.14

$$T_S[\{\phi_i\}] = -\frac{\hbar^2}{2m_e} \sum_i^{occ} f_i \left\langle \phi_i \left| \nabla^2 \right| \phi_i \right\rangle \tag{2.3.14}$$

- Coulomb interaction energy functional between nucleous and electron $E_{Ne}[n]$ as Eq. 2.3.15

$$E_{Ne}[n] = -\frac{e^2}{4\pi\varepsilon_0} \int \sum_I \frac{Z_I}{|\mathbf{R_I} - \mathbf{r}|}\, n(\mathbf{r})\, d\mathbf{r} \tag{2.3.15}$$

- Coulomb interaction energy functional between electrons $E_{ee}[n]$ as Eq. 2.3.16

$$E_{ee}[n] = \frac{1}{2} \frac{e^2}{4\pi\varepsilon_0} \iint \frac{n(\mathbf{r}')}{|\mathbf{r} - \mathbf{r}'|}\, n(\mathbf{r})\, d\mathbf{r}' d\mathbf{r} \tag{2.3.16}$$

- Coulomb interaction energy between nuclei E_{NN} as Eq. 2.3.17

$$E_{NN} = \frac{e^2}{4\pi\varepsilon_0} \int \sum_{I<J} \frac{Z_I Z_J}{|\mathbf{R_I} - \mathbf{R_J}|}\, n(\mathbf{r})\, d\mathbf{r} \tag{2.3.17}$$

The respective potential of each energy functional can be obtained by Eq. 2.3.18.

$$V_\alpha(\mathbf{r}) = \frac{\delta E_\alpha[n]}{\delta n(\mathbf{r})} \tag{2.3.18}$$

Then, the Kohn-Sham equation can finally be written as Eq. 2.3.19.

$$
\begin{aligned}
&H_e^{KS}\phi_i(\mathbf{r}) = \sum_j \Lambda_{ij}\phi_i(\mathbf{r}) \\
&H_e^{KS} = -\frac{\hbar^2}{2m_e}\nabla^2 + \frac{e^2}{4\pi\varepsilon_0}\sum_{I<J}\frac{Z_I Z_J}{|\mathbf{R_I}-\mathbf{R_J}|} - \frac{e^2}{4\pi\varepsilon_0}\sum_I \frac{Z_I}{|\mathbf{R_I}-\mathbf{r}|} \\
&+ \frac{e^2}{4\pi\varepsilon_0}\frac{1}{2}\int \frac{n(\mathbf{r}')}{|\mathbf{r}-\mathbf{r}'|}d\mathbf{r}' + \frac{\delta E_{XC}[n]}{\delta n(\mathbf{r})}
\end{aligned}
\tag{2.3.19}
$$

Via an unitary transformation on the orbitals ϕ_i such as $\phi_i' = \Sigma_j U_{ij}\phi_j$ with $\Sigma_j U_{ij}^* U_{jk} = \delta_{ik}$, the canonical form of the Kohn-Sham equation is obtained as $H_e^{KS}\phi_i' = \epsilon_i\phi_i'$. Where $\{\epsilon_i\}$ are the Kohn-Sham eigenvalues and the total energy can be written in terms of $\{\epsilon_i\}$ as 2.3.20.

$$
E^{\mathrm{KS}} = \sum_i \epsilon_i - \frac{e^2}{4\pi\varepsilon_0}\frac{1}{2}\iint \frac{n(\mathbf{r})n(\mathbf{r}')}{|\mathbf{r}-\mathbf{r}'|}d\mathbf{r}'d\mathbf{r} + E_{XC}[n] - \int \frac{\delta E_{XC}[n]}{\delta n(\mathbf{r})}\,n(\mathbf{r})d\mathbf{r}
\tag{2.3.20}
$$

The Kohn-Sham equation is solved by a self-consistent procedure. It starts with an initial guess of $n(\mathbf{r})$, followed by iterations of Eq. 2.3.19 and calculations of $n(\mathbf{r})$ until self-consistency is achieved.

2.3.3 Exchange and correlation functional

The Kohn-Sham method separates exact known terms from the unknown, the exchange and correlational functional $V_{XC}[n]$. A wide array of approximations are available in the literature for $V_{XC}[n]$. Among them, the Generalized-Gradient Approximations (GGAs) were found to provide good accuracy, particularly the Perdew–Burke-Ernzerhof (PBE) functional [224].

In a GGA, the energy $E_{XC}[n]$ can be obtained by Eq. 2.3.21.

$$
E_{XC}[n] = \int d\mathbf{r} f(n, \nabla n)
\tag{2.3.21}
$$

where $f(n, \nabla n)$ is a semilocal functional chosen and adjusted to obtain known values for the final energy value. The potential cannot be readily reached with Eq. 2.3.18 due to its semilocal behavior. The one used in this work is the PBE functional from [225] and a deeper handling on general forms of $E_{XC}[n]$ can be found in [224].

2.3.4 Orbital representations

The orbitals ϕ_i can be represented in a multitude of forms, each with its own advantages and disadvantages. The valence orbitals are usually described in a different formalism from the core ones, due to their contrasting energy magnitude.

The basic models for valence electrons are Gaussian, Slater and plane-wave functions. The first two portray a localized feature, while the third is delocalized and periodic. A hybrid of Gaussian and plane-wave functions (named GPW) was chosen to construct valence orbitals ϕ_i, see Eq. 2.3.22. As a side note, Slater functions would better represent the physical aspect of the orbitals. However, Gaussians provides better analytic evaluations.

$$\begin{aligned} \phi_i(\mathbf{r}) &= R_i(r)\, Y_{l_i,m_i}(\theta,\varphi) \\ R_i(r) &= r^{l_i} \sum_{j=1}^{N} c_{ij}\, exp(-\alpha_j\, r^2) \end{aligned} \tag{2.3.22}$$

where $Y_{l,m}(\theta,\varphi)$ are spherical harmonics, c_{ij} and α_j are weighting constants.

More specifically, double zeta for valence electrons plus polarization functions (DZVP) were used. It means two functions $\phi_i(\mathbf{r})$ were employed for each orbital plus a set of polarization functions with higher angular momentum.

Regarding core electrons, they were represented by smooth and close to the nuclear core region pseudo wave functions. Such choice is assured by the chemical inactivity of the inner electrons and reduces the calculation time. The chosen method is the Goedecker-Teter-Hutter (GTH) norm-conserving pseudopotential [226] from Eq. 2.3.23.

$$V_{\text{loc}} = -\frac{Z_{\text{eff}}}{r}\, erf\left(\frac{r}{\sqrt{2}r_{\text{loc}}}\right) + exp\left[-\left(\frac{r}{\sqrt{2}r_{\text{loc}}}\right)^2\right] \sum_{i=1}^{4} C_i \left(\frac{r}{r_{\text{loc}}}\right)^{2i-2} \tag{2.3.23}$$

where erf is the error function, Z_{eff} is the nucleus charge minus the charge of core electrons, r_{loc} is the range of the Gaussian ionic charge distribution and $\{C_i\}$ are constants. The first term of Eq. 2.3.23 is the long-range factor, while the second is the short-range one.

Finally, the total orbital is constructed by a linear combination of atomic orbitals (LCAO). Noting the coefficients are set based on theoretical methods, not to reflect experimental results, which attain the ab initio label.

Different approaches to orbital representations can be found in [221, 222, 224].

2.3.5 Thermostat – velocity-rescale

Up to this point the molecular dynamics would evolve in the microcanonical ensemble, i.e. NVE. Yet, the NVT ensemble is required for a proper comparation between the other considered methods. For such, a thermostat is imperious. The same thermostat from the Classical Molecular Dynamics was employed, the Velocity-rescale procedure. Its application is analogous since only nuclear positions and momenta are dynamic variables for both Classical and Born-Oppenheimer Molecular Dynamics.

2.4 Electronic structure calculations

Two main branches of theories were operated for electronic structure calculations:

1. Density Functional Theory with PBE exchange-correlation pure functional
2. Hartree-Fock plus Density Functional Theories with B3LYP exchange-correlation hybrid functional

Since DFT and the PBE functional were already approached in the Section 2.3, only Hartree-Fock theory and B3LYP functional are explained below.

2.4.1 Hartree-Fock theory

Hartree-Fock (HF) theory, also known as self-consistent field (SCF) theory, begins by writting the many-electron wave function as a single Slater determinant, Eq. 2.4.1.

$$\begin{aligned}&\Phi_{\mathrm{HF}}(\mathbf{r}_1, \mathbf{r}_2, ..., \mathbf{r}_{\mathrm{N}}, \boldsymbol{\sigma}_1, \boldsymbol{\sigma}_2, ..., \boldsymbol{\sigma}_{\mathrm{N}})\\ &\qquad = \frac{1}{\sqrt{N!}}\begin{vmatrix}\phi_1(\mathbf{r}_1,\boldsymbol{\sigma}_1) & \phi_2(\mathbf{r}_1,\boldsymbol{\sigma}_1) & \cdots & \phi_{\mathrm{N}}(\mathbf{r}_1,\boldsymbol{\sigma}_1)\\ \phi_1(\mathbf{r}_2,\boldsymbol{\sigma}_2) & \phi_2(\mathbf{r}_2,\boldsymbol{\sigma}_2) & \cdots & \phi_{\mathrm{N}}(\mathbf{r}_2,\boldsymbol{\sigma}_2)\\ \vdots & \vdots & \ddots & \vdots\\ \phi_1(\mathbf{r}_{\mathrm{N}},\boldsymbol{\sigma}_{\mathrm{N}}) & \phi_2(\mathbf{r}_{\mathrm{N}},\boldsymbol{\sigma}_{\mathrm{N}}) & \cdots & \phi_{\mathrm{N}}(\mathbf{r}_{\mathrm{N}},\boldsymbol{\sigma}_{\mathrm{N}})\end{vmatrix}\end{aligned} \tag{2.4.1}$$

Note this approximation considers exchange effects, but not correlational effects, since a general many-body wave function would require more than a single Slater determinant.

The energy contributions are given by Eq. 2.4.2 with $\hat{H}$ being given by one-electron and two-electron contributions in Eq. 2.4.3.

$$E^{(a)} = \int \Phi^* \hat{H}_a \Phi d\mathbf{r}_1 ... d\mathbf{r}_{\mathrm{N}} \tag{2.4.2}$$

$$\hat{H} = \hat{H}^{(1)} + \hat{H}^{(2)} = -\frac{\hbar^2}{2m_e}\sum_{i=1}^{N}\nabla^2_{\mathbf{r}_i} + \frac{e^2}{4\pi\varepsilon_0}\frac{1}{2}\sum_{i=1}^{N}\sum_{j\neq i}^{N}\frac{1}{|\mathbf{r}_i - \mathbf{r}_j|} \tag{2.4.3}$$

That way, the one-electron surviving terms add up to Eq. 2.4.4.

$$E^{(1)} = -\frac{\hbar^2}{2m_e}\sum_{i=1}^{N}\int \phi_i^*(\mathbf{r})\nabla^2_{\mathbf{r}}\phi_i(\mathbf{r})d\mathbf{r} = \sum_{i=1}^{N} E_{ii} \tag{2.4.4}$$

While the two-electron contribution in Eq. 2.4.5 splits in two parts, the Coulomb integrals J_{ij} and the Exchange integrals K_{ij}.

$$
\begin{aligned}
E^{(2)} &= \frac{e^2}{4\pi\varepsilon_0}\frac{1}{2}\sum_{i=1}^{N}\sum_{j=1}^{N}(J_{ij}-K_{ij}) \\
J_{ij} &= \iint \phi_i^*(\mathbf{r})\phi_j^*(\mathbf{r}')\,\frac{1}{|\mathbf{r}-\mathbf{r}'|}\,\phi_i(\mathbf{r})\phi_j(\mathbf{r}')d\mathbf{r}d\mathbf{r}' \\
K_{ij} &= \iint \phi_i^*(\mathbf{r})\phi_j^*(\mathbf{r}')\,\frac{1}{|\mathbf{r}-\mathbf{r}'|}\,\phi_i(\mathbf{r}')\phi_j(\mathbf{r})d\mathbf{r}d\mathbf{r}'
\end{aligned}
\tag{2.4.5}
$$

Then, the total Hartree-Fock energy can be obtained as Eq. 2.4.6.

$$
E^{\mathrm{HF}} = E^{(1)} + E^{(2)} + E_{\mathrm{NN}} \tag{2.4.6}
$$

where E_{NN} is the energy due to the Coulombic interaction of all nuclei pairs.

Finally, the Hartree-Fock equation can be written as Eq. 2.4.7.

$$
\begin{aligned}
\hat{\mathscr{F}}\phi_i(\mathbf{r}) &= \sum_j \Lambda_{ij}\phi_i(\mathbf{r}) \\
\hat{\mathscr{F}} &= -\frac{\hbar^2}{2m_e}\nabla^2_{\mathbf{r}_1} + \frac{e^2}{4\pi\varepsilon_0}\sum_j\left(\hat{\mathscr{J}}_j - \hat{\mathscr{K}}_j\right)
\end{aligned}
\tag{2.4.7}
$$

where $\hat{\mathscr{F}}$ is the Fock operator, $\hat{\mathscr{J}}_j$ is the Coulomb operator and $\hat{\mathscr{K}}_j$ is the exchange operator. The last two are defined by Eq. 2.4.8.

$$
\begin{aligned}
\hat{\mathscr{J}}_j\phi_i(\mathbf{r}) &= \int \phi_j^*(\mathbf{r}')\,\frac{1}{|\mathbf{r}-\mathbf{r}'|}\,\phi_j(\mathbf{r}')d\mathbf{r}'\ \ \phi_i(\mathbf{r}) \\
\hat{\mathscr{K}}_j\phi_i(\mathbf{r}) &= \int \phi_j^*(\mathbf{r}')\,\frac{1}{|\mathbf{r}-\mathbf{r}'|}\,\phi_i(\mathbf{r}')d\mathbf{r}'\ \ \phi_j(\mathbf{r})
\end{aligned}
\tag{2.4.8}
$$

By a unitary transformation on the orbitals ϕ_i such as $\phi_i' = \Sigma_j U_{ij}\phi_j$ with $\Sigma_j U_{ij}^* U_{jk} = \delta_{ik}$, the canonical form of the Hartree-Fock equation is obtained as $\hat{\mathscr{F}}\phi_i' = \epsilon_i\phi_i'$, where $\{\epsilon_i\}$ are the Hartree-Fock eigenvalues. The total energy can be written in terms of $\{\epsilon_i\}$ as 2.4.9 to correct the interaction double-counting.

$$
E^{\mathrm{HF}} = \sum_i \epsilon_i - \frac{e^2}{4\pi\varepsilon_0}\frac{1}{2}\sum_i\sum_j(J_{ij}-K_{ij}) + E_{\mathrm{NN}} \tag{2.4.9}
$$

Alike the Kohn-Sham equation solving, the Hartree-Fock equation is solved by a self-consistent procedure.

2.4.2 Exchange and correlation functional

The hybrid functional B3LYP is a combination of energy contributions from a multitude of functionals to represent known molecular behavior. Its form is given by Eq. 2.4.10.

$$A\, E_X^{\text{Slater}} + (1-A)\, E_X^{\text{HF}} + B\, \Delta E_X^{\text{Becke}} + C\, E_C^{\text{LYP}} + (1-C)\, E_C^{\text{VWN}} \tag{2.4.10}$$

where A, B and C are fitting constants, the subscripts X and C means exchange and correlation terms, respectively, and the superscript refers to the used functional/method:

- Slater [227–229] – is a Local (Spin) Density Approximation (LDA). In LDAs the exchange energy density is assumed to be equal to the exact case of a homogeneous electron gas. The only information needed is the exchange energy of the homogeneous gas written in terms of the density.
- HF – Hartree-Fock energy from Section 2.4.1.
- Becke [230], LYP [231, 232] – are GGA methods such as PBE. The main structures are similar to PBE, however the fitted functionals $f(n, \nabla n)$ from Eq. 2.3.21 differs.
- VWN [233] – is also a LDA method. However, the correlation energy is not same as the exact homogeneous electron gas, but rather a approximation or fit. VWN is constructed as an interpolation for fractional spin polarization.

2.4.3 Orbital representations

In electronic structure calculations the orbitals were represented by Dunning's correlation-consistent, polarized valence, basis set (cc-pV) [234]. In this case, both core and valence orbitals are represented and some higher angular momentum orbitals are added as well to account for polarization. Each orbital Φ_{nlm} was constructed with two base orbitals φ_{nlm} weighted by ζ to account for its diffusivity, i.e. double zeta (DZ), see Eq. 2.4.11.

$$\Phi_{nlm}(\mathbf{r}) = \varphi_{nlm}(\mathbf{r}, \zeta_1) + \alpha \varphi_{nlm}(\mathbf{r}, \zeta_2) \tag{2.4.11}$$

where ζ controls the width of the orbital and α is a weighting constant.

Another improvement can be attained by augmenting the system with one extra diffuse function (aug), i.e. with small values of ζ, for every angular momentum available in the basis. By combining the reduced names, the used bases are called cc-pVDZ and aug-cc-pVDZ.

2.4.4 Geometry relaxation

A relaxed molecular structure means it is located in the global minimum of the potential energy surface. However, this surface is constructed with numerous dimensions, which are the number of degrees of freedom within the molecule. Then, a well directed search must be employed to avoid local minima and to navigate efficiently on a system with high dimensionality.

The used procedure is a hybrid scheme of 3 different methods, each employed at its favored region. It starts with a wide search of potential wells to avoid local minima, followed by a quick and well behaved minimization and finished by a precise probe near the minimum.

The first is the rational function optimization (RFO) [235, 236]. RFO is reliable within a quadratic order in energy and it deals with a crucial shift parameter λ. Based on its choice, the search leaves a current potential well to find others in the vicinity. Which means, local minima can be avoided and the step length of λ is updated to adapt for different potential surface trends.

The second is the Geometry Optimization Using Energy-Represented Direct Inversion in the Iterative Subspace (GEDIIS) [237]. GEDIIS is faster and reduces large energy oscillations drastically when compared to the other two methods. It works by constructing a vector $\mathbf{R}^*$ from previous geometries $\mathbf{R}_i$ by Eq. 2.4.12.

$$\mathbf{R}^* = \sum_{i=1}^{N} c_i \mathbf{R}_i, \quad \text{where} \sum_{i=1}^{N} c_i = 1 \ \ \text{and} c_i > 0, i = 1, ..., N \tag{2.4.12}$$

Then, after some algebraic manipulations, the new energy $E(\mathbf{R}^*)$ is obtained as Eq. 2.4.13

$$E(\mathbf{R}^*) = \sum_{i=1}^{N} c_i E(\mathbf{R}_i) - \frac{1}{2} \sum_{i,j=1}^{N} c_i c_j (\mathbf{g}_i - \mathbf{g}_j)(\mathbf{R}_i - \mathbf{R}_j) \tag{2.4.13}$$

$E(\mathbf{R}^*)$ is minimized with respect to $\{c_i\}$ in a least-square fashion. The next step $\mathbf{R}_{i+1}$ is obtained from $\mathbf{R}^*$ with first order Hessian corrections based on the RFO method.

The third is the Geometry Optimization Using Direct Inversion in the Iterative Subspace (GDIIS) [238]. GDIIS is similar to GEDIIS with the difference being the next step $\mathbf{R}_{i+1}$ is obtained from first and second orders on the Hessian corrections. It allows faster convergence when near the minimum than GEDIIS.

2.4.5 Charge calculations

The force field model for Monte Carlo and Molecular Dynamics simulations requires a charge parameter for each atom. For such, the employed parametrization procedure was the Charges from Electrostatic Potentials using a Grid-based method (CHELPG) [239]. It works by calculating the ab initio molecular electrostatic potential (MEP) in a grid around the molecule. Then, atomic charges are optimized in a least-squares sense to describe MEP with the constraint of maintaining the total parametrized charge equal to the total system charge. Note CHELPG is not recommended for large molecular systems since the innermost atoms will be only slightly relevant for the outer MEP grid.

2.4.6 Binding energy

The binding energy was obtained by dividing a molecular system in two fragments. Then, three energy terms were calculated, of fragment 1 E_1, of fragment 2 E_2 and of both fragments combined E_{1+2}. Lastly, the binding energy E_b was reached by Eq. 2.4.14.

$$E_b = E_{1+2} - E_1 - E_2 \tag{2.4.14}$$

Each energy term was achieved by a hybrid Self-Consistent Field (SCF) method [240]. The energy values were calculated by Direct Inversion of the Iterative Subspace (DIIS) when close to convergence and Energy-based DIIS (EDIIS) when far from convergence. Both methods DIIS and EDIIS are respectively similar to GDIIS and GEDIIS, previously approached. In summary, both construct an error vector $x = \Sigma_i c_i x_i$ and minimize x relative to $\{c_i\}$. In DIIS, x is a suitable commutator and in EDIIS, it is a Hartree-Fock energy functional.

The molecular fragments might display basis set superposition errors (BSSE). It occurs when basis functions of one fragment overlaps with atoms of the other and artificially alters the latter electron distribution. For instance, consider Eq. 2.4.14 with the superscripts being the used basis sets, see Eq. 2.4.15.

$$E_b = E_{1+2}^{(1+2)} - E_1^{(1)} - E_2^{(2)} \tag{2.4.15}$$

The counterpoise correction [241] is based on writing the artificial contribution on each fragment as Eq. 2.4.16.

$$\begin{aligned} E_{BSSE}(1) &= E_1^{(1+2)} - E_1^{(1)} \\ E_{BSSE}(2) &= E_2^{(1+2)} - E_2^{(2)} \end{aligned} \tag{2.4.16}$$

2.5 Analysis properties

2.5.1 Radial distribution function

The Radial Distribution Function (RDF) is a method to describe and visualize the density of particles based on the distance from a fixed point. A RDF is usually named $g(r)$ and is constructed by dividing the system into spherical shells of width Δr centered on a reference point A. The number of particles B in each shell is counted and divided by $4\pi r^2 \Delta r$ to obtain the density in each shell. Lastly, it is normalized by the average density ρ_B^{avg} of particles B in the whole simulation box, see Fig. 2.5. The definition of $g(r)$ centered on particles A with respect to particles B can be arranged as Eq. 2.5.1.

$$g(r) = \frac{1}{\rho_B^{avg}} \frac{1}{N_A} \sum_{i \in A}^{N_A} \sum_{j \in B}^{N_B} \frac{\delta(r_{ij} - r)}{4\pi r^2 \Delta r} \tag{2.5.1}$$

where N_A is the total particles A and r_{ij} is the distance between particles i and j.

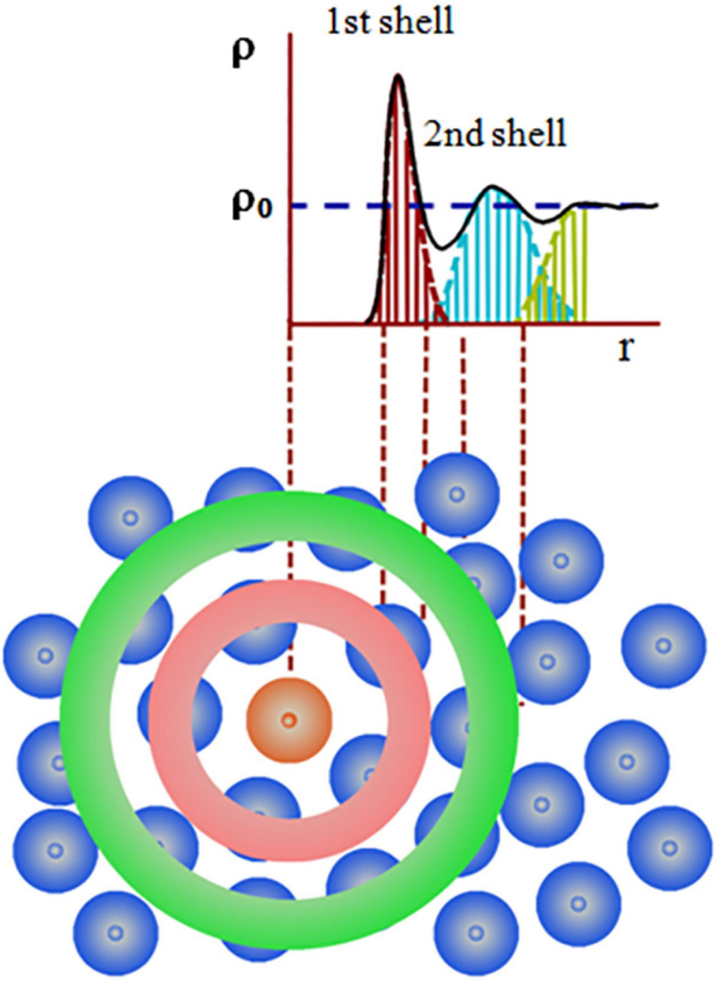

Figure 2.5: Radial distribution function representation of spherical shells around a reference particle – Source: [242]

In practice, the δ is not directly used. The system is divided in spherical shells from r to $r + \Delta r$ and the count of particles B in each shell is displayed in a histogram with the proper normalization.

Also, the integral of $g(r)$ from r_1 to r_2 results in the number of particles inside the spherical region between r_1 and r_2.

2.5.2 Diffusion coefficient

The diffusion coefficient D describes the proportion between molar flux of a molecular species and its concentration gradient. It can be obtained during equilibrium from the time correlation equation named Green-Kubo expression in Eq. 2.5.2 or by its associated

Einstein relation in Eq. 2.5.3.

$$D = \frac{1}{3}\int_0^\infty \langle \mathbf{v}_i(t)\cdot\mathbf{v}_i(0)\rangle_{i\in A}\,dt \tag{2.5.2}$$

$$\lim_{t\to\infty}\left(\|\mathbf{r}_i(t)-\mathbf{r}_i(0)\|^2\right)_{i\in A} = 6Dt \tag{2.5.3}$$

where A is the particle type of interest, $\mathbf{r}_i$ and $\mathbf{v}_i$ are its position and velocity, respectively.

Both expressions yield the same coefficient, however the Eq. 2.5.3 carries less numerical inaccuracy and was used in the current study.

3

Methodology

In this chapter the calculated and simulated systems parameters are detailed, along with the objective behind the various sets of considered systems. The used definition for captured gas molecules is explored as well.

"Nothing has such power to broaden the mind as the ability to investigate systematically and truly all that comes under thy observation in life"
Marcus Aurelius

The used softwares for each type of procedure were: DICE [243] for Classical Monte Carlo Molecular Simulations (MC), GROMACS [244] for Classical Molecular Dynamics (MD), CP2K [245] for Born-Oppenheimer Molecular Dynamics (BOMD) and GAUSSIAN [246] for electronic structure calculations.

3.1 Simulation parameters

The gases were portrayed with the parameters from Vujic et al. [247], except H_2O which followed the SPC/E model [248]. On the MD simulations, the CO_2 molecule flexibility was represented by adding the force constants $k_b^{CO} = 714230.5754\, kJ/(mol\, nm^2)$ for the bond CO and $k_\theta^{OCO} = 1236.1252\, kJ/(mol\, rad^2)$ for the angle OCO. Those constants were based on the EPM2 [249] and UFF [250] models.

Also, to avoid repetitive content, unless informed otherwise, the simulations were performed with the following parameters:

- MC: rigid molecular framework model; NVT ensemble; 2.10^6 and 1.10^6 MC cycles of thermalization and production, respectively; potential cutoff radius of 60 Å.
- MD: flexible molecular framework model with constraints enforced by the LINCS algorithm; system evolution by the leap frog algorithm; velocity-rescale thermostat; time step of 2 fs, possible since H bonds were kept constrained; 10 and 90 ns of thermalization and production, respectively; potential cutoff radius of 60 Å.
- BOMD: cubic box of lattice 20 Å; PBE exchange correlational functional; GPW functions and GTH pseudopotentials; gaussian orbitals represented by DZVP and plane wave with a charge density cutoff of 280 Ry; electronic density calculations had a self-consistent-field energy threshold of 1.10^{-6} hartree; time step of 0.25 fs; total time length of 40 ps.

Note the termalization length was chosen based on the potential energy curves. Only when the system reached a constant minimum potential energy average it was deemed ready for production. Also, the BOMD parameters were chosen based on the work of Cabral et al. [251], which studied CO_2 in different phases.

A potential issue PBC might cause is an atom being affected by itself from a neighbor artificial box. To avoid it, the potential radius cutoff must be equal or smaller than half of the smaller box lattice. In a box with 1000 CO_2 molecules, at ambient conditions, the maximum cutoff radius was of 13 nm. However, for Lennard-Jones and Coulombic potentials it is unlikely to require such a large cutoff. The truncated cutoff distance r_c was determined as the distance which outer molecules had interaction energy magnitude comfortably below 0.05 kcal/mol. That requirement was explored between molecule pairs always containing the ZIF-8 nanoparticle, since it had the highest charge and number of atoms. Checking the interaction energies, a r_c of 4.5 nm would contain the vast majority of the required molecules. Still, r_c was extended up to 6 nm, to ensure it would work for all sceneries. No difference was observed between two tests with 6 nm and 13 nm for r_c.

3.2 Simulated systems

The conducted MC, MD and BOMD simulations are given in the Tables 3.1, 3.2 and 3.3, respectively.

Table 3.1: All MC simulations conducted in the work

#	Solvent	Gas	Ensemble	Pressure (atm)	Temperature (K)
(i)	$((Zn^{+2})_{24}\,(mIm^{-})_{60}\,(Zn^{+2})_{24})^{+36}$	$100\,CO_2$	NVT	1	273.15
(ii)	$((Zn^{+2})_{24}\,(mIm^{-})_{60}\,(Zn^{+2})_{24})^{+36}$	$200\,CO_2$	NVT	1	273.15
(iii)	$((Zn^{+2})_{24}\,(mIm^{-})_{60}\,(Zn^{+2})_{24})^{+36}$	$500\,CO_2$	NVT	1	273.15
(iv)	$((Zn^{+2})_{24}\,(mIm^{-})_{60}\,(Zn^{+2})_{24})^{+36}$	$1000\,CO_2$	NVT	1	273.15
(v)	$((Zn^{+2})_{24}\,(mIm^{-})_{60}\,(Zn^{+2})_{24})^{+36}$	$2000\,CO_2$	NVT	1	273.15
(vi)	$((Zn^{+2})_{24}\,(mIm^{-})_{60}\,(Zn^{+2})_{24})^{+36}$	$1000\,CO_2$	NVT	1	298.00
(vii)	$((Zn^{+2})_{24}\,(mIm^{-})_{60}\,(Zn^{+2})_{24})^{+36}$	$1000\,CO_2$	NPT	1	273.15
(viii)	$((Zn^{+2})_{24}\,(mIm^{-})_{60}\,(Zn^{+2})_{24})^{+36}$	$1000\,CO_2$	NPT	20	273.15
(ix)	$((Zn^{+2})_{24}\,(mIm^{-})_{60}\,(Zn^{+2})_{24})^{+36}$	$1000\,H_2O$	NVT	1	273.15
(x)	$((Zn^{+2})_{24}\,(mIm^{-})_{60}\,(Zn^{+2})_{24})^{+36}$	$1000\,H_2O$	NVT	1	298.00
(xi)	$((Zn^{+2})_{24}\,(mIm^{-})_{60}\,(Zn^{+2})_{24})^{+36}$	$1000\,N_2$	NVT	1	273.15
(xii)	$((Zn^{+2})_{24}\,(mIm^{-})_{60}\,(Zn^{+2})_{24})^{+36}$	$1000\,O_2$	NVT	1	273.15
(xiii)	$((Zn^{+2})_{24}\,(mIm^{-})_{60}\,(Zn^{+2})_{24})^{+36}$	$1000\,Ar$	NVT	1	273.15
(xiv)	$((Zn^{+2})_{24}\,(mIm^{-})_{60}\,(Zn^{+2})_{6})$	$1000\,CO_2$	NVT	1	273.15
(xv)	$((Zn^{+2})_{24}\,(mIm^{-})_{60}\,(Zn^{+2})_{6})$	$1000\,H_2O$	NVT	1	273.15
(xvi)	$((Zn^{+2})_{24}\,(mIm^{-})_{60}\,(Zn^{+2})_{6})$	$1000\,N_2$	NVT	1	273.15
(xvii)	$((Zn^{+2})_{24}\,(mIm^{-})_{60}\,(Zn^{+2})_{12})^{+12}$	$1000\,CO_2$	NVT	1	273.15
(xviii)	$((Zn^{+2})_{24}\,(mIm^{-})_{60}\,(Zn^{+2})_{12})^{+12}$	$1000\,H_2O$	NVT	1	273.15
(xix)	$((Zn^{+2})_{24}\,(mIm^{-})_{60}\,(Zn^{+2})_{12})^{+12}$	$1000\,N_2$	NVT	1	273.15
(xx)	$((Zn^{+2})_{24}\,(mIm^{-})_{60}\,(Zn^{+2})_{16})^{+20}$	$1000\,CO_2$	NVT	1	273.15
(xxi)	$((Zn^{+2})_{24}\,(mIm^{-})_{60}\,(Zn^{+2})_{16})^{+20}$	$1000\,H_2O$	NVT	1	273.15
(xxii)	$((Zn^{+2})_{24}\,(mIm^{-})_{60}\,(Zn^{+2})_{16})^{+20}$	$1000\,N_2$	NVT	1	273.15
(xxiii)	$((Zn^{+2})_{24}\,(mIm^{-})_{60}\,(Zn^{+2})_{20})^{+28}$	$1000\,CO_2$	NVT	1	273.15
(xxiv)	$((Zn^{+2})_{24}\,(mIm^{-})_{60}\,(Zn^{+2})_{20})^{+28}$	$1000\,H_2O$	NVT	1	273.15
(xxv)	$((Zn^{+2})_{24}\,(mIm^{-})_{60}\,(Zn^{+2})_{20})^{+28}$	$1000\,N_2$	NVT	1	273.15
(xxvi)	$((Zn^{+2})_{24}\,(mIm^{-})_{60}\,(H^{+})_{12})$	$1000\,CO_2$	NVT	1	273.15
(xxvii)	$((Zn^{+2})_{24}\,(mIm^{-})_{60}\,(H^{+})_{12})$	$1000\,H_2O$	NVT	1	273.15
(xxviii)	$((Zn^{+2})_{24}\,(mIm^{-})_{60}\,(H^{+})_{12})$	$1000\,N_2$	NVT	1	273.15
(xxix)	$((Zn^{+2})_{24}\,(mIm^{-})_{60}\,(H^{+})_{18})^{+6}$	$1000\,CO_2$	NVT	1	273.15
(xxx)	$((Zn^{+2})_{24}\,(mIm^{-})_{60}\,(H^{+})_{18})^{+6}$	$1000\,H_2O$	NVT	1	273.15
(xxxi)	$((Zn^{+2})_{24}\,(mIm^{-})_{60}\,(H^{+})_{18})^{+6}$	$1000\,N_2$	NVT	1	273.15
(xxxii)	$((Zn^{+2})_{24}\,(mIm^{-})_{60}\,(H^{+})_{24})^{+12}$	$1000\,CO_2$	NVT	1	273.15
(xxxiii)	$((Zn^{+2})_{24}\,(mIm^{-})_{60}\,(H^{+})_{24})^{+12}$	$1000\,H_2O$	NVT	1	273.15
(xxxiv)	$((Zn^{+2})_{24}\,(mIm^{-})_{60}\,(H^{+})_{24})^{+12}$	$1000\,N_2$	NVT	1	273.15
(xxxv)	$(Zn^{+2}\,mIm^{-})^{+}$	$100\,CO_2$	NVT	1	273.15
(xxxvi)	$(Zn^{+2}\,mIm^{-})^{+}$	$100\,H_2O$	NVT	1	273.15
(xxxvii)	$(Zn^{+2}\,mIm^{-})^{+}$	$100\,N_2$	NVT	1	273.15
(xxxviii)	-	$2000\,CO_2$	NVT	1	273.15
(xxxix)	-	$2000\,CO_2$	NPT	1	273.15
(xl)	-	$2000\,CO_2$	NVT	10	225.15
(xli)	-	$2000\,CO_2$	NPT	10	225.15
(xlii)	-	$2000\,CO_2$	NVT	72	298.00
(xliii)	-	$2000\,CO_2$	NPT	72	298.00
(xliv)	$((Zn^{+2})_{24}\,(mIm^{-})_{60}\,(Zn^{+2})_{24})^{+36}$	$1000\,CO_2 + 1000\,H_2O$	NVT	1	273.15
(xlv)	$((Zn^{+2})_{24}\,(mIm^{-})_{60}\,(Zn^{+2})_{24})^{+36}$	$1000\,CO_2 + 1000\,N_2$	NVT	1	273.15

Table 3.2: All MD simulations conducted in the work

#	Solvent	Gas	Ensemble	Pressure (atm)	Temperature (K)
(xlvi)	$((Zn^{+2})_{24}\ (mIm^{-})_{60}\ (Zn^{+2})_{24})^{+36}$	$1000\,N_2$	NVT	1	273.15
(xlvii)	$((Zn^{+2})_{24}\ (mIm^{-})_{60}\ (Zn^{+2})_{24})^{+36}$	$1000\,CO_2$	NVT	1	273.15
(xlviii)	$((Zn^{+2})_{24}\ (mIm^{-})_{60}\ (Zn^{+2})_{24})^{+36}$	$1000\,CO_2 + 1000\,N_2$	NVT	1	273.15
(xlix)	$((Zn^{+2})_{24}\ (mIm^{-})_{60}\ (Zn^{+2})_{24})^{+36}$	$1000\,CO_2 + 9000\,N_2$	NVT	1	273.15
(l)	$((Zn^{+2})_{144}\ (mIm^{-})_{336}\ (Zn^{+2})_{72})^{+96}$	$8000\,CO_2$	NVT	1	273.15
(li)	$((Zn^{+2})_{144}\ (mIm^{-})_{336}\ (Zn^{+2})_{24})$	$8000\,CO_2$	NVT	1	273.15
(lii)	$((Zn^{+2})_{432}\ (mIm^{-})_{972}\ (Zn^{+2})_{144})^{+180}$	$27000\,CO_2$	NVT	1	273.15

Table 3.3: All BOMD simulations conducted in the work

#	Solvent	Gas	Temperature (K)
(liii)	$(Zn^{+2}\ mIm^{-})^{+}$	$4\,CO_2$	300.00
(liv)	$(Zn^{+2}\ mIm^{-})^{+}$	$4\,H_2O$	300.00

3.3 Electronic structure calculations

3.3.1 Geometry optimization and charge calculation

The geometry optimizations and CHELPG charge calculations were both carried out with the B3LYP method and aug-cc-pVDZ basis set. B3LYP is a common method throughout the literature for zeolitic imidazolate framework studies [166, 181, 183, 200, 252–254]. The systems from Figs. 3.1c, 3.1e, 3.1h, 3.1j were optimized and underwent CHELPG calculations with the method PBE since it was used on the BOMD simulations.

The systems from Fig. 3.1 were chosen for electronic structure calculations to test specific circumstances. Figs. 3.1b, 3.1c, 3.1g, 3.1h represent the superficial Zn atom in vacuum as monocoordinated or dicoordinated, while in the crystallographic and in the relaxed geometries. Figs. 3.1d, 3.1e, 3.1i, 3.1j represent the superficial Zn atom interacting with CO_2 and H_2O as monocoordinated or dicoordinated with the imidazole rings. Figs. 3.1k, 3.1l represent the bulk Zn atom with and without superficial H atoms. Fig. 3.1f represents the superficial H atom in vacuum. Also, in a different set of CHELPG calculations, the systems from Figs. 3.1d, 3.1e, 3.1i, 3.1j had its gas molecules fixed as point charges.

Do note other systems such as $(Zn^{+2}\ \ mIm^{-}) + 4N_2$ and $(Zn^{+2}\ \ mIm^{-}) + 5X$, where X is CO_2 or H_2O, were optimized as well. However, those did not portray a proper binding between Zn and the solvent molecules, such as Fig. 3.2.

3.3.2 Binding energy

The employed methodology started with optimization by B3LYP/aug-cc-pVDZ. Then, multiple binding energy calculation were carried out with B3LYP/cc-pVDZ in the following fashion. For example, a system composed by a ZIF-8 fragment (ZF) with 3 gas molecules named A, B and C, had twelve calculations performed. By denoting each

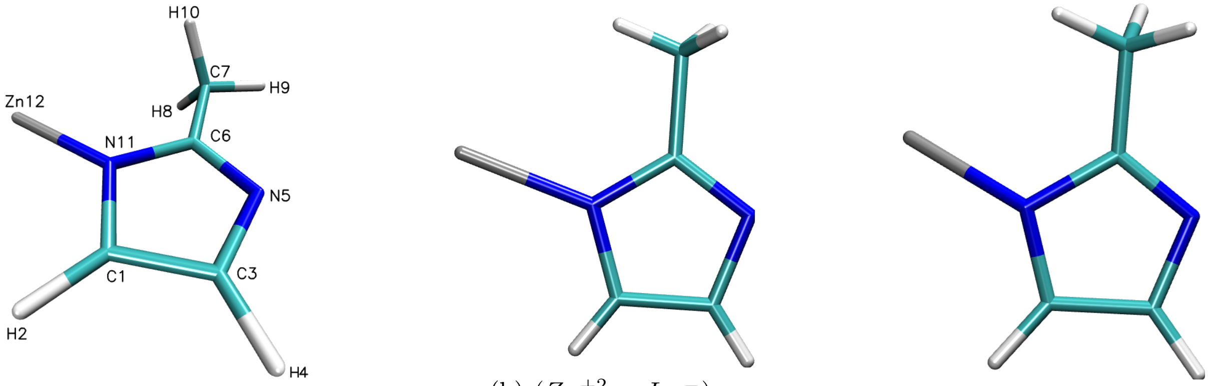

(a) Labels of the atoms

(b) $(Zn^{+2}\ \ mIm^{-})$

(c) $(Zn^{+2}\ \ mIm^{-})$

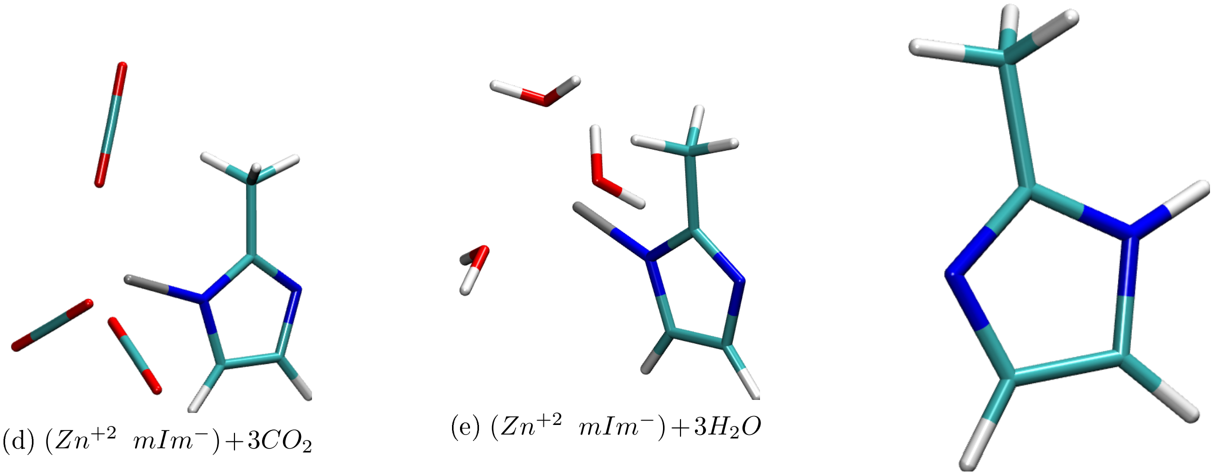

(d) $(Zn^{+2}\ \ mIm^{-}){+}3CO_2$

(e) $(Zn^{+2}\ \ mIm^{-}){+}3H_2O$

(f) $(H^{+}\ \ mIm^{-})$

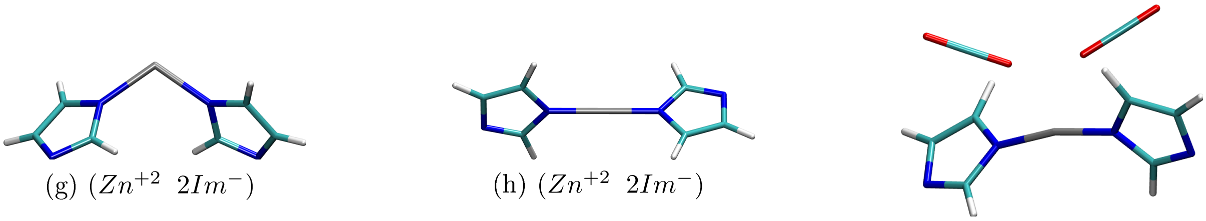

(g) $(Zn^{+2}\ \ 2Im^{-})$

(h) $(Zn^{+2}\ \ 2Im^{-})$

(i) $(Zn^{+2}\ \ 2Im^{-}) + 2CO_2$

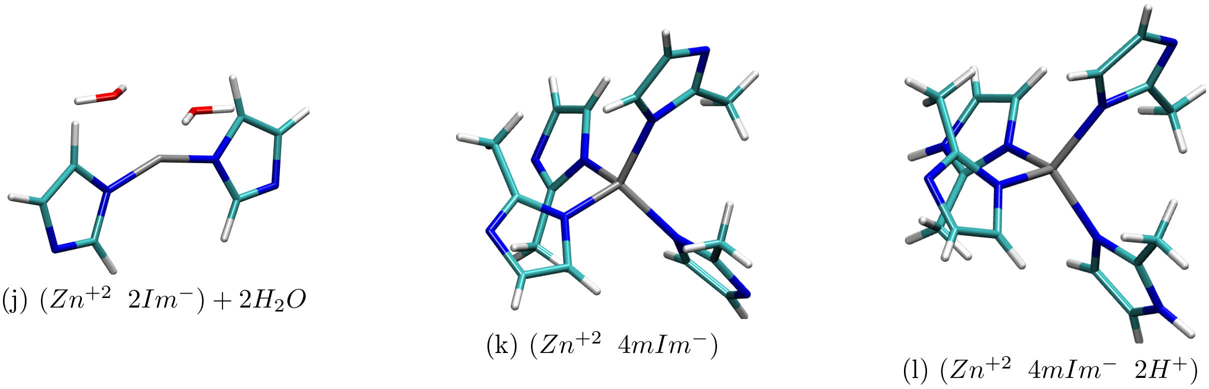

(j) $(Zn^{+2}\ \ 2Im^{-}) + 2H_2O$

(k) $(Zn^{+2}\ \ 4mIm^{-})$

(l) $(Zn^{+2}\ \ 4mIm^{-}\ \ 2H^{+})$

Figure 3.1: Fragments of ZIF-8 which underwent CHELPG charge calculations. All fragments but (b), (g), (k), (l) had its geometry optimized prior to the charge calculations. The (k) and (l) structures are meant to represent the environment in which bulk Zn atoms reside.

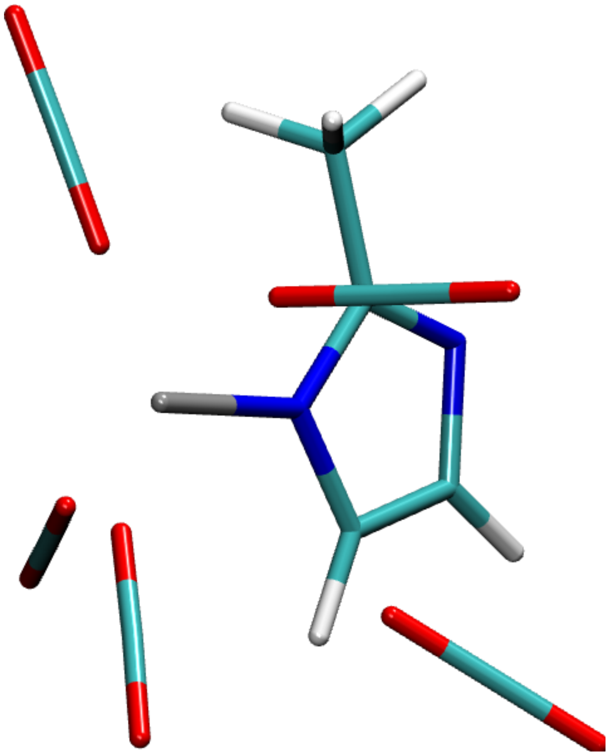

Figure 3.2: Molecular representation of optimized $(Zn^{+2}\ mIm^{-}) + 5CO_2$. The CO_2 molecule on the right-bottom diagonal was significantly further away from the Zn atom.

fragment between parenthesis, the calculations were: (ZF)(A), (ZF)(B), (ZF)(C), (ZF + A)(B), (ZF + A)(C), (ZF + B)(A), (ZF + B)(C), (ZF + C)(A), (ZF + C)(B), (ZF + A + B)(C), (ZF + A + C)(B), (ZF + B + C)(A). Then, an energy average of all twelve systems was considered to be the binding energy.

To do so, the systems 3.1d and 3.1e from Fig. 3.1 along with the ones from Fig. 3.3 underwent geometry optimization followed by binding energy calculations.

3.4 Systems used for each purpose

The systems from the Tables 3.1, 3.2 and 3.3 were used in different groups for each section of the work.

The charge parametrization in Section 4.1 was made with electronic structure calculations as explained in Section 3.3. The representation of atmospheric air on Section 4.2 was conducted with systems composed by different number of CO_2 molecules, which were (i) - (v). The geometry and energy validations on Section 4.3 were made with multiple methods and systems. MC simulations of (iv), (ix) and (xi) represented the 1x1x1 ZIF-8 nanoparticle with each gas CO_2, H_2O and N_2, individually. Similarly, the ZIF-8 fragment in (xxxv) - (xxxvii) with the mentioned gases was simulated. Meanwhile, BOMD simulations of (liii) and (liv) and electronic structure calculations were conducted to provide first principle results. The results for different gases in Section 4.4.1 were obtained from

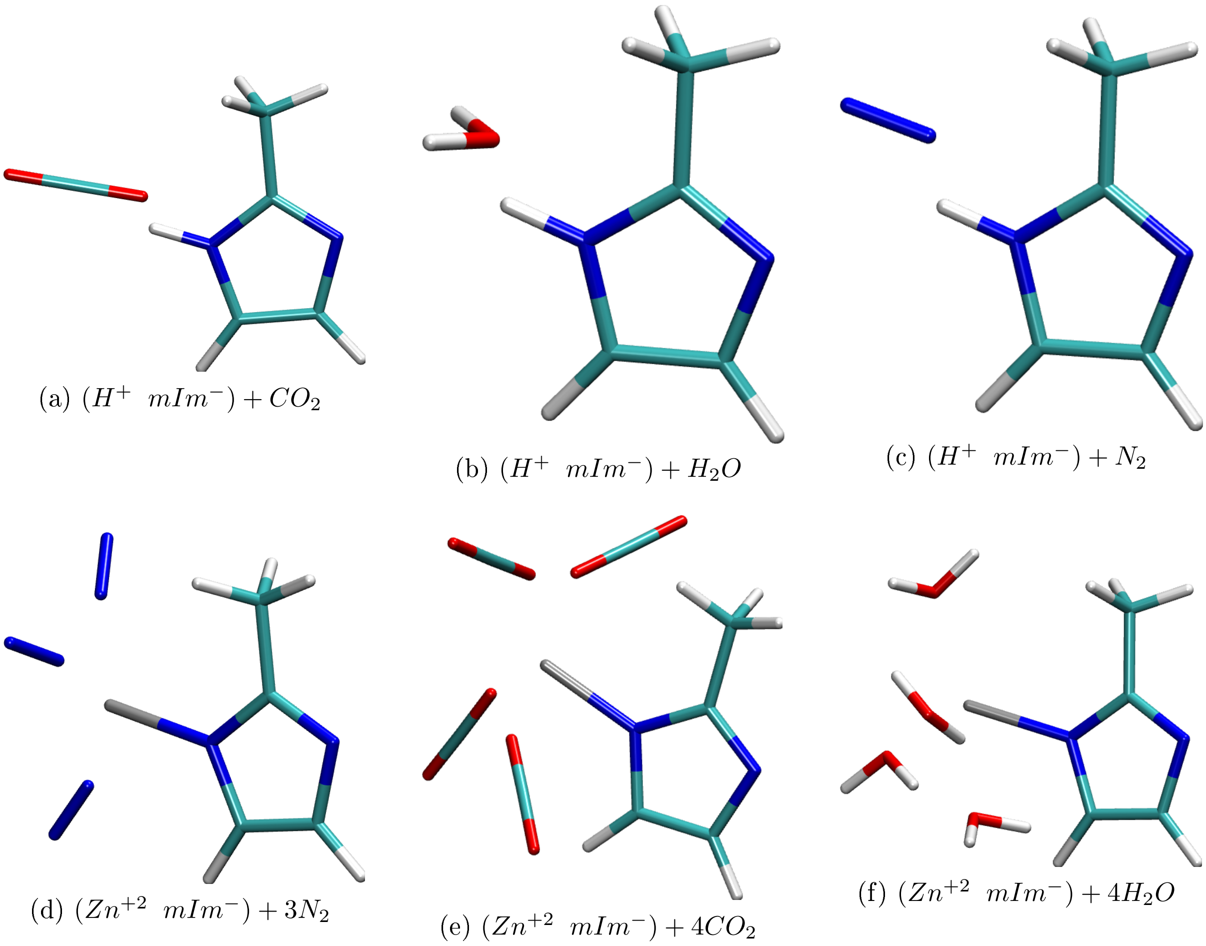

(a) $(H^+ \;\; mIm^-) + CO_2$

(b) $(H^+ \;\; mIm^-) + H_2O$

(c) $(H^+ \;\; mIm^-) + N_2$

(d) $(Zn^{+2} \;\; mIm^-) + 3N_2$

(e) $(Zn^{+2} \;\; mIm^-) + 4CO_2$

(f) $(Zn^{+2} \;\; mIm^-) + 4H_2O$

Figure 3.3: Fragments of ZIF-8 which underwent geometry optimization followed by binding energy calculations. The fragments (e) and (f) were also simulated via BOMD.

systems of 1x1x1 ZIF-8 with each gas CO_2, H_2O, N_2, O_2 and Ar, which were (iv), (ix) and (xi) - (xiii). The temperature effect in Section 4.4.2 was verified by comparing (iv) and (vi) for CO_2, (ix) and (x) for H_2O. The pressure effect in Section 4.4.3 was obtained by comparing different ensembles by (iv) and (vii), and different pressures by (vii) and (viii). The surface effect in Section 4.5 was performed with a wide number of simulations. The different ZIF-8 compositions and gases are represented in (iv), (ix), (xi), (xiv) - (xxv) and (xxvi) - (xxxiv). The MD parametrization in Section 4.6 was performed with multiple simulations differing by tweaks on the force field parameters. Most are not listed since only the final set of parameters is relevant. The system considered is (xlvii) which was compared to (iv). The direct CO_2 and H_2O gas competition in Section 4.7.1 was made with (xliv) and compared to (iv). The mixtures of CO_2 and N_2 in Section 4.7.2 were conducted both with MC and MD and in different proportions. The systems (xlv), (xlviii) and (xlix) were simulated and compared to (iv) and (xlvii). The CO_2 density study in Section 4.8 compared simulations of ZIF-8 + CO_2 in different ensembles, temperatures, simulation methods and competition scenarios. Those are (iv), (vi), (vii), (xlvii), (xlix).

Also, pristine CO_2 simulations of the systems (xxxviii) - (xliii) were performed.

The nanoparticle size study in Section 4.9 was performed with the 1x1x1, 2x2x2 and 3x3x3 ZIF-8 nanoparticles. From the Section 4.2, the 1x1x1 ZIF-8 nanoparticle needed at least 1000 gas molecules to attain a good approximation for the thermodynamic limit. In order to find a minimum amount of gas molecules reasonable for larger ZIF-8 nanoparticles, individual tests would have to be conducted. On the other hand, the efficient paralelization of GROMACS allows huge systems to be simulated in convenient time.

Consider a cube of lattice a. Its volume is a^3 and area is $6a^2$. If the lattice is grown to na, the volume and area would be n^3a^3 and $6n^2a^2$, respectively. Setting n to 2(3), the volume and area are $8a^3(27a^3)$ and $24a^2(54a^2)$, respectively. In comparison to the initial cube, the one with twice the lattice has a multiplier of 8 in volume and of 4 in area. It means that the needed molecules to solvate the cube with twice the lattice would need to grow by at least 4 and at most 8 times. Making use of the efficiency of GROMACS to avoid further testing, the 2x2x2 ZIF-8 nanoparticle simulation had 8000 CO_2 molecules. Following the same path, the 3x3x3 ZIF-8 nanoparticle was simulated with 27000 CO_2 molecules. Both the 2x2x2 and 3x3x3 ZIF-8 nanoparticles were simulated with all surface sites filled with Zn atoms as Fig. 1.7. Also, a neutral 2x2x2 ZIF-8 nanoparticle was simulated. Thus, the nanoparticle study was conducted with the (xlvii) and (l) - (lii) systems.

The diffusion coefficients in Section 4.10 were were obtained from (xlvii) with 10 ns continuing a previous (xlvii) simulation already on equilibrium. Then, no termalization was needed. The absorption time study in Section 4.11 was performed by preparing the system with the CO_2 or N_2 molecules randomly placed in the simulation box. The 1x1x1 ZIF-8 nanoparticle was placed in the middle of the box avoiding superpositions, then both (xlvi) and (xlvii) were simulated for 10 ns. The same procedure was done a total of 5 times by generating different initial positions for the CO_2 or N_2 molecules. The adsorbed CO_2 structure study in Section 4.12 was conducted on the system (iv).

3.5 Analysis methodologies

3.5.1 Definition of captured gas molecule

The RDF of monocoordinated Zn atoms relative to CO_2 from MC classical simulations is displayed in Fig. 3.4. The green curve, which refers to O of CO_2, has a deep local minima at 3.25 Å. This way, the CO_2 cutoff radius of interacting solvent molecules was estabilished at 3.25 Å for $Zn - O$. Similarly, the same pattern was observed at 2.75 and 2.95 Å for O of H_2O and N of N_2, respectively.

A definition for absorption in inner pores and for adsorption is also required. In Fig. 3.5 the combination of blue and yellow, i.e. $r < 14.65$Å, composes the inner region of the

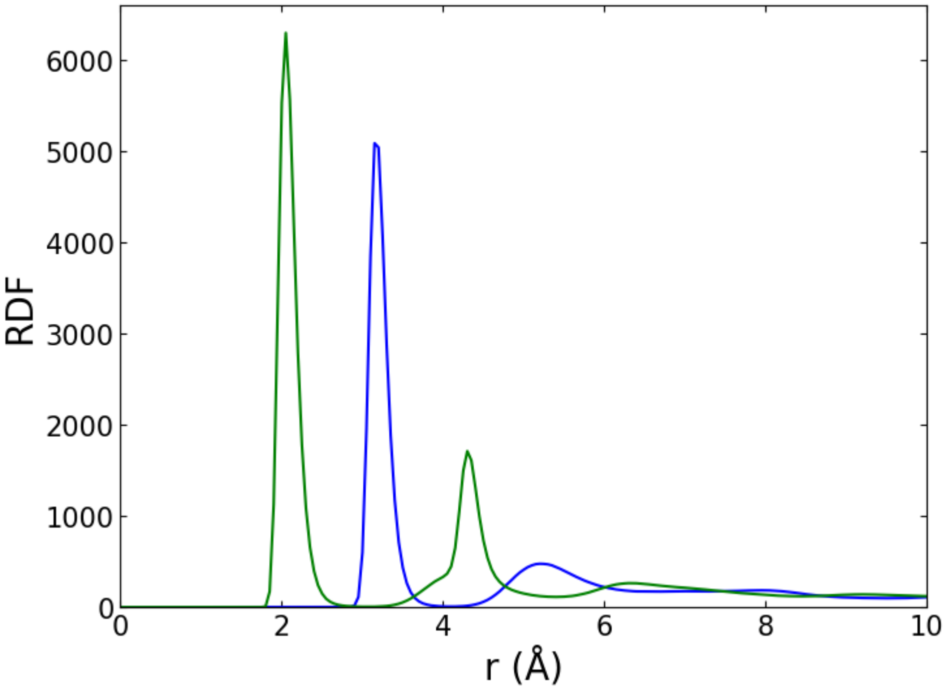

Figure 3.4: RDFs of monocoordinated Zn atoms in regard to CO_2 molecules from a classic simulation of the $((Zn^{+2})_{24}\ (mIm^{-})_{60}\ (Zn^{+2})_{24})$ nanoparticle and CO_2. Green and blue refers to the pairs Zn-O and Zn-C, respectively. The second peak of the Zn-C curve represents other CO_2 molecules interacting with the captured ones on the surface.

ZIF-8 nanoparticle. The thin peak at 15.0 Å refers to CO_2 molecules that interacts with two Zn atoms simultaneously. Also, the broader peak between 15.5 and 17.5 Å is the first solvation layer. The adsorbed molecules could be approximated by the first solvation layer, however a more precise path was used. All X gas molecules within a distance d^{X}_{Surf} of the atom in the surface site are deemed to be bonded. The distances are 3.25, 2.75 and 2.95 Å for CO_2, H_2O and N_2, respectively. Note that this approach is more precise since it only considers gas molecules directly bonded to the surface sites.

This mix of methods to identify absorbed and adsorbed molecules could count some gas molecules as both types since they might fit in both criterias. To verify it, the angle $NZn-O$ distribution is displayed in Fig. 3.6. In either distributions, the vast majority of occurrences have $NZn-O$ angles higher than 80^o. Considering the Fig. 3.5, a more acute $NZn-O$ angle would be needed for the captured CO_2 molecule to be both closely interacting with the Zn atom and inside the blue zone. Which means the distinction between a gas molecule being absorbed, adsorbed or neither is well established.

3.5.2 Free volume calculation

The density of captured CO_2 had to be calculated considering ZIF-8 occupies space already. It was conducted by approximating the atoms of ZIF-8 as rigid spheres and evaluating the free volume through MC counting. The radii for the framework atoms

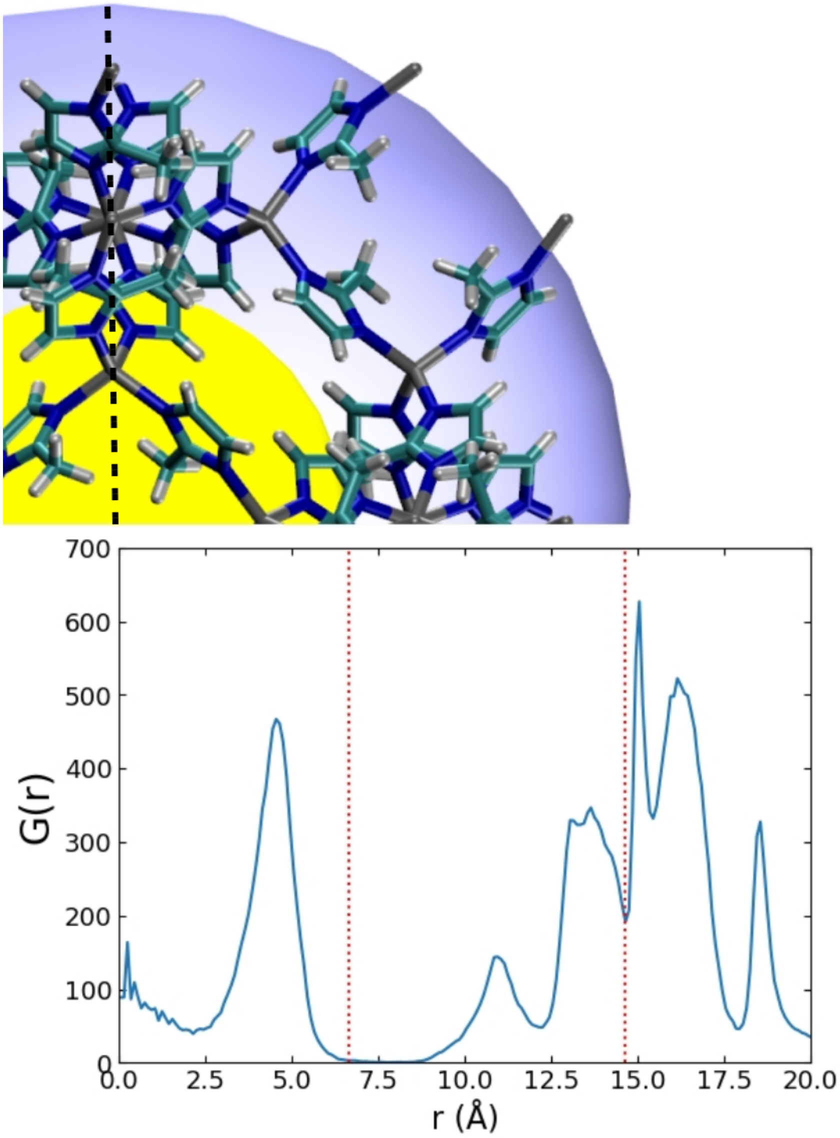

Figure 3.5: Regions of the 1x1x1 ZIF-8 nanoparticle with a RDF of the center of mass of CO_2. The yellow part is the inner core and the blue part is the inside region without its core.

were estabilished as 0.57 times of its own σ parameter. Such specific proportion was adopted due to:

- In the MD software GROMACS, when solvating a molecular structure in water, the Van der Waals radius of each atom is multiplied by 0.57 to avoid superpositions.
- In the molecular visualization and analysis software Mercury [255], the free volume in a molecule can be calculated as well. It works by probing the accessible surface for the solvent. Since specific regions of the molecule could not be chosen, only the whole unitary cell, it was not fit for this current work. Nevertheless, when selecting the same region, our method achieved the same volume with the choice of 0.57 times σ for the radii.

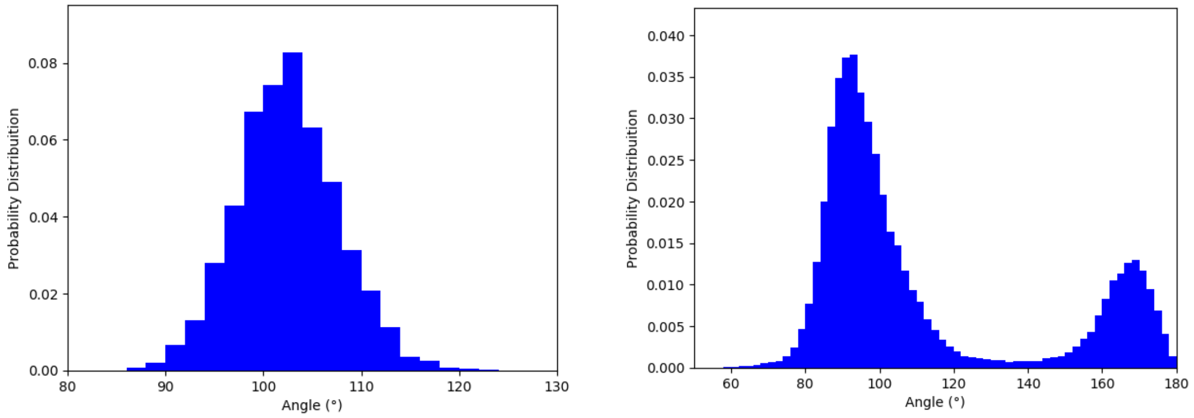

(a) CO_2 binding with 2 Zn

(b) CO_2 binding with 1 Zn

Figure 3.6: Angle $NZn - O$ distribution of CO_2 binded to superficial Zn atoms from a classic simulation. The distributions (a) and (b) represent different interaction structures between CO_2 and the ZIF-8 nanoparticle.

3.5.3 CO_2 diffusion coefficient calculation

The diffusion coefficients were calculated by the Einstein relation from Eq. 2.5.3, which requires a linear fit on the mean squared displacement (MSD) curve. This fit was obtained by the following steps.

The whole 10 ns trajectory was split in smaller ones of 1 ns each. In the middle of each smaller trajectory, the CO_2 molecules were categorized as "in", if their center of mass distance from ZIF-8 was smaller than 14.65 Å, or as "out", if their center of mass distance from ZIF-8 was smaller than 25.00 Å but bigger than 14.65 Å. These regions were chosen so that the vast majority of CO_2 molecules confirmed to be within it midway through the 1 ns trajectory, stayed there for the whole duration.

In each trajectory fragment, the MSD was calculated for both sets "in" and "out" separetely. A least squares fit $y = Ax + B$ was made for every of the aforementioned cases. The fit was applied only in an interval where the MSD trend was similar to a straight line.

4

Results

In this chapter the methods are employed on the gas capture by ZIF-8. It starts by laying down the foundation for the simulations, such as parametrization and representation issues. Then, multiple facets are explored, being thermodynamic effects, gas competition, ZIF-8 nanoparticle structures and CO_2 *detailed surveys.*

"The gem cannot be polished without friction, nor man perfected without trials."
Chinese Proverb

4.1 Charge parametrization

An essential step before any classical simulation can be performed is the force field parametrization. Regarding the rigid framework interactions, only intermolecular terms are present, being the Lennard-Jones (Eq. 2.1.17) and the Coulombic (Eq. 2.1.16) potentials. Thus, values of the parameters ϵ_{ij} and σ_{ij} for each molecule pair ij and of q_i for each atom must be estabilished. The ϵ_{ij} and σ_{ij} are constructed by a combination of individual terms ϵ_i and σ_i through the Lorentz-Berthelot rule, see Eq. 2.1.18. Then, the whole rigid framework parametrization is constituted by only three values for each atom type, being $(\sigma_i, \epsilon_i, q_i)$.

Hu et al. [168] developed a force field to study absorption of CO_2 and CH_4 in ZIF-8. The ZIF-8 was depicted as an infinite periodic bulk, which means the parameters were not optimized for surface atoms. In the current work, the values of σ_i and ϵ_i proposed by Hu et al. were first assumed to be reasonable for all atoms, bulk and surface ones. However, the charge parameters q_i could not be applied in the same way. An 1x1x1 nanoparticle of ZIF-8 terminated in Zn atoms is constitued of 48 Zn^{+2} atoms and 60 deprotonated 2-methylimidazolate groups (mIm^{-}), i.e., $((Zn^{+2})_{24}\ (mIm^{-})_{60}\ (Zn^{+2})_{24})$. The charge of the whole 1x1x1 nanoparticle is $+36$ e. If the bulk charge parameters from Hu et al. are indiscriminately applied for all atoms in the nanoparticle, its total charge results in $+18$ e. Thus, electronic structure calculations with CHELPG were performed on fragments of ZIF-8, see Section 3.3.1, to obtain more reasonable values of q_i for surface atoms.

The CHELPG charge parameters of the ZIF-8 fragments obtained for the systems in Fig. 3.1 are displayed in Tables 4.1, 4.2, 4.3. Note the methyl ligand was exchanged for a H atom named H7* in variants of the system $(Zn^{+2}\ \ 2Im^{-})$ to reduce the computational cost, since it was expected to have little effect on the Zn atom charge.

The PBE method was applied on the BOMD simulations. From the Tables 4.1, 4.2, 4.3, B3LYP and PBE methods yielded similar results when performed on the same systems. Which means the final charge parameters should be reasonable for applications regarding either of the methods.

Considering systems without gas molecules, between those that did and did not underwent prior geometry optimization, more distinct charge values were obtained when they were composed of fewer atoms. The systems 3.1b and 3.1c had different charge parameters especially for the N11 atom in the Table 4.1. On the other hand, the systems 3.1g and 3.1h are bigger and had more similar charge values. The systems 3.1k and 3.1l were not optimized due to their size and structure complexity. Following the trend of charge similarity as the system grows towards the crystallographic framework, the systems 3.1k and 3.1l were expected to be reasonable structures for charge calculations even without geometry optimization. Do note all systems with gas molecules had its geometry relaxed to ensure proper interaction conformation with the ZIF-8 fragment.

Table 4.1: CHELPG charge calculations of variants of the system $(Zn^{+2} \quad mIm^{-})$ with B3LYP and PBE methods. The systems with gas molecules had them either explicitly considered or fixed as point charges.

	B3LYP						PBE		[168]
Fig.	3.1b	3.1c	3.1d		3.1e		3.1c	3.1e	3.1b
	None	None	Explicit	Point	Explicit	Point	None	Explicit	None
C1	0.129	-0.121	-0.004	0.192	0.001	0.215	-0.013	0.023	-0.100
H2	0.008	0.118	0.049	0.016	0.049	0.004	0.082	0.042	0.100
C3	0.384	0.468	0.216	0.147	0.158	0.134	0.364	0.153	-0.100
H4	0.037	0.045	0.069	0.094	0.072	0.081	0.063	0.075	0.100
N5	-0.528	-0.514	-0.602	-0.491	-0.566	-0.596	-0.452	-0.535	-0.500
C6	0.551	0.405	0.832	0.952	0.697	1.070	0.465	0.689	0.500
C7	0.175	0.025	-0.453	-0.562	-0.381	-0.694	-0.017	-0.430	-0.300
H8	0.017	-0.030	0.054	0.089	0.152	0.242	-0.002	0.170	0.100
H9	0.046	0.163	0.187	0.225	0.064	0.112	0.151	0.082	0.100
H10	-0.167	-0.082	0.054	0.089	0.067	0.099	-0.065	0.090	0.100
N11	-0.722	-0.459	-1.047	-1.231	-0.928	-1.358	-0.555	-0.939	-0.500
Zn12	1.070	0.981	1.342	1.480	1.335	1.692	0.977	1.281	1.000

Table 4.2: CHELPG charge calculations of variants of the system $(Zn^{+2} \quad 2Im^{-})$ with B3LYP and PBE methods. The systems with gas molecules had them either explicitly considered or fixed as point charges. Atom types that appeared more than once have their charge displayed as the mean value.

	B3LYP						PBE		[168]
Fig.	3.1g	3.1h	3.1i		3.1j		3.1h	3.1j	3.1b
	None	None	Explicit	Point	Explicit	Point	None	Explicit	None
C1	-0.012	0.088	0.140	0.069	0.079	0.172	0.099	0.129	-0.100
H2	-0.016	0.020	0.009	0.028	0.033	0.010	0.015	0.016	0.100
C3	0.331	0.166	0.128	0.185	0.131	0.137	0.157	0.121	-0.100
H4	-0.010	0.041	0.045	0.034	0.028	0.020	0.042	0.026	0.100
N5	-0.690	-0.559	-0.551	-0.566	-0.560	-0.570	-0.533	-0.542	-0.500
C6	0.668	0.584	0.590	0.578	0.483	0.601	0.573	0.510	0.500
H7*	-0.055	-0.073	-0.075	-0.061	-0.025	-0.048	-0.070	-0.033	0.000
N11	-0.850	-0.930	-1.022	-0.960	-0.868	-1.130	-0.933	-0.942	-0.500
Zn12	1.268	1.326	1.436	1.386	1.260	1.614	1.300	1.279	1.000

Although the charge parameters of the system 3.1l, in Table 4.3, were different from the ones made by Hu et al., the overall trend was reasonable if you consider the mean values between protonated and deprotonated imidazole rings for each atom. The mean was deemed as reasonable due to similarity between charge values and making the average would be a way to propose a simplified set of parameters, especially considering the bulk environment without surface effects. Also, the charge of the Zn atom, of 1.036, had outstanding agreement with Hu et al. parameter of 1.000. Thus, the employed methodol-

Table 4.3: CHELPG charge calculations of variants of the systems $(H^+ \quad mIm^-)$ and $(Zn^{+2} \quad 4mIm^-)$ with B3LYP method. H13 is the H^+ atom which replaces Zn at the surface. Atom types that appeared more than once have their charge displayed as the mean value.

Fig.	3.1k	3.1l		3.1f	[168]
	None	Deprotonated	Protonated	None	None
C1	-0.210	-0.289	0.020	-0.279	-0.100
H2	0.045	0.076	0.086	0.154	0.100
C3	0.269	0.299	-0.089	0.197	-0.100
H4	-0.044	0.003	0.131	0.053	0.100
N5	-0.898	-0.804	-0.320	-0.591	-0.500
C6	0.790	0.725	0.501	0.454	0.500
C7	-0.344	-0.397	-0.389	-0.189	-0.300
H8	0.051	0.055	0.119	0.042	0.100
H9	0.058	0.071	0.124	0.082	0.100
H10	0.046	0.108	0.114	0.042	0.100
N11	-0.525	-0.515	-0.472	-0.237	-0.500
Zn12	1.046	1.036		-	1.000
H13	-	-	0.327	0.272	-

ogy in this work managed to reach similar bulk parameters, i.e. the methylimidazole and internal Zn atoms, to the work of Hu et al.

With the aforementioned comparison of the bulk charge parameters considering the ones from Hu et al., the method could be extrapolated for the surface atoms. Regarding the superficial Zn atom, a wide range of values were obtained, from 0.977 to 1.692. That way, which system and procedure would be best suited to address the superficial Zn atom?

First of all, ZIF-8 is expected to be allowed to interact with gas molecules. Which means pure ZIF-8 fragments systems are not a good option to reproduce potential polarization from the gas–ZIF-8 interaction. Instead, the systems 3.1d, 3.1e, 3.1i and 3.1j can portray a more representative example of the total ZIF-8 + gas system.

The next point is the choice to implement the gas molecules as explicit atoms or point fixed charges. Taking into consideration all gas molecules of the same type will have the same charge parameters in classical simulations, regardless of its relative position to ZIF-8, explicit gas could not be used if the polarization effects are significant. Considering Table 4.1, all systems with gas molecules, in respect to the ones without, had shown a considerably higher charge on the Zn atom. It demonstrates that CO_2 and H_2O polarization play an important role. The charge parameters obtained for explicit gas atoms are in Table 4.4. From the CO_2 parameters, a charge displacement between the O atoms would not be represented with the current force field model. Also, from the H_2O parameters, the charge sum for one H_2O molecule is not neutral, which could not be employed as well. Therefore, fixed point charges for the gases was the chosen procedure for the parametrization.

Table 4.4: CHELPG charge calculations of the gas molecules when explicitly represented with B3LYP and PBE methods. Atom types that appeared more than once have their charge displayed as the mean value.

	CO_2			H_2O		
	C	O_{near}	O_{far}	O	H_{near}	H_{far}
$(Zn^{+2}\ mIm^{-})$ w/ B3LYP	0.806	-0.465	-0.240	-0.830	0.470	0.470
$(Zn^{+2}\ mIm^{-})$ w/ PBE	-	-	-	-0.788	0.477	0.411
$(Zn^{+2}\ 2Im^{-})$ w/ B3LYP	0.785	-0.355	-0.411	-0.617	0.344	0.343
$(Zn^{+2}\ 2Im^{-})$ w/ PBE	-	-	-	-0.575	0.325	0.325
Force field parameters [247, 248]	0.651	-0.326	-0.326	-0.848	0.424	0.424

After defining the path, the final part is determining numerically the parameters for surface atoms. From Table 4.1, the charges for monocoordinated Zn atom were obtained as 1.480 and 1.692 e for systems with CO_2 and H_2O, respectively, treated as fixed point charges. An 1x1x1 ZIF-8 nanoparticle terminated in Zn atoms constructed as Fig. 1.6 has a charge of +36 e. If all atoms but the superficial Zn atoms are parametrized with the charges from Hu et al., then those Zn atoms must have a charge of 1.750 e to reach the expected value of +36 e for the whole nanoparticle, see Table 4.5. When removing the superficial Zn from the nanoparticle, its total charge diminishes and until it becomes neutral with only 6 superficial Zn atoms. Those changes impact the Zn atomic charge parameter needed to complete the expected total nanoparticle charge. The chosen values are 1.00 e, same as the bulk parameter, when the nanoparticle is neutral, and range from 1.50 to 1.75 e in positively charged configurations. Those values are similar to the CHELPG charges previously obtained as 1.480 and 1.692 e.

The procedure employed for the superficial H atom bonded to N was similar. The difference lays on a weaker polarization between the pair HN. From Table 4.3, the CHELPG charges are -0.237 and -0.472 for the atom N, 0.272 and 0.327 for the H, depending on the tested system. Thus, the charge values were chosen in the ranges -0.320 to -0.125 and 0.320 to 0.375 for N and H, respectively, see Table 4.5.

In bigger nanoparticles, such as 2x2x2 and 3x3x3, dicoordinated Zn atoms are present, see Fig. 4.1. From Table 4.2, the CO_2 and H_2O fixed point charge systems resulted in CHELPG charges of 1.386 and 1.614 e. Since those values are similar to the ones for monocoordinated Zn atoms, the charges were chosen accordingly as:

- Fully charged 2x2x2 nanoparticle: Monocoordinated Zn $\rightarrow$1.70 e; Dicoordinated Zn $\rightarrow$1.60 e
- Neutral 2x2x2 nanoperticle: Monocoordinated Zn absent; Dicoordinated Zn $\rightarrow$ 1.00 e

Table 4.5: Force field parameters for the $((Zn^{+2})_{24}\ (mIm^{-})_{60}\ (Zn^{+2})_{24})$ nanoparticle where each atom label can be related to Fig. 3.1a as Zn → Zn12; N → N5, N11; C1 → C6; C2 → C1, C3; HC2 → H2, H4; C3 → C7; HC3 → H8, H9, H10.

Bulk atoms [168]	q_i(e)	ϵ_i (kcal/mol)	σ_i(Å)
Zn	1.000	0.0125	1.960
N	-0.500	0.1700	3.250
C1	0.500	0.0860	3.400
C2	-0.100	0.0060	3.400
HC2	0.100	0.0150	2.421
C3	-0.300	0.1094	3.400
HC3	0.100	0.0157	2.650
Surface sites			
$(Zn)_n$	1.000 ($n=6$); 1.500 ($n=12$); 1.625 ($n=16$); 1.700 ($n=20$); 1.750 ($n=24$)	0.0125	1.960
$(N)_n$	-0.320 ($n=12$); -0.183 ($n=18$); -0.125 ($n=24$)	0.1700	3.250
$(HN)_n$	0.320 ($n=12$); 0.350 ($n=18$); 0.375 ($n=24$)	0.0157	1.069

- Fully charged 3x3x3 nanoparticle: Monocoordinated Zn → 1.65 e; Dicoordinated Zn → 1.60 e

All other used parameters were from Table 4.5.

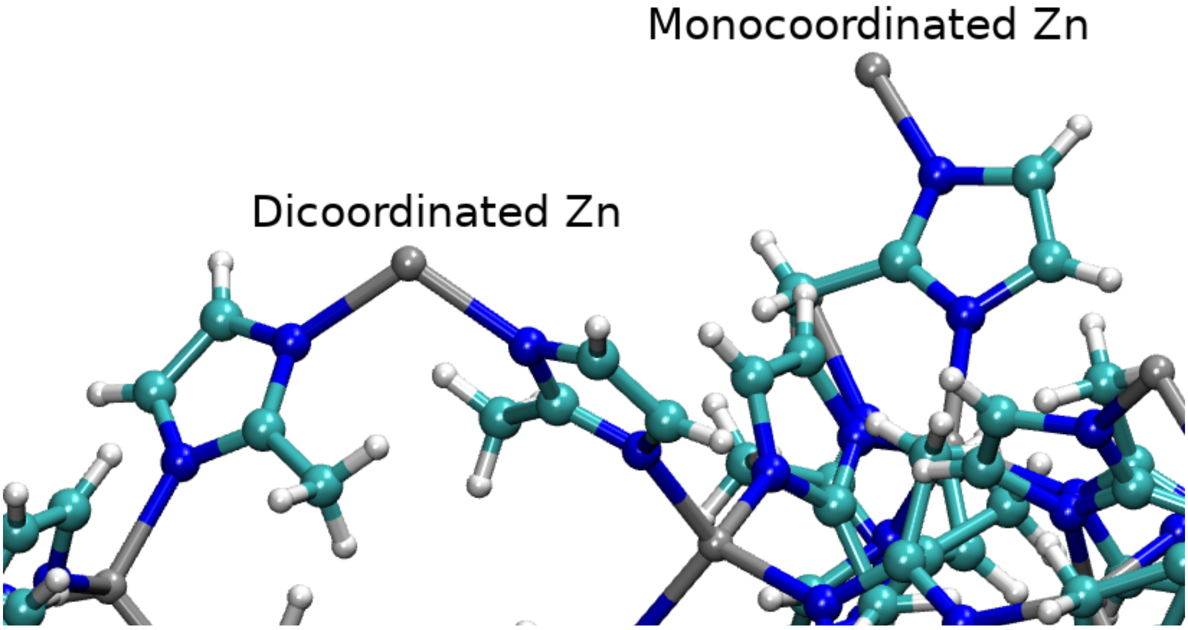

Figure 4.1: Structural model of mono and dicoordinated Zn atoms on the surface of ZIF-8

4.2 Depiction of atmospheric air in a finite container

Due to computational limitations, all simulations run in a finite space, which normally could not represent the atmospheric air. Certain methods, such as periodic boundary conditions (PBC), can mitigate adverse effects from the finite box. However, PBC can make others abnormalities arise if the simulation box is small for the intended system. On the other hand, a huge box implies on a fierce strain for each simulation step.

The first step on the simulation production was the evaluation of how large does the box has to be to avoid artificial effects. The molar density of atmospheric air is quite similar to the ideal gas of 22.4 mol/L under ambient conditions. Then, by fixating this density, the volume can be evaluated by the means of number of particles.

From Fig. 4.2, both the numbers of absorbed CO_2 molecules (N_{in}) and the interaction energy between CO_2 and ZIF-8 reached a reasonable plateau between 1000 and 2000 CO_2 molecules. Then, 1000 gas molecules was chosen as the minimum number for the classic simulations.

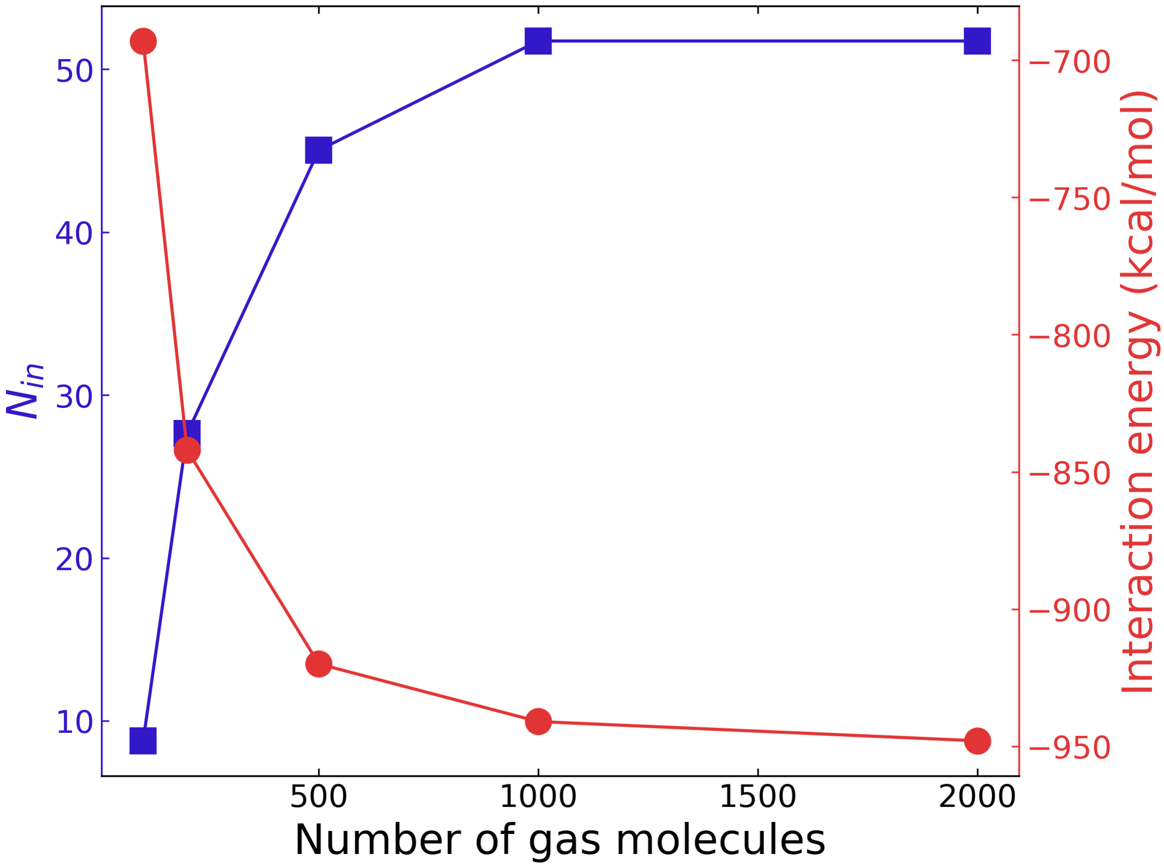

Figure 4.2: Graph of number of absorbed CO_2 molecules (N_{in}) and interaction energy between CO_2 and ZIF-8 versus number of CO_2 molecules present on the MC simulation

4.3 Geometry and energy validations

Although the force field parameters were obtained in a seemingly reasonable way, the results obtained from the classical simulations need to be confronted with results from first principles methods.

A compilation of the observed interaction distance and energy is displayed in Table 4.6. Note the optimized geometries also had their binding energy calculated classically with the previously developed force field parameters.

Table 4.6: Interaction distance and energy of different systems to evaluate the classical force field quality. E_{ij} is the binding energy between solute and gas, in kcal/mol, and R_{Zn-X} is the average distance between superficial Zn atoms and the closest atom X of the gas molecule, in Å. Binding energies obtained from B3LYP/cc-pVDZ are displayed in parenthesis. The cases with MC and BOMD methods were averaged over 5000 configurations from the simulations.

Method	Solute	N_{gas}	CO_2		H_2O		N_2	
			E_{ij}	R_{Zn-O}	E_{ij}	R_{Zn-O}	E_{ij}	R_{Zn-N}
MC	ZIF-8[a]	1000	-15.1	2.21	-62.2	1.93	-8.4	2.26
MC	$(Zn^{+2}\ mIm^-)$	100	-11.5	2.18	-45.5	1.98	-5.7	2.22
OPT	$(Zn^{+2}\ mIm^-)$	3	-11.8	2.12	-41.7	2.08	-6.5	2.21
			(-17.5)		(-34.7)		(-11.9)	
OPT	$(Zn^{+2}\ mIm^-)$	4	-10.5	2.26	-42.1	2.05	-	-
			(-14.7)					
BOMD	$(Zn^{+2}\ mIm^-)$	4	-9.5	2.21	-40.0	2.09	-	-
OPT	$(H^+\ mIm^-)$	1	-2.3	2.28	-7.5	1.99	-1.3	2.46
			(-1.5)		(-5.8)		(-1.0)	

[a] The complete name is $((Zn^{+2})_{24}\ (mIm^-)_{60}\ (Zn^{+2})_{24})^{+36}$

The Fig. 4.3 represents Table 4.6 in a visual manner. The full icons are from classical force field usage, while the hollow ones are from first principle methods. Regarding CO_2, the classic interaction distance was between the values from quantum methods. Similarly, for N_2, the classic interaction distance was almost equal to the quantum value. On the other hand, both interaction energy and distance for H_2O had discrepancies. The superficial Zn atom force field parameters were slightly tweaked to enhance the H_2O representation by increasing the σ of Zn in 7 %, i.e. increased the interaction distance. The H_2O interaction energy displayed a slight reduction from -45 kcal/mol to -43 kcal/mol. However, the binding energies of CO_2 and N_2 were reduced as well. Then, the parameters were reverted to the values already presented. Overall, the H_2O interaction energy and distance differences between classic and quantum methods were about 15 % and 0.1 Å, respectively. Which means, although some discrepancies can be seen, especially with H_2O, the current force field parameters enabled a balance between values for the different gases.

The binding energies of the system $((Zn^{+2})_{24}\ (mIm^-)_{60}\ (Zn^{+2})_{24})$ from Table 4.6 are

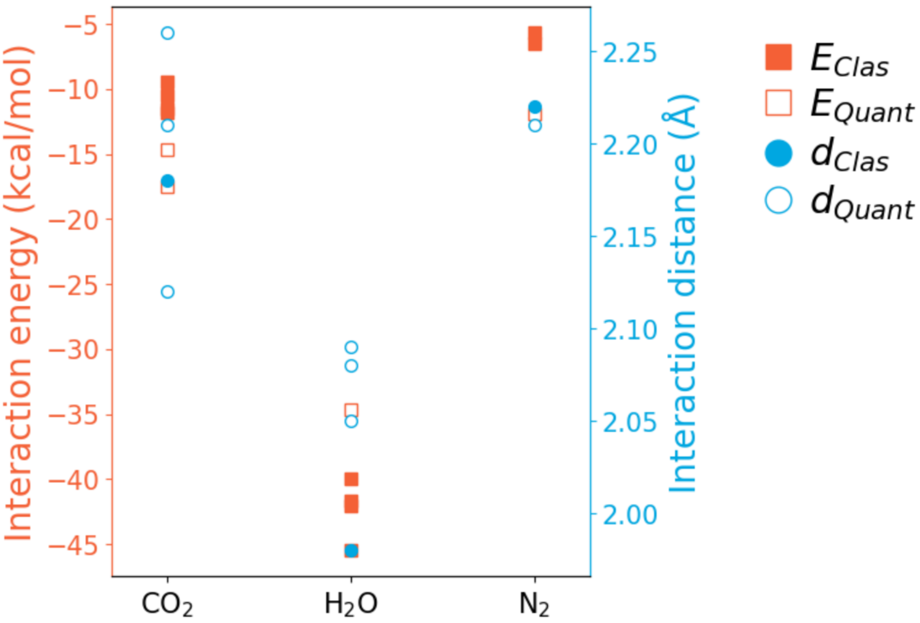

Figure 4.3: Binding energy and distance of $(Zn^{+2}\ mIm^{-})$ with CO_2, H_2O and N_2. The quantities obtained using the classical force field from Table 4.5 are represented by filled icons and the ones obtained from first principle methods are represented by hollow icons.

systematically higher than its counterpart of $(Zn^{+2}\ mIm^{-})$. It is a good sign since the energy is considered between the whole solute molecule with the binding gas molecule. So, a more intense interaction was expected.

The interaction energies between $(H^{+}\ mIm^{-})$ and the gases CO_2 and N_2 are around 2 to 4 times the k_BT value for temperature of 273.15 K. Which means, thermal fluctuation effects are sufficient to disrupt those interactions. Only H_2O can maintain the binding with $(H^{+}\ mIm^{-})$ in ambient temperature. Also, the classic force field represented the interaction with reasonable agreement.

4.4 Initial results: different gases and thermodynamic effects

The CO_2 capture is meant to be done in atmospheric environment, which means temperature and pressure are not strictly constant, and many different gases are present.

4.4.1 Different gases

The results from simulations with different gases are in Fig. 4.4. The first important result from Fig. 4.4 is the almost absent interaction between ZIF-8 and the gases O_2 and Ar. In the literature, those gas species can be captured by ZIF-8, although only at lower temperatures, such as 77 K [256]. Both were not further studied in this work since they pose no competition at atmospheric environment.

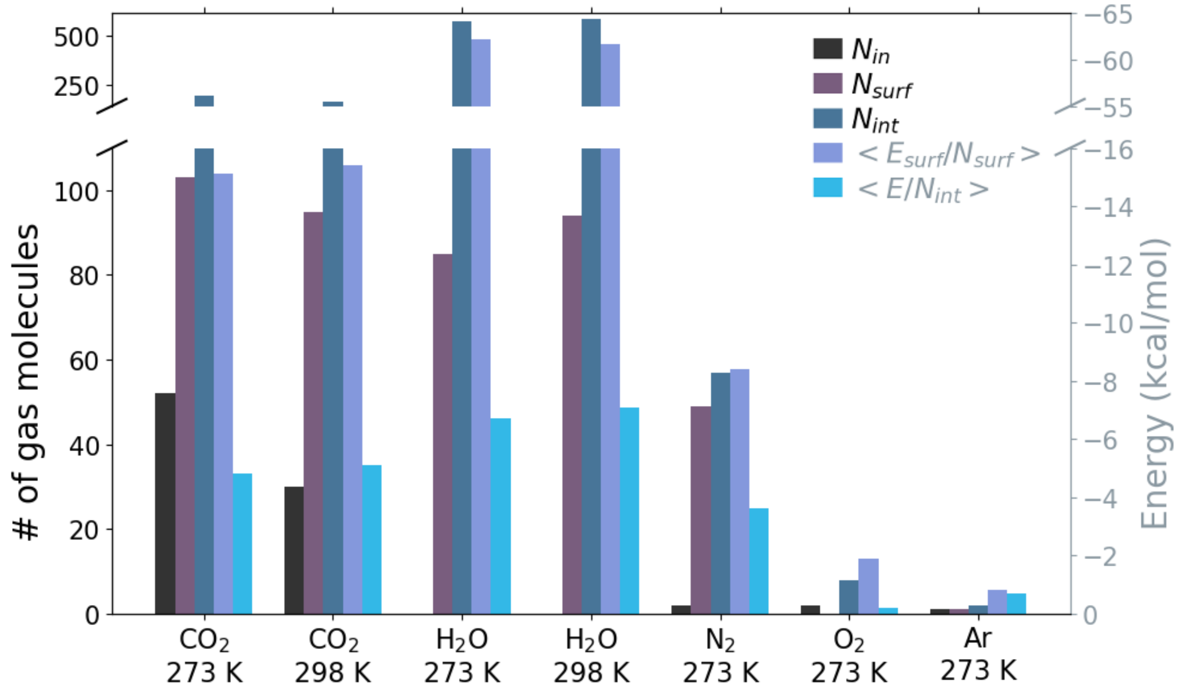

Figure 4.4: Number and interaction energy of captured gas molecules from MC simulations at ambient pressure. N_{in}, N_{surf} and N_{int} are the number of absorbed, adsorbed and interacting gas molecules, respectively. E_{surf} and E are the interaction energy of adsorbed and interacting gas molecules, respectively, in respect to the ZIF-8 nanoparticle given by $((Zn^{+2})_{24}\ (mIm^{-})_{60}\ (Zn^{+2})_{24})^{+36}$.

Only CO_2 was absorbed (N_{in}) in significant amounts considering the remaining three gases. The absence of H_2O was already expected due to the hydrophobicity of the inner cavities of ZIF-8 [163, 257]. Surprisingly, the inner ZIF-8 pores were extremely selective towards CO_2, even among other apolar gases.

On the other hand, the superficial capture (N_{surf}) demonstrates the Zn atoms on the surface are a competitive domain for CO_2, H_2O and N_2. The interaction energy $\langle E_{surf}/N_{surf}\rangle$ is more intense with H_2O than CO_2. Thus, for the fully charged ZIF-8, the surface is dominated by H_2O, while CO_2 is prefered over N_2.

4.4.2 Temperature

The temperature influences CO_2 uptake drastically as the Fig. 4.4 suggests and as seen experimentally [165]. N_{in} of CO_2 decreases about a third over the temperature increase of only 25 K. N_{surf} diminishes over this change, however only slightly. Also, N_{surf} for H_2O increases with growing temperature, which means CO_2 selectivity worsens as well with higher temperatures. Do note the binding energies barely change, the whole effect is exclusive on the uptake amount.

4.4.3 Pressure

The initial simulation box volume had lattice of 334 Å, which is necessary for pristine CO_2 to be at ambient conditions. After the simulation, the box volume decreased by 27.5 %. To put it in perspective, the introduction of a ZIF-8 nanoparticle of about 0.04 % of the total initial volume was sufficient to shrink the box in 27.5 % to maintain atmospheric conditions. Thus, a minuscule particle, in relation to the whole box, managed to compress the total volume by about a fourth. It demonstrates that ZIF-8 has a great potential on CO_2 storage.

An enhanced pressure setup of 20 atm of the same system was tested. The superficial CO_2 capture was marginally increased by only 4 %. However, the inner CO_2 uptake rose by 108 %. Therefore, absorption can be highly enhanced in more pressured environment whereas adsorption barely depends on it.

4.5 Surface effect

Based on the scientific reports for ZIF-8 surface, a multitude of options as surface sites can be found. Among those possibilities, monocoordinated Zn atoms, protons and empty surface sites were simulated. The specific ZIF-8 configurations are the ones expressed in Table 4.5, which account to charges for the whole nanoparticle as depicted in Fig. 4.5.

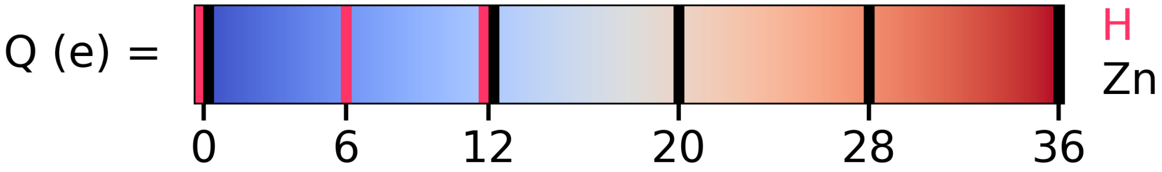

Figure 4.5: Diagram of the charge of the $((Zn^{+2})_{24}\ (mIm^{-})_{60}\ (Zn^{+2})_{24})$ nanoparticle based on its surface composition.

The numbers of absorbed (N_{in}) and adsorbed (N_{surf}) gas molecules are displayed in the Figs. 4.6a and 4.6b. As seen from the Table 4.6, those gases possess weak interactions with the superficial protons.

The N_{in} trend shows that the CO_2 absorption does not increase when more protons are added, but it does increase with more Zn atoms. Also, the absorption of H_2O decreases with the charge increase of the ZIF-8, while the N_2 absorption stays near zero. It is important to note the drastic impact that surface conditions have on the internal gas capture. In summary, ZIF-8 nanoparticles with higher values of charge displayed increased absorption selectivity towards CO_2. Also, more superficial Zn atoms enhanced the sheer CO_2 absorption.

The N_{surf} results are less appealing for CO_2 separation. Although the CO_2 adsorption increased with more Zn atoms on the surface, H_2O and N_2 capture increased as well.

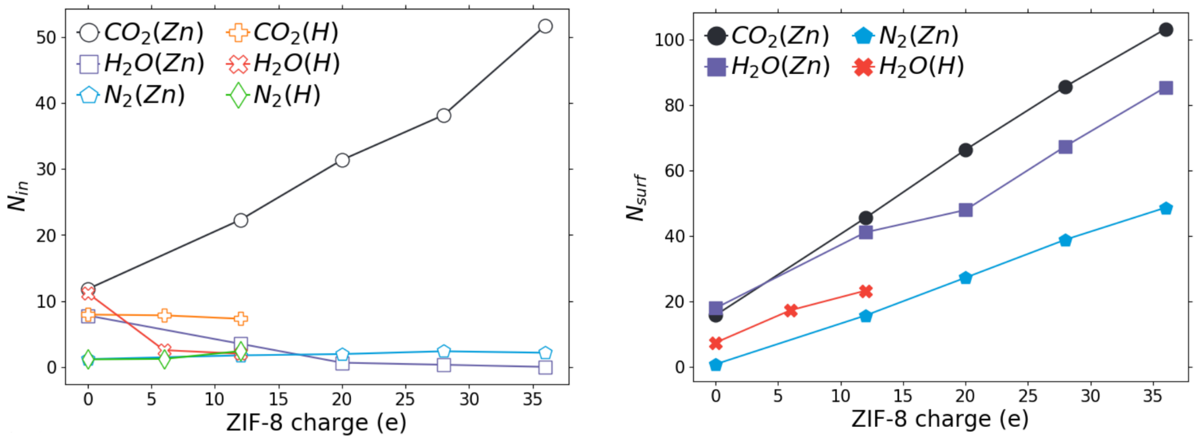

(a) Number of absorbed gas molecules

(b) Number of adsorbed gas molecules

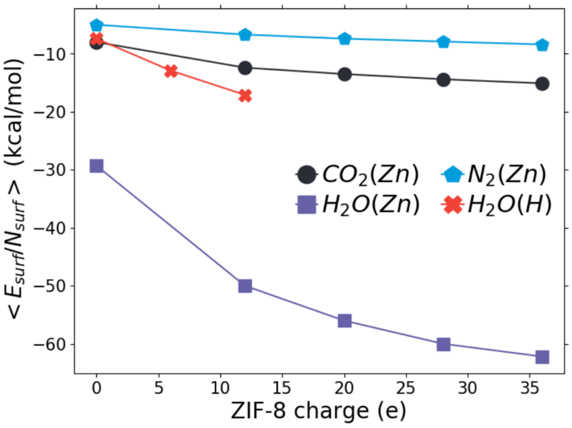

(c) Interaction energy of adsorbed gas molecules

Figure 4.6: Energy and number of captured gas molecules of MC simulations with multiple charge configurations for the ZIF-8 nanoparticle. The atom in parenthesis refers to the surface condition of the ZIF-8 nanoparticle. Note (b) does not have values for CO_2 or N_2 with H at the surface sites since it was constantly null.

Their competition can be verified with the Fig. 4.6c. In all tested circumstances with Zn atoms on the surface sites, H_2O dominated the superficial capture, since its interaction energy is the highest. Also, H_2O is the only captured gas by H superficial atoms. On the other hand, CO_2 has energetic advantage over N_2.

4.6 Molecular dynamics parametrization

Up to this point, all classical simulations were done with a rigid framework by MC. However, MD simulations enable different approaches, such as innately flexible molecules and dynamic measures. Similarly to the intermolecular parameters, the bulk intramolecular ones for ZIF-8 were available in the literature [168]. Those were developed for a bulk bound by PBC, then could be inadequate for a free nanoparticle.

In the first tests of $((Zn^{+2})_{24}\ (mIm^{-})_{60}\ (Zn^{+2})_{24})$ in vacuum, the whole structure maintained most of its integrity but the imidazole rings planarity, see Fig. 4.7. Many gradual adjustments were employed on the dihedrals, both proper and improper, to ensure the expected planarity. The bond and angle intramolecular parameters were kept as the bulk ones from [168]. The dihedrals were extensively strengthened and had some of its phase values changed to reflect better the crystallographic structure until the values in Table 4.7.

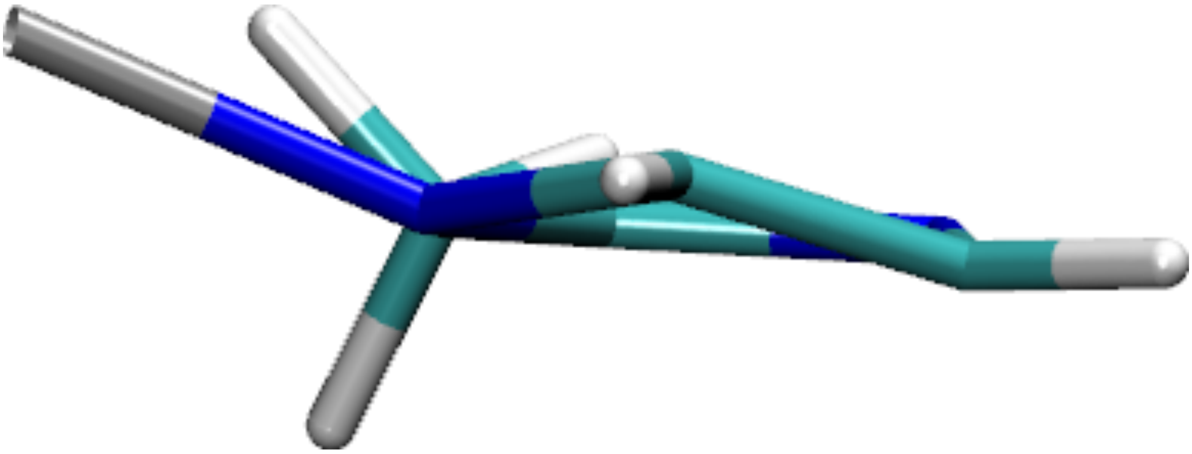

Figure 4.7: Molecular representation of a non-planar imidazole ring from initial MD simulations.

The structure of the ZIF-8 nanoparticle remained stable throughout the whole simulation with root-mean-square deviation (RMSD) approximately constant at 1 Å. Which means the flexible ZIF-8 framework was only slightly different from the crystallographic structure. The newly added flexibility enhanced the CO_2 inner capture by 19 % and the superficial capture by 14 %. It is a welcome boost, but not enough to discredit the MC results.

Regarding the ensemble, NPT simulations could not be made due to the difficulty of setting a barometer for gases. The box size was extremely unstable between steps, then only NVT simulations were done with MD.

4.7 Gas mixtures

The previous simulations were all performed with a solute related to ZIF-8 immersed in a pristine gas. Therefore, no direct competition between different solvents were tested. Analysing the interaction geometries and energies, a reasonable guess can be made on how the competition would happen. However, the confirmation comes from actually simulating them together. Those were carried out with H_2O or N_2 along CO_2, as both were the potential competitors of CO_2.

Table 4.7: Intramolecular dihedral force field parameters for ZIF-8 in the AMBER format. The atom labels are the same as the ones used in Table 4.5 with the addition of Zn1 being the bulk Zn atom and $Zn2$ is the monocoordinated Zn atom.

Dihedrals	V_1	V_2	V_3	γ_1	γ_2	γ_3
Zn1-N-C1-N	0.0	15.0	0.0	0.0	180.0	0.0
Zn1-N-C1-C3	0.0	15.0	0.0	0.0	180.0	0.0
C2-N-C1-N	0.0	15.0	0.0	0.0	180.0	0.0
C2-N-C1-C3	0.0	15.0	0.0	0.0	180.0	0.0
Zn1-N-C2-C2	0.0	15.0	0.0	0.0	180.0	0.0
Zn1-N-C2-HC2	0.0	15.0	0.0	0.0	180.0	0.0
C1-N-C2-C2	0.0	15.0	0.0	0.0	180.0	0.0
C1-N-C2-HC2	0.0	4.8	0.0	0.0	180.0	0.0
N-C2-C2-N	0.0	15.0	0.0	0.0	180.0	0.0
N-C2-C2-HC2	0.0	4.0	0.0	0.0	180.0	0.0
HC2-C2-C2-HC2	0.0	4.0	0.0	0.0	180.0	0.0
N-C1-C3-HC3	0.0	0.0	0.1	0.0	0.0	0.0
C1-N-Zn1-N	0.0	0.0	15.0	0.0	0.0	8.8
C2-N-Zn1-N	0.0	0.0	15.0	0.0	0.0	-171.2
C2-C2-N-Zn2	0.0	15.0	0.0	0.0	180.0	0.0
HC2-C2-N-Zn2	0.0	15.0	0.0	0.0	180.0	0.0
N-C1-N-Zn2	0.0	15.0	0.0	0.0	180.0	0.0
C3-C1-N-Zn2	0.0	15.0	0.0	0.0	180.0	0.0
Improper Dihedrals				V_p		
N-Zn1-C1-C2				15.0		
C1-N-N-C3				15.0		
C2-N-C2-HC2				8.5		
N-C2-C1-Zn2				15.0		

4.7.1 $CO_2 + H_2O$

The real proportion of CO_2:H_2O depends on the local humidity, then 1:1 was used as a general case.

The CO_2 capture suffered a severe blow, the absorption decreased by 83 % while the adsorption became null. Exclusively H_2O was captured by the superficial Zn atoms. In general, MOFs tend to adsorb H_2O in favor of other apolar solvents [39]. Specifically for ZIF-8, the trends of CO_2 absorption and H_2O adsorption were known [194]. However, such an intense impact on the CO_2 absorption was not expected. Thus, H_2O must be removed prior to CO_2 capture attempts.

4.7.2 $CO_2 + N_2$

Differently from the previous case, CO_2:N_2 proportion is immensely favored for N_2 at an atmospheric setup. Firstly, an 1:1 MC simulation was performed. It displayed a decrease on CO_2 absorption by 35 % and almost no change in CO_2 adsorption in comparison to the simulation with CO_2 only. Do note, almost none N_2 molecule was adsorbed or absorbed. The CO_2 absorption was significantly decreased without N_2 closely interacting with the ZIF-8 nanoparticle.

The same system was simulated again, but through MD. The results had displayed a similar trend to the previous MC attempt. In comparison to the MD simulation with only CO_2, it had a decrease on CO_2 absorption by 47 % and no difference on CO_2 adsorption. Also, exclusively CO_2 got captured by ZIF-8 in either the inner pores or the surface sites.

In an attempt to reproduce better the proportion imbalance of CO_2:N_2, an 1:9 MD simulation was performed. This specific proportion was chosen since 10 - 15 % is roughly the CO_2 composition in flue gas. This simulation was not performed by MC since a system of this size would take a long time, while intense paralelization on the MD algorithm of GROMACS enabled larger systems to be tackled. The results were similar to the ones from the previous system, however more drastic. The CO_2 absorption and adsorption decreased by 75 % and by less than 1 %, respectively, when comparing to the MD simulation with CO_2 only. The capture in the inner pores of ZIF-8 was mainly dominated by CO_2, still traces of captured N_2 molecules were found. Although the internal capture of CO_2 diminished, the superficial CO_2 capture by the unsaturated Zn atoms remained unflinched. A possible root for those results could be that this bigger system required a longer termalization, even though the production phase of each simulation was only conducted when the system potential energy reached a minimum average. To test it, the system was simulated from two different initial conditions: 1. random placement for CO_2 and N_2; 2. ZIF-8 already filled with CO_2, while N_2 was randomly placed. However, both conditions led to the same production scenario. Considering volume and temperature were set for the whole gas to have atmospheric pressure, the partial pressure of CO_2 was 0.1 atm in an 1:9 simulation. Then, the results were analogous to the ones observed in Section 4.4.3, an enhanced pressure increased the internal CO_2 capture greatly but was mostly irrelevant for the superficial CO_2 capture.

4.8 CO_2 density

In view of the intense CO_2 compactation provided by ZIF-8, a set of pristine CO_2 simulations were made to compare how similar the latter is to captured CO_2.

The pristine CO_2 simulations had average densities $\langle\rho\rangle$ as displayed in Table 4.8 along with the theoretical expected values [258]. The expected and obtained density values are compatible, which means the used force field parameters for CO_2 are reliable even in significantly different thermodynamic conditions. Those thermodynamic conditions were chosen to represent atmospheric CO_2 and light density liquid CO_2. A diagram of the region with small theorical densities for liquid CO_2 is in Fig. 4.8. It shows the density values around the critical point and it goes as low as 0.583 g/cm^3, but simulations near phase transitions are tricky to be made.

Table 4.8: Pristine CO_2 densities from MC simulations. The value in parenthesis is the standard deviation.

Phase	Pressure (atm)	Temperature (K)	Densities (g/cm^3)	
			$\langle\rho\rangle$	[258]
Gas	1	273.15	0.00198(4)	0.00196
Liquid	10	225.15	1.139(8)	1.148
	72	298.00	0.730(26)	0.758

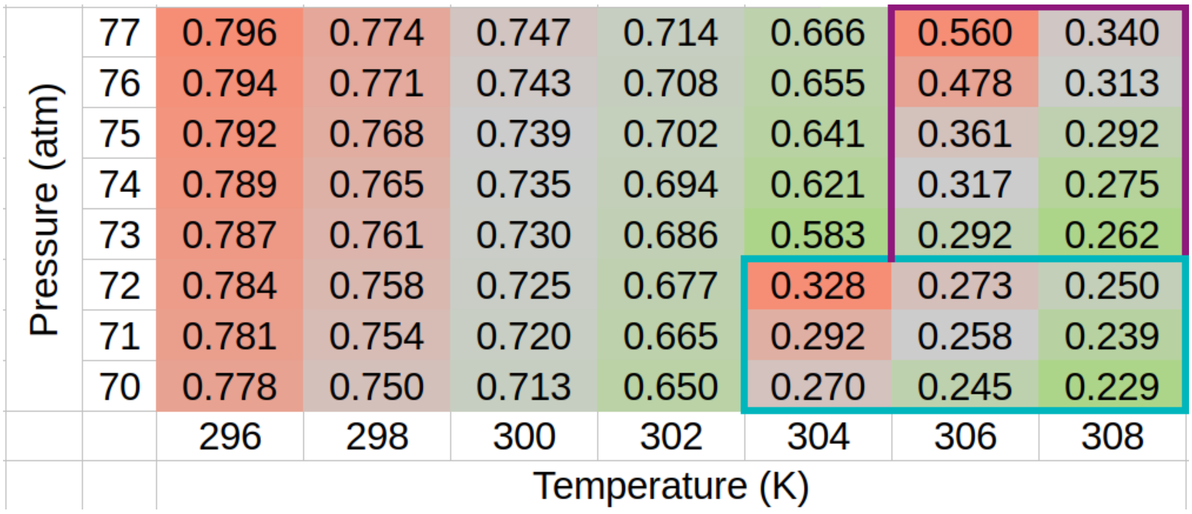

Pressure (atm)	296	298	300	302	304	306	308
77	0.796	0.774	0.747	0.714	0.666	0.560	0.340
76	0.794	0.771	0.743	0.708	0.655	0.478	0.313
75	0.792	0.768	0.739	0.702	0.641	0.361	0.292
74	0.789	0.765	0.735	0.694	0.621	0.317	0.275
73	0.787	0.761	0.730	0.686	0.583	0.292	0.262
72	0.784	0.758	0.725	0.677	0.328	0.273	0.250
71	0.781	0.754	0.720	0.665	0.292	0.258	0.239
70	0.778	0.750	0.713	0.650	0.270	0.245	0.229

Figure 4.8: Diagram of theoretical CO_2 density, in g/cm^3, with values from [258]. The encirclement colors refers to: none – gas phase, teal – liquid phase, purple – supercritical phase.

The structure of the ZIF-8 nanoparticle, $((Zn^{+2})_{24}\ (mIm^{-})_{60}\ (Zn^{+2})_{24})$, was decomposed as suggested in Fig. 4.9. The 1x1x1 ZIF-8 nanoparticle has an approximately spherical shape and was analysed as such. The innermost sphere, named (a), is the biggest pore devoid of ZIF-8 atoms. Moving outwards, the light grey (b) region is heavily populated with ZIF-8 atoms with only slight free space. The dark blue (c) region is an intermediate region with plenty of space for absorbed molecules. Finally, the dark grey (d) region consists of the superficial sites with the adsorbed molecules.

Due to the spherical nature of this nanoparticle, the number of CO_2 molecules was counted by the RDF. Dividing the amount by the free volume, determined as described in Section 3.5.2, densities for each region were obtained as displayed in Table 4.9.

From the MC simulations in Table 4.9 it is clear that the highest CO_2 density region is the external one, (d). Which highlights once more the major importance of the surface conditions on the CO_2 capture. Additionally, when the temperature is increased, the region (a) displays a huge drop on density, followed by region (c), while the (d) maintains most of its density. The ensemble change from NVT to NPT increased the densities only slightly.

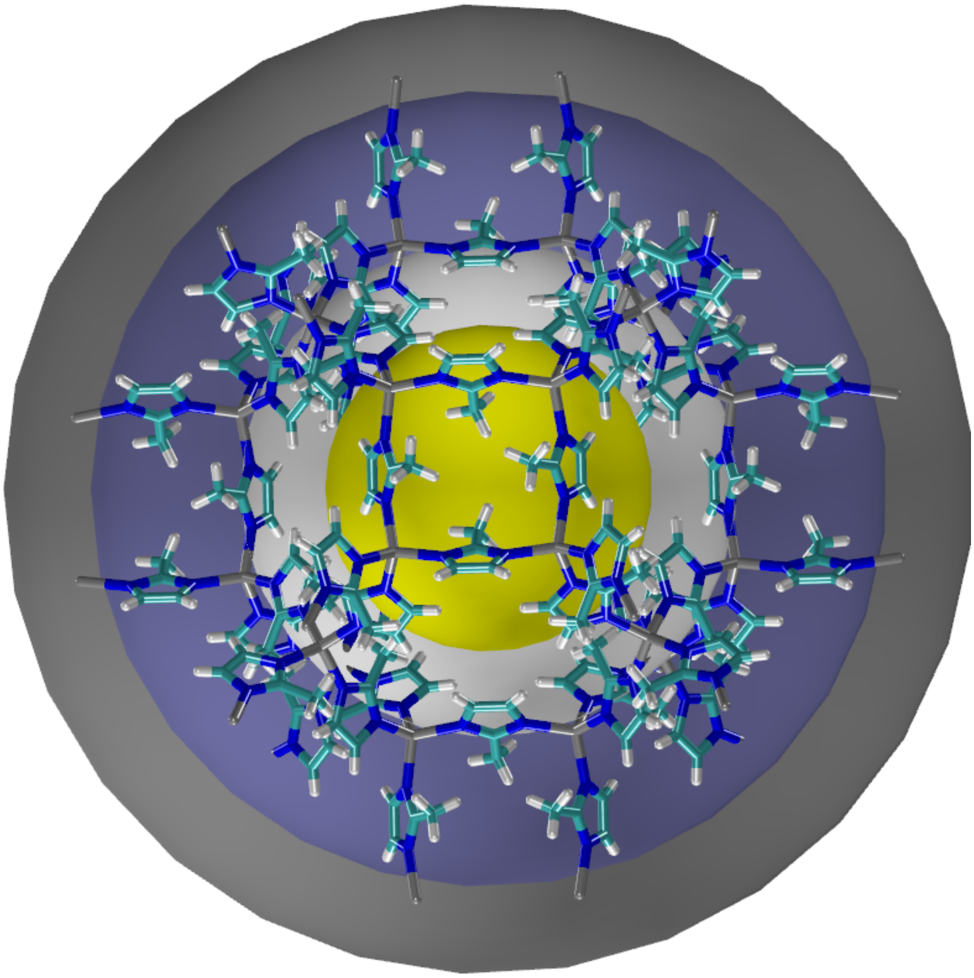

Figure 4.9: Decomposition of spherical regions in the ZIF-8 nanoparticle for the density analysis. The concentric spheres are named as (a) to (d), starting with the yellow and moving outwards.

Table 4.9: Densities of captured CO_2 in different regions, according to Fig. 4.9, of the 1x1x1 ZIF-8 nanoparticle under atmospheric pressure. The region (b) is not shown due to almost null value in all cases.

Simulation	Ensemble	Temperature (K)	Densities (g/cm^3)			
			(a)	(c)	(d)	all
MC	NVT	273.15	0.362	0.344	0.658	0.453
MC	NVT	298.00	0.091	0.209	0.586	0.353
MC	NPT	273.15	0.401	0.378	0.676	0.476
MD	NVT	273.15	0.680	0.392	0.917	0.606
MD[a]	NVT	273.15	0.010	0.027	0.632	0.295

[a] from the simulation with the gases 1000 $CO_2 + 9000\ N_2$

Regarding the MD simulations in Table 4.9, the flexibility enhanced the capture mostly on (a) and secondly on (d). The simulation of the mixture CO_2:N_2 on proportion 1:9 shows how drastically the absorption can be impaired by low CO_2 partial pressure, while the adsorption reached a similar level to the MC simulation.

The flexible ZIF-8 framework immersed in pristine CO_2 attained an average overall density of captured CO_2 of 0.606 g/cm^3. It peaked at 0.917 g/cm^3 in the region (d), which is significantly denser than the pristine CO_2 simulation of 0.730 g/cm^3. Going back to Fig. 4.8, 0.606 g/cm^3 is denser than liquid CO_2 at 73 atm and 304 K, with 0.583 g/cm^3. In other words, the ZIF-8 nanoparticle spontaneously condensed the gaseous CO_2 into low density liquid CO_2.

4.9 Nanoparticle size effect

The fundamental reason why ZIF-8 was chosen to be studied as a nanoparticle is the potential to change its size and evaluate the surface effect. When the nanoparticle is grown, its surface-to-volume ratio diminishes. Then, smaller nanoparticles have proportionally higher surface effect than bigger ones.

A difficult step was the analysis of absorbed CO_2 molecules in non-spherical nanoparticles. The method of counting used so far was based on the RDF, however it does not convey as much information for far from spherical nanoparticles. A huge aid from the developers of the software SuAVE [259] was provided to overcome the counting problem. By defining a set of surface atoms, SuAVE constructs a smooth surface with gaussian functions on the aforesaid atoms. The surface can be constructed as a closed one and all molecules of the required type inside of it are counted.

The results from simulations with nanoparticles of different sizes are in Table 4.10. A higher CO_2 uptake for growing nanoparticles with analogous architecture was just about obvious. The relevant results are the CO_2 density inside of the ZIF-8 nanoparticles and the total loading. There is a clear and steep tendency of internal CO_2 density decrease as the nanoparticle grows, i.e. as the surface-to-volume ratio diminishes. Which demonstrates how impactful the surface is on the inner CO_2 capture.

Table 4.10: Number of absorbed (N_{in}) and adsorbed (N_{surf}) CO_2 molecules, density of captured CO_2 inside the inner pores of ZIF-8 and CO_2 loading regarding both N_{in} and N_{surf}, i.e. mass of captured CO_2 in proportion to mass of ZIF-8. These values are presented for ZIF-8 nanoparticles of different sizes.

Nanoparticle size	N_{in}	N_{surf}	Internal CO_2 density (g/cm^3)	Total Loading (mg/g)
1x1x1	117	120	0.657	1304
2x2x2	195	322	0.210	550
3x3x3	434	605	0.161	393

The CO_2 loading represents the proportion of captured CO_2 mass in comparison to the ZIF-8 nanoparticle mass. As the nanoparticle grows, its efficiency decreases sharply. The overall range of CO_2 loading values by ZIF-8 for atmospheric environment available in the literature are 22 - 60 and 8 - 82 mg/g, for experimental [165, 166, 183] and theoretical [165–

167, 178, 179, 183, 185, 186, 260–263] studies, respectively. The experimental procedures are made with ZIF-8 in different forms, such as films and nanoparticles. However the size of the nanoparticles are orders of magnitude bigger than the ones in Table 4.10. Which means, the values of loading in Table 4.10 are expected to be exceptionally higher than observed experimental values. Similarly, the theoretical works consider the bulk replicated by PBC, i.e. the limit of huge nanoparticles.

Specific interaction factors between monocoordinated Zn atoms and CO_2 such as coordination of CO_2 molecules for each Zn atom, the binding energy and geometry were all indistinguishable among differently sized nanoparticles. Thus, growing the ZIF-8 nanoparticle does not weaken the binding between superficial Zn atoms and CO_2. However it does reduce the availability of superficial Zn in proportion to the bulk due to the smaller surface-to-volume ratio.

Unlike the 1x1x1 ZIF-8 nanoparticle, bigger ones had dicoordinated Zn atoms on the surface. Those were impactful on the adsorption, each binding with 3.4 CO_2 molecules, on average. It is not as attractive as the monocoordinated Zn atoms averaging 5.0 CO_2 molecules, although still important. Monocoordinated Zn atoms are more prone to react with its surrounding molecules than dicoordinated Zn atoms [193, 197, 199–201]. Then, the latter is also capable of contributing considerably in the capture by real synthetized ZIF-8 nanoparticles.

A survey of metal-organic complexes have shown the Zn coordination number is 4 or 6 with frequencies of 59 or 23 %, respectively [264, 265]. Then, the hexacoordinated Zn atoms (coordinated to 1 mIm^- and 5 CO_2) can appear in other circumstances as well.

A last MD simulation on this topic was made with a 2x2x2 ZIF-8 nanoparticle devoid of any monocoordinated Zn atom. This nanoparticle was neutral and the dicoordinated Zn atoms were less polarized. In such scenery, each superficial Zn atom binded with only 1.9 CO_2 molecules in average. Thus, analogously to the trend from the 1x1x1 ZIF-8 nanoparticle, more superficial Zn atoms can enhance the capture potential of the nanoparticle even without direct interaction to it.

4.10 CO_2 diffusivity

After discussing long about how many gas molecules are captured by ZIF-8, an important question that arises is about the stability of those newformed bindings. In an environment filled with more CO_2 to be captured, the resilience of the binding with the ZIF-8 can be overlooked. However, considering a flux of gas with CO_2 going through the ZIF-8 for it to act as a filter, it would be important to not leak too much CO_2. On the other hand, a fierce binding would require a high energy cost regeneration procedure.

An unexplored facet of the CO_2 capture so far in this work relies on dynamic quantities. While MC simulations do not have an estabilished timeline between frames, the MD simulations are built upon a time ordered structure. Then, diffusion coefficients can be obtained to assess the likelihood of captured CO_2 molecules staying as such.

The fits obtained as described in Section 3.5.3 are displayed in Fig. 4.10. By the Einstein relation, A is the diffusion coefficient, however from Fig. 4.10a it can be seen that A fluctuates strongly. Which is why 10 trajectory fragments were made, so that $\langle A \rangle$ would be more accurate.

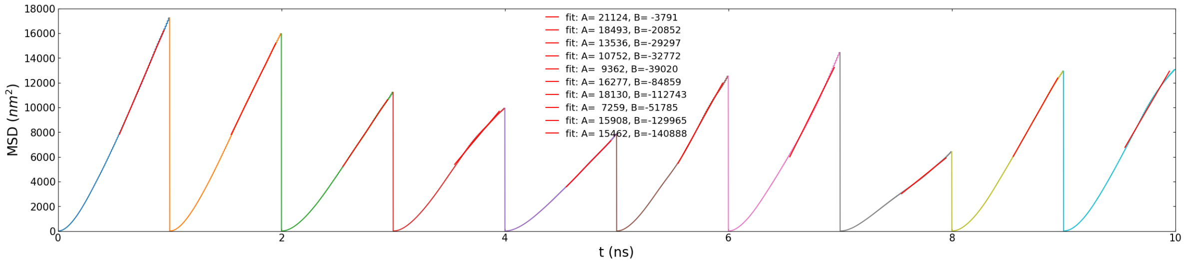

(a) CO_2 "in"

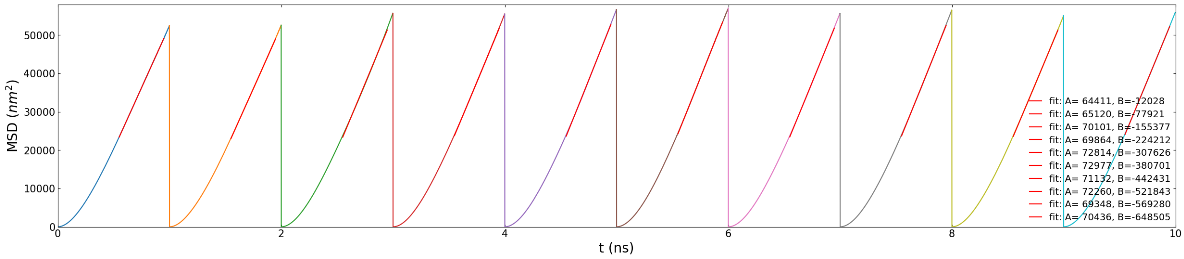

(b) CO_2 "out"

Figure 4.10: MSD of CO_2 molecules from MD simulation with the least squares fit $y = Ax + B$. The difference between (a) and (b) is detailed in Section 3.5.3

The coefficient diffusions were $\langle D_{in} \rangle = 14.630(3) nm^2/ps$ and $\langle D_{out} \rangle = 69.846(5)$ nm^2/ps. The value in parenthesis is the standard deviation. Which means, absorbed CO_2 molecules diffuse four to five times slower than non-absorbed ones. While it is not proof of outstanding retaining potential, it is a rather good sign.

4.11 Absorption characteristic time

The previous topics explored the evolution of systems in equilibrium, i.e., post thermalization process. Yet a noteworthy part of the operation lies on the gas capture by a non loaded molecule of ZIF-8.

The distance between the centers of mass of ZIF-8 and the i-th gas molecule is named d_i. The average of d_i over all values of i is $\langle d \rangle$. Considering L to be the simulation box lattice, the highest value possible for d_i is half of the internal box diagonal, i.e. $L\sqrt{3}/2$. Thus, the quantity to represent the capture process of gas by ZIF-8 is $\langle d \rangle / (L\sqrt{3}/2)$, as shown in Fig. 4.11. The curves were fit by an orthogonal distance regression algorithm, which considered time correlations, of the form $y_0 + A_j \exp(-t/\tau_j)$. In this model, y_0 is the constant reached when the system reaches equilibrium, A_j is an auxiliary constant for the fit and τ_j is the characteristic capture time.

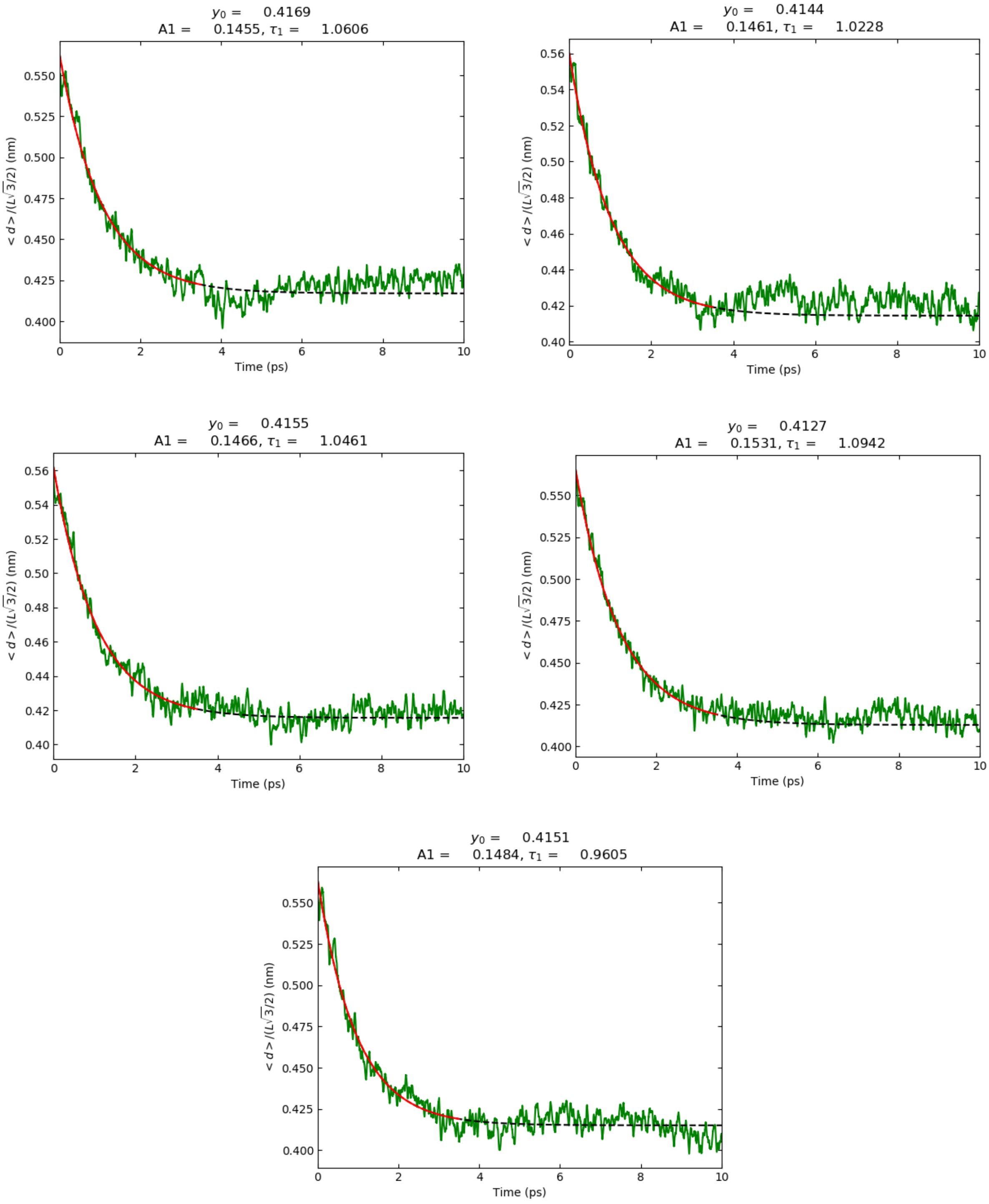

Figure 4.11: Graphs of the normalized average distance d between the centers of mass of CO_2 and ZIF-8. The fitting curve is $y_0 + A_j \exp(-t/\tau_j)$.

All simulations shown in Fig. 4.11 were randomly generated and are equally representative. Thus, the CO_2 normalized average of the equilibrium constant and the characteristic CO_2 capture times yield 0.148(3) and 1.04(5) ns, respectively, with standard deviation in parenthesis. The results for N_2 were 0.060(4) and 0.28(3) ns. The first value could act as a compactation parameter, which shows ZIF-8 is capable of compacting CO_2 2.5 times more than N_2. On the other hand, the characteristic capture time is 3.7 times slower for CO_2 than for N_2. It might be due to the stronger compactation which demands a longer time.

4.12 Adsorbed CO_2 structure

Adsorbed CO_2 on the ZIF-8 nanoparticle form a web of CO_2. Some frame superpositions are in Fig. 4.12 where the dots represent CO_2 molecules. On Figs. 4.12a, 4.12c and 4.12d, the clouds inside a green circle represent a strongly localized CO_2 molecule binding with two superficial Zn atoms. The clouds in yellow rings are adsorbed CO_2 molecules binding with a single Zn atom. Those are less localized, but still clear. However, the blue rings hold the most revealing results, they encircle clouds which are CO_2 molecules that do not interact closely with any atom of the ZIF-8 nanoparticle. Those molecules are captured by the interaction with the CO_2 molecules from the green and yellow rings by their quadrupole interaction. There is a web of CO_2 molecules captured indirectly by the surface of ZIF-8, mediated by the truly adsorbed CO_2 molecules.

The interaction between CO_2 molecules that are either directly or indirectly adsorbed is given by the graphs in Fig. 4.13. Although the pair interaction energy seems weak in comparison to k_BT, which is 0.5 kcal/mol, it is strong enough to maintain the structure. The solid phase of CO_2 which exists in conditions closer to the ambient has a $C - O$ distance of 3.18 Å, a $C - OC$ angle of 133.7^o and, considering the force field parameters used in this work, interaction energy of -0.80 kcal/mol. The modal value of both distance and energy is similar, while the angle distribution is probably composed of two patterns combined, one with a peak similar to solid CO_2 and another around 160^o. Along these lines, the CO_2 molecules organize themselves in a similar fashion to solid phase CO_2 mixed with another angular structure. It reinforces the point that ZIF-8 can spontaneously change the phase state of CO_2 to a composition of liquid and solid states.

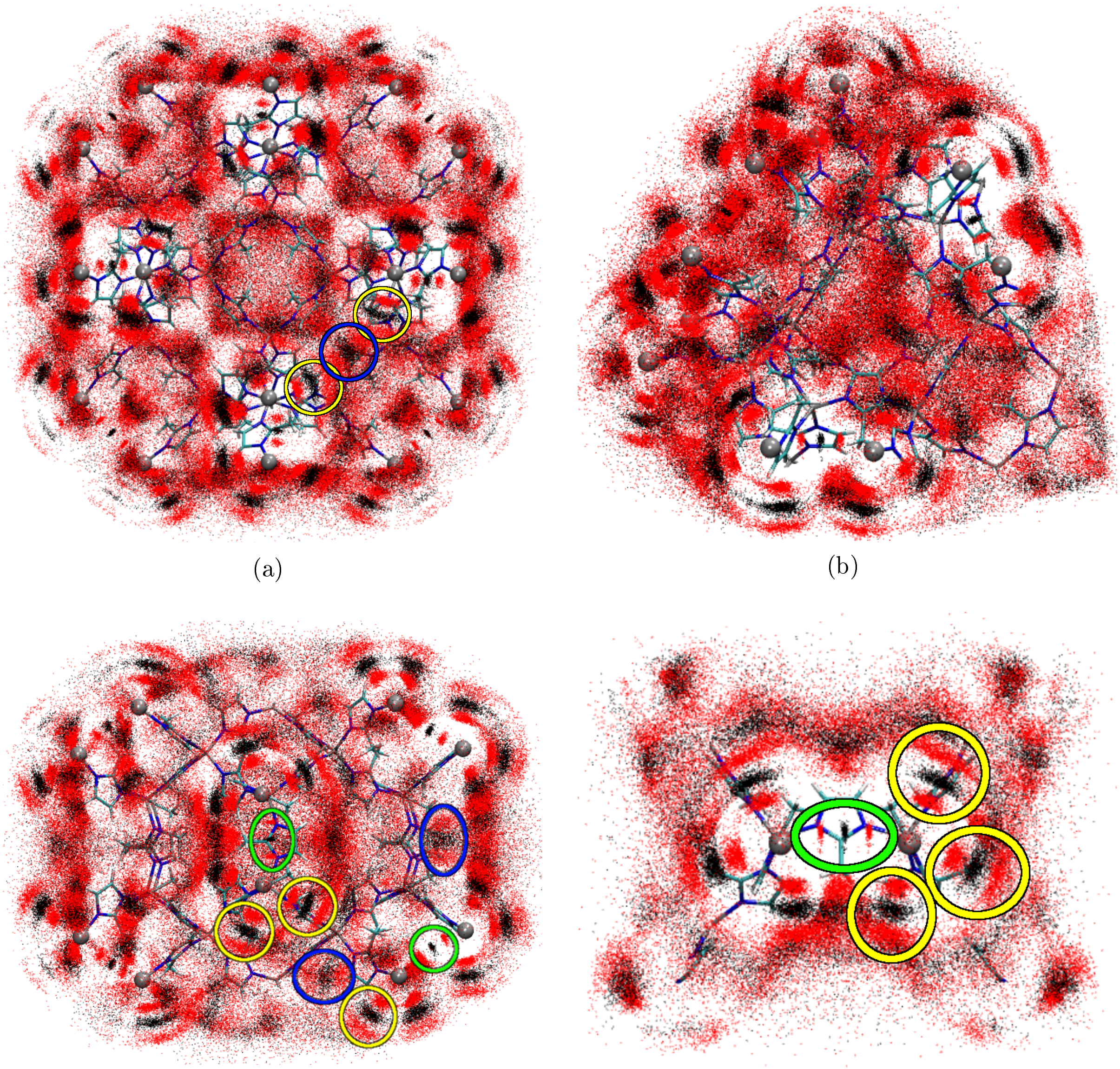

(a) (b)

(c) (d)

Figure 4.12: Frame superpositions from a MC simulation of $((Zn^{+2})_{24}$ $(mIm^{-})_{60}$ $(Zn^{+2})_{24}) + 1000$ CO_2 with the ZIF-8 nanoparticle aligned on top of each other. Each image had its molecular structure cut for better visualization. The big atom spheres are the superficial Zn atoms, while the black and red dots are C and O atoms, respectively, both from CO_2. (a), (c) and (d) have rings with the following meaning based on its color: green, localized CO_2 molecule between two superficial Zn atoms; yellow, captured CO_2 molecule on the surface; blue, CO_2 molecule captured by the quadrupole interaction of the neighbor CO_2 molecules.

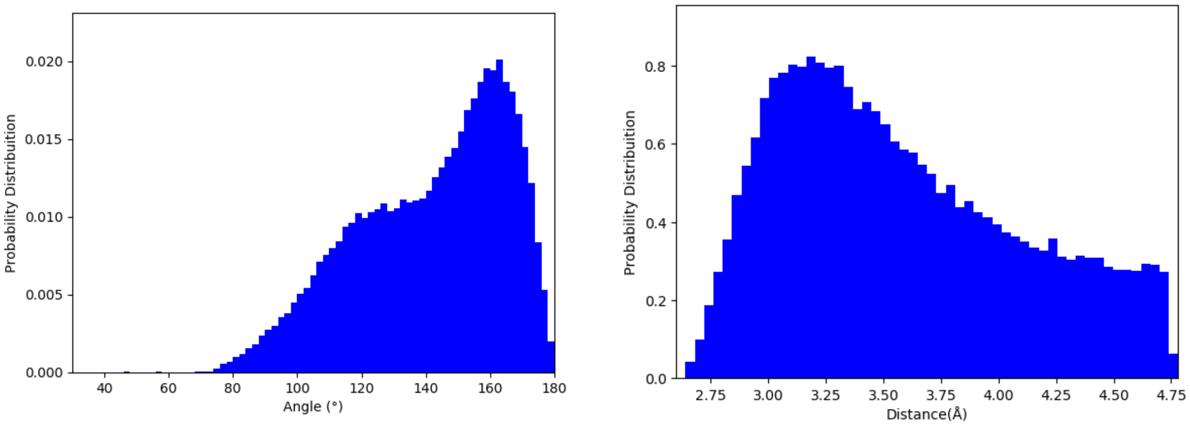

(a) Angle $O - CO$

(b) Distance $C - O$

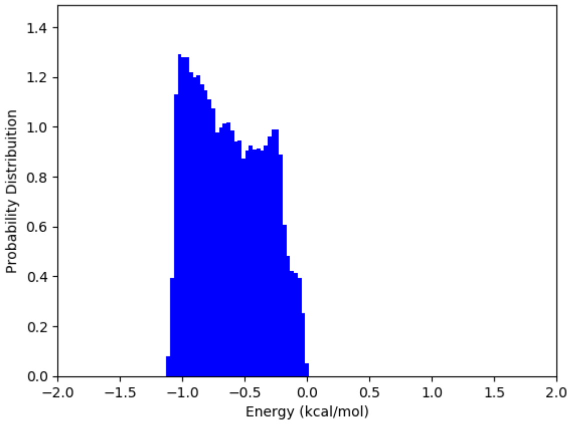

(c) Interaction energy

Figure 4.13: Distributions of the interaction between the CO_2 molecules in the adsorbed web on the ZIF-8 nanoparticle.

5

Conclusions

In this chapter the results are summarized and discussed. The focused topics are construction of the model to be simulated, evaluation of gas competition and thermodynamic conditions, impact of ZIF-8 framework and CO_2 *response for interacting with ZIF-8.*

"Mystery creates wonder and wonder is the basis of man's desire to understand."
Neil Armstrong

The atmosphere of Earth has an alarming concentration of CO_2 which continues to rise due to anthropogenic CO_2 emissions. CO_2 is fundamental on the greenhouse effect and its intensification is a prominent threat to life diversity and quality on Earth. While methods to reduce emissions are valuable, negative emission technologies are needed from economical and logistical points of view. Direct air capture can greatly aid on this field, with CO_2 capture by metal-organic frameworks (MOFs) being a vast field of study. Among the considered MOFs in the literature for this job, zinc-methylimidazolate framework-8 (ZIF-8) was found to be an outstanding candidate for CO_2 capture.

This work had the objective of studying the capture of atmosheric gases (CO_2, H_2O, N_2, O_2 and Ar) by ZIF-8 through theoretical means. Multiple works were already performed, and are available in the literature, on the same subject. However, the surface of ZIF-8 is rarely ever taken into consideration. Mostly because the treatment of surface conditions of MOFs is an intricate problem, while their bulk structures are better estabilished throughout the literature. Thus, along with results for the ZIF-8, this work is also oriented to assist future treatments of other MOFs, specifically on the surface conditions domain.

The form of ZIF-8 that was chosen as a study subject is the nanoparticle. It has both bulk and surface present and changing its size allows the comparison of their effects, since the surface-to-volume ratio varies with the nanoparticle size.

Molecular simulations of different sorts, such as Classic Monte Carlo (MC), Classic Molecular Dynamics (MD) and Born-Oppenheimer Molecular Dynamics (BOMD) were employed. Electronic structure calculations were used as well to reach satisfactory classic models and infer on its quality. The numerous forms of ZIF-8 fragments and nanoparticles were constructed both by crystallographic data and by geometry optimization. The analysis procedures relied on molecular counts, radial distribution functions (RDFs), probability distributions, diffusion coefficients and visual evaluations. Those operations were made mostly by external softwares or scripts developed by the author. Then, along with the study of the problem at hand, a comprehensive learning of programming was attained.

Multiple molecular quantities were analysed to study the interaction between ZIF-8 and atmospheric gases. Those were atomic charges; interaction geometries and energies; gas capture coordinations; amount of absorbed and adsorbed gas molecules; gas densities, diffusivities and conformations.

The conclusions that arose from the simulations and analysis are summarized in the following topics.

5.1 Initial treatment

The parametrization began by calculating charges for the ZIF-8 fragments. Although parameters were already available in the literature, those were meant for the bulk region. Then, electronic structure calculations were employed on multiple systems to obtain CHELPG charges and validate them.

B3LYP as a method to obtain CHELPG charges is a common method throughout the literature. It was successfully applied on the systems composed of a ZIF-8 fragment with some CO_2 or H_2O molecules, as they were the most important gases on this study. Also, CO_2 and H_2O had to be treated as pontual charges since their polarization could not be represented on the employed force field model. Lastly, the parametrized ZIF-8 was simulated and the geometries and energies were compared to validate the force field. This procedure is not meant only to recapitulate the results section. It is to serve as a guideline for future works since treatment of the surface of MOFs is a difficult matter to approach.

Moving onto the flexible framework, the parametrized charges caused an abnormal behaviour of the imidazole rings. The imidazole rings near the surface were heavily distorted. To circumvent it, the dihedral force constants were strengthened until a reasonable planarity of the rings was achieved. Thus, although the charges seemed to work properly and no distortion was seen on the small fragments, an inspection must be conducted on the whole simulated nanoparticle.

5.2 Effects of different gases and thermodynamic conditions

The most abundant atmospheric gases are N_2, O_2, H_2O, Ar and CO_2. Their sizes are similar and are all apolar, except for H_2O. Which means developing a selective mechanism to capture exclusively CO_2 is highly delicate. Yet, the inner pores of ZIF-8 are capable of capturing only CO_2 among the five studied gases. The surface capture was not as selective and could adsorb H_2O, CO_2 and N_2, in this energetic order.

Up to this point, the gases were treated separately. Based on its results, absorption was expected to be dominated by CO_2 and adsorption by H_2O, with CO_2 following behind. The actual competition test was made by simulating pairs of gases together with the ZIF-8 nanoparticle. The CO_2/H_2O competition was vastly disadvantageous for CO_2. Adsorption worked as expected, but surprisingly the absorption also took a severe blow. In summary, CO_2 capture by ZIF-8 can only be performed in a dehumidified media. CO_2/N_2 competition was different. The adsorption was dominated by CO_2, as the interaction energies suggested. The absorption was greatly diminished, but its extent depended on what the CO_2 partial pressure was set at. The more unbalanced setup of 1:9 for CO_2:N_2 caused a purge of molecules from inside of ZIF-8. Due to the dominance of CO_2 molecules interacting directly with ZIF-8, N_2 could barely approach its vicinity. Which means, N_2 has a faint impact on the CO_2 absorption, with only trace N_2 capture, and no effect on the CO_2 adsorption. However, the small CO_2 partial pressure of 0.1 atm was responsible for the CO_2 absorption decay. The CO_2 partial pressure in atmospheric environment is sharply lower than 0.1 atm, which means absorption of CO_2 would be unlikely, however adsorption was mostly unaffected and could become the main capture method.

The previous results were obtained for atmospheric conditions, however those can fluctuate in a real setting. Higher temperatures were found to not only drastically reduce the CO_2 capture but also to increase the H_2O adsorption. Then, both CO_2 intake and selectivity are enhanced by lower temperatures.

Currently there are projects already working to capture CO_2 from atmospheric air. Some use turbines to increase the pressure of the inlet beyond the atmospheric value. The higher pressure setup simulated was greatly above the atmospheric pressure to check for this possibility. It was found to be extremely impactful on the CO_2 absorption, but only marginally significant on the adsorption.

5.3 Nanoparticle effects

ZIF-8 was simulated with multiple different conditions, which affected its charge and surface composition. The surface sites of the ZIF-8 nanoparticle could be filled with Zn or H atoms or be left empty. CO_2 capture was found to have higher uptake and selectivity whenever more Zn atoms were available on the surface. It implies the ZIF-8 nanoparticle had a higher charge, however increasing its charge by adding protons on the surface sites caused no change on the CO_2 capture. In summary, ZIF-8 nanoparticles with higher density of Zn atoms can capture CO_2 more efficiently, not necessarily the ones more positively charged. Note that even the absorption is greatly dependant on the superficial Zn density.

Bigger ZIF-8 nanoparticles were tested and displayed an acute decrease on the CO_2 loading in relation to the smaller one. The surface-to-volume ratio also decreases as the nanoparticle is grown. Once again, it reinforces the impact of the surface effect on the overall CO_2 capture. Even when the surface sites were kept in a similar fashion, fully filled by Zn atoms, the expansion of bulk over surface was enough to extensively cripple the CO_2 loading.

5.4 CO_2 structure and behaviour

As the main gas for this study, CO_2 had received special attention. It was simulated as a pristine substance to be compared with the captured CO_2. The average density of CO_2 in ZIF-8 is comparable to pristine low density liquid CO_2. Then, density-wise ZIF-8 can spontaneously condense CO_2. Additionally, this capture was performed in about 1 ns for the 1x1x1 ZIF-8 nanoparticle.

Adsorbed CO_2 promotes a web of CO_2 molecules around the ZIF-8 nanoparticle. The structure of this web resembles the geometry of solid phase CO_2. So, structure-wise ZIF-8 can compose a framework related to solid CO_2.

Thus, ZIF-8 is capable of compacting and ordering CO_2 in a manner unlike the gas phase. It possibilits a multitude of applications regarding not only capture, but also storage of CO_2. For the latter, gas competition can be overlooked, which was the weak point of ZIF-8 in an atmospheric setting. The diffusivity also reflects how absorbed CO_2 molecules are less mobile than external ones and are more inclined to stay inside ZIF-8.

The Zn atoms on the surface of ZIF-8 can provide an outstanding CO_2 loading potential, in both density and structure. Two proposals of applications arise from such ability. The first is by creating imperfections in the bulk of ZIF-8, more undercoordinated Zn atoms would be available and could create artificial surface sites within the inner pores. Secondly, nanoparticles of ZIF-8 could be deposited on a supporting media, which would create a membrane of ZIF-8 with an extensive superficial area.

Bibliography

[1] IPCC, *Climate Change 2007: The scientific Basis. Contribution of working group I to the fourth assessment report of the intergovernmental panel on climate change*, 2007.

[2] J.-g. Lu, M.-d. Cheng, Y. Ji, and H. Zhang, "Membrane-based co2 absorption into blended amine solutions", Journal of Fuel Chemistry and Technology **37**, 740–746 (2009).

[3] Q. S. S. Nahin, *Greenhouse Effect*, http://blog.nigurha.com/greenhouse-effect/, Accessed: 2020/09/15, 2019.

[4] NOAA National Centers for Environmental Information, *State of the Climate: Global Climate Report for 2019*, https://www.ncdc.noaa.gov/sotc/global/201913 /supplemental/page-3, Accessed: 2020/09/15, 2020.

[5] A. Yamasaki, "An overview of co2 mitigation options for global warming-emphasizing co2 sequestration options", Journal of Chemical Engineering of Japan **36**, 361–375 (2003).

[6] IPCC, *Policymaker's summary of the scientific assessment of climate change; report to IPCC from working group*, 1990.

[7] A. A. Olajire, "CO2 capture and separation technologies for end-of-pipe applications - A review", Energy **35**, 2610–2628 (2010).

[8] M. K. Mondal, H. K. Balsora, and P. Varshney, "Progress and trends in CO2 capture/separation technologies: A review", Energy **46**, 431–441 (2012).

[9] D. Vuuren, E. Stehfest, M. Elzen, T. Kram, J. Vliet, S. Deetman, M. Isaac, K. Klein Goldewijk, A. Hof, A. Mendoza Beltran, R. Oostenrijk, and B. van Ruijven, "Rcp2.6: exploring the possibility to keep global mean temperature increase below 2^oc", Climatic Change **109**, 95–116 (2011).

[10] R. Socolow, *Wedges Reaffirmed*, www.thebulletin.org/, Accessed: 2020-08-17, 2011.

[11] C. Stewart and M.-A. Hessami, "A study of methods of carbon dioxide capture and sequestration—the sustainability of a photosynthetic bioreactor approach", Energy Conversion and Management **46**, 403–420 (2005).

[12] T. Stocker, D. Qin, G.-K. Plattner, M. Tignor, S. Allen, J. Boschung, A. Nauels, Y. Xia, V. Bex, and P. Midgley, *Climate Change 2013: The Physical Science Basis Working Group I Contribution to the Fifth Assessment Report of the Intergovernmental Panel on Climate Change*, Cambridge, United Kingdom and New York, NY, 2013.

[13] E. Post, M. C. Forchhammer, M. S. Bret-Harte, T. V. Callaghan, T. R. Christensen, B. Elberling, A. D. Fox, O. Gilg, D. S. Hik, T. T. Høye, R. A. Ims, E. Jeppesen, D. R. Klein, J. Madsen, A. D. McGuire, S. Rysgaard, D. E. Schindler, I. Stirling, M. P. Tamstorf, N. J. Tyler, R. van der Wal, J. Welker, P. A. Wookey, N. M. Schmidt, and P. Aastrup, "Ecological dynamics across the arctic associated with recent climate change", Science **325**, 1355–1358 (2009).

[14] International Energy Agency, *Energy technology transitions for industry. Strategies for the Next Industrial Revolution* (2009).

[15] T. Kuramochi, A. Ramírez, W. Turkenburg, and A. Faaij, "Comparative assessment of co2 capture technologies for carbon-intensive industrial processes", Progress in Energy and Combustion Science **38**, 87–112 (2012).

[16] D. Aaron and C. Tsouris, "Separation of CO2 from flue gas: A review", in Separation science and technology (2005).

[17] IPCC, *Climate change 2001: impacts, adaptation and vulnerability. Contribution of Working Group II to the Third Assessment Report of the Intergovernmental Panel on Climate Change*, 2001.

[18] E. N. Lightfoot and M. C. M. Cockrem, "What are dilute solutions?", Separation Science and Technology **22**, 165–189 (1987).

[19] C. Breyer, D. Bogdanov, A. Aghahosseini, A. Gulagi, M. Child, A. S. Oyewo, J. Farfan, K. Sadovskaia, and P. Vainikka, "Solar photovoltaics demand for the global energy transition in the power sector", Progress in Photovoltaics: Research and Applications **26**, 505–523 (2018).

[20] M. Z. Jacobson, M. A. Delucchi, Z. A. Bauer, S. C. Goodman, W. E. Chapman, M. A. Cameron, C. Bozonnat, L. Chobadi, H. A. Clonts, P. Enevoldsen, J. R. Erwin, S. N. Fobi, O. K. Goldstrom, E. M. Hennessy, J. Liu, J. Lo, C. B. Meyer, S. B. Morris, K. R. Moy, P. L. O'Neill, I. Petkov, S. Redfern, R. Schucker, M. A. Sontag, J. Wang, E. Weiner, and A. S. Yachanin, "100% clean and renewable wind, water, and sunlight all-sector energy roadmaps for 139 countries of the world", Joule **1**, 108–121 (2017).

[21] B. Mathiesen, H. Lund, D. Connolly, H. Wenzel, P. Ostergaard, B. Möller, S. Nielsen, I. Ridjan, P. Karnoe, K. Sperling, and F. Hvelplund, "Smart energy systems for coherent 100% renewable energy and transport solutions", Applied Energy **145**, 139–154 (2015).

[22] M. Ram, D. Bogdanov, A. Aghahosseini, A. Oyewo, A. Gulagi, M. Child, H.-J. Fell, and C. Breyer, *Global Energy System Based on 100% Renewable Energy e Power Sector*, http://bitly.com/2hU4Bn9, Accessed: 2018-05-10, 2017.

[23] S. Sgouridis, D. Csala, and U. Bardi, "The sower's way: quantifying the narrowing net-energy pathways to a global energy transition", Environmental Research Letters **11**, 094009 (2016).

[24] M. Fasihi, O. Efimova, and C. Breyer, "Techno-economic assessment of CO 2 direct air capture plants", Journal of Cleaner Production **224**, 957–980 (2019).

[25] J. Farfan, M. Fasihi, and C. Breyer, "Trends in the global cement industry and opportunities for long-term sustainable ccu potential for power-to-x", Journal of Cleaner Production **217**, 821–835 (2019).

[26] D. R. Lide, *CRC Handbook of Chemistry and Physics*, 76th (CRC-Press, 1997), pp. 2375–2378.

[27] C. N. Hewitt and P. Brimblecombe, *Air Composition and Chemistry.* 2nd (Cambridge University Press, 1996), pp. 1–2.

[28] R. Barry and R. Chorley, *Atmosphere, Weather and Climate*, 9th (Routledge, London, 2010), pp. 1–3 / 13–14.

[29] F. K. Lutgens and E. J. Tarbuck, *The Atmosphere: An Introduction to Meteorology*, 12th (Pearson, 2013), pp. 17–25.

[30] F. T. Mackenzie and J. A. MacKenzie, *Our Changing Planet: Earth System Science and Global Environmental Change*, 1st (Pearson, 1995), pp. 288–307.

[31] B. J. Finlayson-Pitts and J. N. J. Pitts, *Chemistry of the Upper and Lower Atmosphere: Theory, Experiments, and Applications*, 1st (Elsevier Science, 1999), pp. 37, 561–567.

[32] J. PEARSON and G. R. STEWART, "The deposition of atmospheric ammonia and its effects on plants", New Phytologist **125**, 283–305 (1993).

[33] M. T. Kleinman, R. F. Phalen, W. J. Mautz, R. C. Mannix, T. R. McClure, and T. T. Crocker, "Health effects of acid aerosols formed by atmospheric mixtures.", Environmental Health Perspectives **79**, 137–145 (1989).

[34] A. Neftel, E. Moor, H. Oeschger, and B. Stauffer, "Evidence from polar ice cores for the increase in atmospheric CO2 in the past two centuries", Nature **315**, 45–47 (1985).

[35] D. M. Etheridge, L. P. Steele, R. L. Langenfelds, R. J. Francey, J.-M. Barnola, and V. I. Morgan, "Natural and anthropogenic changes in atmospheric co2 over the last 1000 years from air in antarctic ice and firn", Journal of Geophysical Research: Atmospheres **101**, 4115–4128 (1996).

[36] A. Indermuhle, T. Stocker, F. Joos, H. Fischer, H. Smith, M. Wahlen, B. Deck, D. Mastroianni, J. Tschumi, T. Blunier, R. Meyer, and B. Stauffer, "Holocene carbon-cycle dynamics based on co2 trapped in ice at taylor dome, antarctica", Nature **398**, 121–126 (1999).

[37] IPCC, *Climate change 2001: the scientific basis. Contribution of working group I to the third assessment report of the intergovernmental panel on climate change*, 2001.

[38] C. D. Keeling, S. C. Piper, R. B. Bacastow, M. Wahlen, T. P. Whorf, M. Heimann, and H. A. Meijer, "Atmospheric CO2 and 13CO2 Exchange with the Terrestrial Biosphere and Oceans from 1978 to 2000: Observations and Carbon Cycle Implications", in *A history of atmospheric co2 and its effects on plants, animals, and ecosystems*, edited by I. T. Baldwin, M. M. Caldwell, G. Heldmaier, R. B. Jackson, O. L. Lange, H. A. Mooney, E.-D. Schulze, U. Sommer, J. R. Ehleringer, M. Denise Dearing, and T. E. Cerling (Springer New York, New York, NY, 2005), pp. 83–113.

[39] B. P. Spigarelli and S. K. Kawatra, "Opportunities and challenges in carbon dioxide capture", Journal of CO2 Utilization **1**, 69–87 (2013).

[40] M. Hasib-ur-Rahman, M. Siaj, and F. Larachi, "Ionic liquids for CO2 capture-Development and progress", Chemical Engineering and Processing: Process Intensification **49**, 313–322 (2010).

[41] M. Ramdin, T. W. De Loos, and T. J. Vlugt, "State-of-the-art of CO 2 capture with ionic liquids", Industrial and Engineering Chemistry Research **51**, 8149–8177 (2012).

[42] C. H. Yu, C. H. Huang, and C. S. Tan, "A review of CO2 capture by absorption and adsorption", Aerosol and Air Quality Research **12**, 745–769 (2012).

[43] A. Meisen and X. Shuai, “Research and development issues in co2 capture”, Energy Conversion and Management **38**, Proceedings of the Third International Conference on Carbon Dioxide Removal, S37–S42 (1997).

[44] P. Riemer, “Greenhouse gas mitigation technologies, an overview of the co2 capture, storage and future activities of the iea greenhouse gas r&d programme”, Energy Conversion and Management **37**, Proceedings of the International Energy Agency Greenhouse Gases: Mitigation Options Conference, 665–670 (1996).

[45] S. Wong and R. Bioletti, *Carbon dioxide separation technologies. In: Carbon and energy management*, 2002.

[46] A. R. Kulkarni and D. S. Sholl, “Analysis of equilibrium-based TSA processes for direct capture of CO 2 from Air”, Industrial and Engineering Chemistry Research **51**, 8631–8645 (2012).

[47] D. Keith, M. Hà Duong, and J. Stolaroff, “Climate strategy with co2 capture from the air”, Climatic Change **74**, 17–45 (2006).

[48] K. Lackner, “Capture of carbon dioxide from ambient air”, The European Physical Journal Special Topics **176**, 93–106 (2009).

[49] J. C. Fisher II, J. Tanthana, and S. S. Chuang, “Oxide-supported tetraethylenepentamine for co2 capture”, Environmental Progress & Sustainable Energy **28**, 589–598 (2009).

[50] IMTE AG Consulting Engineers, *Exploring the many carbon capture options*, https://www.mrsphoto.net/4-IMTE%20AG/2-2009-3.pdf, Accessed: 2020-08-17, 2009.

[51] D. Leeson, N. Mac Dowell, N. Shah, C. Petit, and P. Fennell, “A techno-economic analysis and systematic review of carbon capture and storage (ccs) applied to the iron and steel, cement, oil refining and pulp and paper industries, as well as other high purity sources”, International Journal of Greenhouse Gas Control **61**, 71–84 (2017).

[52] SAPEA, *Novel Carbon Capture and Utilisation Technologies: Research and Climate Aspects. SAPEA Evidence Review Report No. 2, Berlin, Germany*, https://www.sapea.info/wp-content/uploads/CCU-report-proof3-for-23-May.pdf, Accessed: 2018-05-27, 2018.

[53] E. S. Sanz-Pérez, C. R. Murdock, S. A. Didas, and C. W. Jones, “Direct Capture of CO2 from Ambient Air”, Chemical Reviews **116**, 11840–11876 (2016).

[54] K. Z. House, A. C. Baclig, M. Ranjan, E. A. Van Nierop, J. Wilcox, and H. J. Herzog, “Economic and energetic analysis of capturing CO2from ambient air”, Proceedings of the National Academy of Sciences of the United States of America **108**, 20428–20433 (2011).

[55] J. Yu, L. H. Xie, J. R. Li, Y. Ma, J. M. Seminario, and P. B. Balbuena, “CO2 Capture and Separations Using MOFs: Computational and Experimental Studies”, Chemical Reviews **117**, 9674–9754 (2017).

[56] K. Greenwood and M. Pearce, “The removal of carbon dioxide from atmospheric air by scrubbing with caustic soda in packed towers”, Chemical Engineering Research and Design **31a**, 201–207 (1953).

[57] N. McGlashan, N. Shah, B. Caldecott, and M. Workman, “High-level techno-economic assessment of negative emissions technologies”, Process Safety and Environmental Protection **90**, Special Issue: Negative emissions technology, 501–510 (2012).

[58] C. Pritchard, A. Yang, P. Holmes, and M. Wilkinson, “Thermodynamics, economics and systems thinking: What role for air capture of CO2?”, Process Safety and Environmental Protection **94**, 188–195 (2015).

[59] European Academies Science Advisory Council (EASAC), *Negative emission technologies: What role in meeting Paris Agreement targets?* (2018).

[60] J. C. Minx, W. F. Lamb, M. W. Callaghan, S. Fuss, J. Hilaire, F. Creutzig, T. Amann, T. Beringer, W. de Oliveira Garcia, J. Hartmann, T. Khanna, D. Lenzi, G. Luderer, G. F. Nemet, J. Rogelj, P. Smith, J. L. V. Vicente, J. Wilcox, and M. del Mar Zamora Dominguez, “Negative emissions – part 1: research landscape and synthesis”, Environmental Research Letters **13**, 063001 (2018).

[61] C. J. E. Bajamundi, J. Koponen, V. Ruuskanen, J. Elfving, A. Kosonen, J. Kauppinen, and J. Ahola, “Capturing CO2 from air: Technical performance and process control improvement”, Journal of CO2 Utilization **30**, 232–239 (2019).

[62] Z. Hu, Y. Wang, B. B. Shah, and D. Zhao, “ CO 2 Capture in Metal-Organic Framework Adsorbents: An Engineering Perspective ”, Advanced Sustainable Systems **3**, 1800080 (2019).

[63] M. Broehm, J. Strefler, and N. Bauer, “Techno-Economic Review of Direct Air Capture Systems for Large Scale Mitigation of Atmospheric CO2”, SSRN Electronic Journal, 1–28 (2015).

[64] S. Choi, J. H. Drese, P. M. Eisenberger, and C. W. Jones, “Application of amine-tethered solid sorbents for direct co2 capture from the ambient air”, Environmental Science & Technology **45**, 2420–2427 (2011).

[65] McKinsey and Company, *Carbon capture and storage: Assessing the economics.* http://assets.wwf.ch/downloads/mckinsey2008.pdf, Accessed: 2011-11-07, 2008.

[66] A. Kohl and R. Nielsen, *Gas Purification*, 5th (Gulf Professional Publishing, Houston, 1997).

[67] J. Isobe, P. Henson, A. MacKnight, S. Yates, D. Schuck, and D. Winton, “Carbon dioxide removal technologies for U.S. Space vehicles: past, present, and future”, in 6 th international conference on environmental systems (2016).

[68] NASA, *Closing the Loop Recycling Water and Air in Space*, https://www.nasa.gov/pdf/146558main_RecyclingEDA(final)4_10_06.pdf, Accessed: 2018-07-27, 2006.

[69] R. Boyda, C. Miller, and M. Schwartz, “Integrated air revitalization system for Space Station”, in Sixteenth international conference on environmental systems (1986), pp. 331–343.

[70] D. J. Rendell, M. Clarke, and M. Evans, “The effect of environmental conditions on the absorption of Carbon Dioxide using soda lime”, in Sae technical papers (2003).

[71] N. Spector and B. Dodge, “Removal of carbon dioxide from atmospheric air”, Trans Am Inst Chem Eng **42**, 827–848 (1946).

[72] N. Johnston, D. Blake, F. Rowland, S. Elliott, K. Lackner, H. Ziock, M. Dubey, H. Hanson, and S. Barr, “Chemical transport modeling of potential atmospheric co2 sinks”, Energy Conversion and Management **44**, 681–689 (2003).

[73] J. Elfving, C. Bajamundi, J. Kauppinen, and T. Sainio, “Modelling of equilibrium working capacity of PSA, TSA and TVSA processes for CO2 adsorption under direct air capture conditions”, Journal of CO2 Utilization **22**, 270–277 (2017).

[74] A. Kumar, D. G. Madden, M. Lusi, K. J. Chen, E. A. Daniels, T. Curtin, J. J. Perry, and M. J. Zaworotko, "Direct Air Capture of CO2 by Physisorbent Materials", Angewandte Chemie - International Edition **54**, 14372–14377 (2015).

[75] D. W. Keith, G. Holmes, D. St. Angelo, and K. Heidel, "A Process for Capturing CO2 from the Atmosphere", Joule **2**, 1573–1594 (2018).

[76] O. Shekhah, Y. Belmabkhout, Z. Chen, V. Guillerm, A. Cairns, K. Adil, and M. Eddaoudi, "Made-to-order metal-organic frameworks for trace carbon dioxide removal and air capture", Nature Communications **5**, 1–7 (2014).

[77] D. G. Madden, H. S. Scott, A. Kumar, K.-j. Chen, R. Sanii, A. Bajpai, M. Lusi, T. Curtin, J. J. Perry, M. J. Zaworotko, and T. Curtin, "Flue-gas and direct-air capture of CO 2 by porous metal – organic materials Subject Areas : Authors for correspondence :" Philosophical Transactions of the Royal Society A: Mathematical, Physical and Engineering Sciences **375**, 2084–2094 (2017).

[78] W. R. Lee, S. Y. Hwang, D. W. Ryu, K. S. Lim, S. S. Han, D. Moon, J. Choi, and C. S. Hong, "Diamine-functionalized metal–organic framework: exceptionally high co2 capacities from ambient air and flue gas, ultrafast co2 uptake rate, and adsorption mechanism", Energy Environ. Sci. **7**, 744–751 (2014).

[79] T. Grant Glover, G. W. Peterson, B. J. Schindler, D. Britt, and O. Yaghi, "Mof-74 building unit has a direct impact on toxic gas adsorption", Chemical Engineering Science **66**, 163–170 (2011).

[80] L. J. Wang, H. Deng, H. Furukawa, F. Gándara, K. E. Cordova, D. Peri, and O. M. Yaghi, "Synthesis and characterization of metal–organic framework-74 containing 2, 4, 6, 8, and 10 different metals", Inorganic Chemistry **53**, 5881–5883 (2014).

[81] A. Ö. Yazaydın, R. Q. Snurr, T.-H. Park, K. Koh, J. Liu, M. D. LeVan, A. I. Benin, P. Jakubczak, M. Lanuza, D. B. Galloway, J. J. Low, and R. R. Willis, "Screening of metal-organic frameworks for carbon dioxide capture from flue gas using a combined experimental and modeling approach", Journal of the American Chemical Society **131**, 18198–18199 (2009).

[82] Carbon Engineering, *Team and Board*, http://carbonengineering.com/company-profile/, Accessed: 2018-01-15, 2018.

[83] Climeworks, *About us*, http://www.climeworks.com/about/, Accessed: 2018-02-05, 2018.

[84] C. Gebald, J. A. Wurzbacher, and A. Steinfeld, *Amine Containing Fibrous Structure for Adsorption of CO2 from Atmospheric Air*, Patent number US20120076711, 2012.

[85] C. Gebald, N. Piatkowski, T. Ruesch, and J. A. Wurzbacher, *Low-Pressure Drop Structure of Particle Adsorbent Bed for Adsorption Gas Separation Process*, Patent numbers US9751039 and US20160074803, 2014.

[86] J. A. Wurzbacher and C. Gebald, *Distributed Building-Integrated Carbon Dioxide Extraction System Reducing Fresh Air Requirements*, Patent number WO2013075981A3, 2012.

[87] C. Gebald, T. Zimmerman, and P. Tingaut, *Porous Adsorbent Structure for Adsorption of CO2 from a Gas Mixture*, Patent number US20140134088, 2014.

[88] C. Gebald, N. Repond, and J. A. Wurzbacher, *Steam Assisted Vacuum Desorption Process for Carbon Dioxide Capture*, Patent numbers US10279306 and US20170203249, 2015.

[89] C. Gebald, W. Meier, N. Repond, T. Ruesch, and J. A. Wurzbacher, *Direct Air Capture Device*, Patent numbers US10232305 and US20170106330, 2015.

[90] Global Thermostat, *About Global Thermostat*, https://globalthermostat.com/ about-global-thermostat/, Accessed: 2018-01-15, 2018.

[91] P. M. Eisenberger and G. Chichilnisky, *System and Method for Removing Carbon Dioxide from an Atmosphere and Global Thermostat Using the Same*, Patent numbers US8894747, US9061237, US9925488, US20140004016, US20140130670 and US20150027308, 2014.

[92] S. Choi, J. H. Drese, R. R. Chance, P. M. Eisenberger, and C. W. Jones, *Application of Amine-Tethered Solid Sorbents to CO2 Fixation from Air*, Patent number US8491705, 2013.

[93] P. M. Eisenberger, *System and Method for Carbon Dioxide Capture and Sequestration*, Patent numbers US8500855 and US20140010719, 2013.

[94] P. M. Eisenberger, *Carbon Dioxide Capture/Regeneration Structures and Techniques*, Patent numbers USUS8163066 and US20110041688, 2012.

[95] Antecy, *About us*, http://www.antecy.com/about-us/, Accessed: 2018-02-05.

[96] Hydrocell, *Direct Air Capture (DAC) Appliances*, http://hydrocell.fi/en/air-cleaners-carbon-dioxide-filters-and-dac-appliances/dac-appliances/, Accessed: 2018-05-25, 2018.

[97] C. Bajamundi, *Progress Presentation on CO2 Capture Device Acquisition*, http://www.neocarbonenergy.fi/wp-content/uploads/2016/02/12_Bajamundi.pdf, Accessed: 2018-05-24, 2015.

[98] C. Bajamundi, J. Elfving, and J. Kauppinen, “Assessment of the performance of a bench scale direct air capture device operated at outdoor environment”, in International conference on negative co2 emissions (2018).

[99] Skytree, *CO2 Removal*, https://www.skytree.eu/direct-air-capture/, Accessed: 2018-05-28.

[100] Y. Ishimoto, M. Sugiyama, E. Kato, R. Moriyama, K. Tsuzuki, and A. Kurosawa, *Putting costs of direct air capture in context*, https://papers.ssrn.com/sol3/papers.cfm?abstract_id142982422, Accessed: 2018-05-30, 2017.

[101] Infinitree, *Company's Website*, http://www.infinitreellc.com/technology/, Accessed: 2018-05-28, 2018.

[102] K. S. Lackner and P. Liu, *Removal of Carbon Dioxide from Air*, Patent number US20100095842, 2010.

[103] A. B. Wright, K. S. Lackner, and U. Ginster, *Method and Apparatus for Extracting Carbon Dioxide from Air*, Patent numbers US8273160 and US8337589, 2012.

[104] K. S. Lackner and A. B. Wright, *Removal of Carbon Dioxide from Air*, Patent numbers US8133305 and US20120058032, 2012.

[105] A. B. Wright, K. S. Lackner, and U. Ginster, *Method and Apparatus for Extracting Carbon Dioxide from Air*, Patent numbers US7708806, US8083836, US8273160, US8337589, US20100105126, US20110027142, US20110027143, US20110027157, US20110033357, US20110033358, US20110079144, US20110079146, US20110079147, US20110079149, US20110079150, US20110081709, US20110081710, US20110081712 and US20110083554, 2010.

[106] D. Ruthven, "Co2 capture: value functions, separative work and process economics", Chemical Engineering Science **114**, 128–133 (2014).

[107] M. Ranjan and H. J. Herzog, "Feasibility of air capture", in Energy procedia (2011).

[108] E. I. Koytsoumpa, C. Bergins, and E. Kakaras, "The CO2 economy: Review of CO2 capture and reuse technologies", Journal of Supercritical Fluids **132**, 3–16 (2018).

[109] F. D. Meylan, V. Moreau, and S. Erkman, "CO2 utilization in the perspective of industrial ecology, an overview", Journal of CO2 Utilization **12**, 101–108 (2015).

[110] J. Wilcox, P. C. Psarras, and S. Liguori, "Assessment of reasonable opportunities for direct air capture", Environmental Research Letters **12**, 065001 (2017).

[111] A. Dibenedetto, A. Angelini, and P. Stufano, "Use of carbon dioxide as feedstock for chemicals and fuels: homogeneous and heterogeneous catalysis", Journal of Chemical Technology & Biotechnology **89**, 334–353 (2014).

[112] C. Barnhart, M. Carbajales-Dale, A. Brandt, and S. Benson, "The energetic implications of curtailing versus storing solar- and wind-generated electricity", Energy & Environmental Science **6**, 2804 (2013).

[113] K.-K. Cheng, X.-B. Zhao, J. Zeng, and J.-A. Zhang, "Biotechnological production of succinic acid: current state and perspectives", Biofuels, Bioproducts and Biorefining **6**, 302–318 (2012).

[114] J. K. Stolaroff, G. V. Lowry, and D. W. Keith, "Using cao- and mgo-rich industrial waste streams for carbon sequestration", Energy Conversion and Management **46**, 687–699 (2005).

[115] K. Lackner, P. Grimes, and H. Ziock, "Capturing carbon dioxide from air", in Proceedings of the first national conference on carbon sequestration (2001).

[116] F. Zeman, "Energy and material balance of co2 capture from ambient air", Environmental Science & Technology **41**, 7558–7563 (2007).

[117] R. Baciocchi, G. Storti, and M. Mazzotti, "Process design and energy requirements for the capture of carbon dioxide from air", Chemical Engineering and Processing: Process Intensification **45**, 1047–1058 (2006).

[118] J. K. Stolaroff, D. W. Keith, and G. V. Lowry, "Carbon dioxide capture from atmospheric air using sodium hydroxide spray", Environmental Science & Technology **42**, 2728–2735 (2008).

[119] Q. Yang, V. Guillerm, F. Ragon, A. D. Wiersum, P. L. Llewellyn, C. Zhong, T. Devic, C. Serre, and G. Maurin, "Ch4 storage and co2 capture in highly porous zirconium oxide based metal–organic frameworks", Chem. Commun. **48**, 9831–9833 (2012).

[120] M. Eddaoudi, J. Kim, N. Rosi, D. Vodak, J. Wachter, M. O'Keeffe, and O. M. Yaghi, "Systematic design of pore size and functionality in isoreticular mofs and their application in methane storage", Science **295**, 469–472 (2002).

[121] H. Chae, D. Siberio-Pérez, J. Kim, Y. Go, M. Eddaoudi, A. Matzger, M. O'Keeffe, and O. Yaghi, "A route to high surface area, porosity and inclusion of large molecules in crystals", Nature **427**, 523–527 (2004).

[122] C. Serre, C. Mellot-Draznieks, S. Surblé, N. Audebrand, Y. Filinchuk, and G. Férey, "Role of solvent-host interactions that lead to very large swelling of hybrid frameworks", Science **315**, 1828–1831 (2007).

[123] S. Kitagawa, R. Kitaura, and S.-i. Noro, "Functional porous coordination polymers", Angewandte Chemie International Edition **43**, 2334–2375 (2004).

[124] H. Furukawa, K. E. Cordova, M. O'Keeffe, and O. M. Yaghi, "The chemistry and applications of metal-organic frameworks", Science **341**, 1230444 (2013).

[125] H. Zhang, R. Zou, and Y. Zhao, "Macrocycle-based metal-organic frameworks", Coordination Chemistry Reviews **292**, 74–90 (2015).

[126] Y. Zeng, R. Zou, and Y. Zhao, "Covalent organic frameworks for CO2 capture", Advanced Materials **28**, 2855–2873 (2016).

[127] J.-R. Li, R. J. Kuppler, and H.-C. Zhou, "Selective gas adsorption and separation in metal–organic frameworks", Chem. Soc. Rev. **38**, 1477–1504 (2009).

[128] K. Sumida, D. L. Rogow, J. A. Mason, T. M. McDonald, E. D. Bloch, Z. R. Herm, T.-H. Bae, and J. R. Long, "Carbon dioxide capture in metal–organic frameworks", Chemical Reviews **112**, 724–781 (2012).

[129] S. Chaemchuen, N. A. Kabir, K. Zhou, and F. Verpoort, "Metal–organic frameworks for upgrading biogas via co2 adsorption to biogas green energy", Chem. Soc. Rev. **42**, 9304–9332 (2013).

[130] G. Férey, C. Serre, T. Devic, G. Maurin, H. Jobic, P. L. Llewellyn, G. De Weireld, A. Vimont, M. Daturi, and J.-S. Chang, "Why hybrid porous solids capture greenhouse gases?", Chem. Soc. Rev. **40**, 550–562 (2011).

[131] J. M. Simmons, H. Wu, W. Zhou, and T. Yildirim, "Carbon capture in metal–organic frameworks—a comparative study", Energy Environ. Sci. **4**, 2177–2185 (2011).

[132] Z. Zhang, Z.-Z. Yao, S. Xiang, and B. Chen, "Perspective of microporous metal–organic frameworks for co2 capture and separation", Energy Environ. Sci. **7**, 2868–2899 (2014).

[133] B. Wang, A. Côté, H. Furukawa, M. O'Keeffe, and O. Yaghi, "Colossal cages in zeolitic imidazolate frameworks as selective carbon dioxide reservoirs", Nature **453**, 207–211 (2008).

[134] S. Keskin, T. M. van Heest, and D. S. Sholl, "Can metal–organic framework materials play a useful role in large-scale carbon dioxide separations?", ChemSusChem **3**, 879–891 (2010).

[135] A. Samanta, A. Zhao, G. K. Shimizu, P. Sarkar, and R. Gupta, "Post-combustion CO 2 capture using solid sorbents: A review", Industrial and Engineering Chemistry Research **51**, 1438–1463 (2012).

[136] A. R. Millward and O. M. Yaghi, "Metal-organic frameworks with exceptionally high capacity for storage of carbon dioxide at room temperature", Journal of the American Chemical Society **127**, 17998–17999 (2005).

[137] P. L. Llewellyn, S. Bourrelly, C. Serre, Y. Filinchuk, and G. Férey, "How hydration drastically improves adsorption selectivity for co2 over ch4 in the flexible chromium terephthalate mil-53", Angewandte Chemie International Edition **45**, 7751–7754 (2006).

[138] E. Neofotistou, C. D. Malliakas, and P. N. Trikalitis, “Unprecedented sulfone-functionalized metal–organic frameworks and gas-sorption properties”, Chemistry – A European Journal **15**, 4523–4527 (2009).

[139] A. Comotti, S. Bracco, P. Sozzani, S. Horike, R. Matsuda, J. Chen, M. Takata, Y. Kubota, and S. Kitagawa, “Nanochannels of two distinct cross-sections in a porous al-based coordination polymer”, Journal of the American Chemical Society **130**, 13664–13672 (2008).

[140] H. Kim, Y. Kim, M. Yoon, S. Lim, S. M. Park, G. Seo, and K. Kim, “Highly selective carbon dioxide sorption in an organic molecular porous material”, Journal of the American Chemical Society **132**, 12200–12202 (2010).

[141] A. Phan, C. J. Doonan, F. J. Uribe-Romo, C. B. Knobler, M. O’Keeffe, and O. M. Yaghi, “Synthesis, Structure, and Carbon Dioxide Capture Properties of Zeolitic Imidazolate Frameworks”, Accounts of Chemical Research **43**, 58–67 (2010).

[142] M. Xue, Y. Liu, R. M. Schaffino, S. Xiang, X. Zhao, G.-S. Zhu, S.-L. Qiu, and B. Chen, “New prototype isoreticular metal-organic framework zn4o(fma)3 for gas storage”, Inorganic Chemistry **48**, 4649–4651 (2009).

[143] M. Tagliabue, D. Farrusseng, S. Valencia, S. Aguado, U. Ravon, C. Rizzo, A. Corma, and C. Mirodatos, “Natural gas treating by selective adsorption: material science and chemical engineering interplay”, Chemical Engineering Journal **155**, 553–566 (2009).

[144] H. Li, M. Eddaoudi, M. O’Keeffe, and O. Yaghi, “Design and synthesis of an exceptionally stable and highly porous metal- organic framework”, English (US), Nature **402**, 276–279 (1999).

[145] A. Sayari, Y. Belmabkhout, and R. Serna-Guerrero, “Flue gas treatment via co2 adsorption”, Chemical Engineering Journal **171**, Special Section: Symposium on Post-Combustion Carbon Dioxide Capture, 760–774 (2011).

[146] P. Nugent, Y. Belmabkhout, S. Burd, A. Cairns, R. Luebke, K. Forrest, T. Pham, S. Ma, B. Space, L. Wojtas, M. Eddaoudi, and M. Zaworotko, “Porous materials with optimal adsorption thermodynamics and kinetics for co2 separation”, Nature **495**, 80–84 (2013).

[147] S. R. Caskey, A. G. Wong-Foy, and A. J. Matzger, “Dramatic tuning of carbon dioxide uptake via metal substitution in a coordination polymer with cylindrical pores”, Journal of the American Chemical Society **130**, 10870–10871 (2008).

[148] N. L. Rosi, J. Kim, M. Eddaoudi, B. Chen, M. O’Keeffe, and O. M. Yaghi, “Rod packings and metal-organic frameworks constructed from rod-shaped secondary building units”, Journal of the American Chemical Society **127**, 1504–1518 (2005).

[149] J. C. Abanades, B. Arias, A. Lyngfelt, T. Mattisson, D. E. Wiley, H. Li, M. T. Ho, E. Mangano, and S. Brandani, “Emerging CO2 capture systems”, International Journal of Greenhouse Gas Control **40**, 126–166 (2015).

[150] A. L. Chaffee, G. P. Knowles, Z. Liang, J. Zhang, P. Xiao, and P. A. Webley, “CO2 capture by adsorption: Materials and process development”, International Journal of Greenhouse Gas Control **1**, 11–18 (2007).

[151] J. B. DeCoste, G. W. Peterson, B. J. Schindler, K. L. Killops, M. A. Browe, and J. J. Mahle, “The effect of water adsorption on the structure of the carboxylate containing metal–organic frameworks cu-btc, mg-mof-74, and uio-66”, J. Mater. Chem. A **1**, 11922–11932 (2013).

[152] J. Canivet, A. Fateeva, Y. Guo, B. Coasne, and D. Farrusseng, “Water adsorption in mofs: fundamentals and applications”, Chem. Soc. Rev. **43**, 5594–5617 (2014).

[153] S. Choi, J. H. Drese, and C. W. Jones, “Adsorbent materials for carbon dioxide capture from large anthropogenic point sources”, ChemSusChem **2**, 796–854 (2009).

[154] M. Pera-Titus, “Porous inorganic membranes for CO2 capture: Present and prospects”, Chemical Reviews **114**, 1413–1492 (2014).

[155] J. C. Glier and E. S. Rubin, “Assessment of solid sorbents as a competitive post-combustion co2 capture technology”, Energy Procedia **37**, GHGT-11 Proceedings of the 11th International Conference on Greenhouse Gas Control Technologies, 18-22 November 2012, Kyoto, Japan, 65–72 (2013).

[156] A. Sinha, L. A. Darunte, C. W. Jones, M. J. Realff, and Y. Kawajiri, “Systems design and economic analysis of direct air capture of co2 through temperature vacuum swing adsorption using mil-101(cr)-pei-800 and mmen-mg2(dobpdc) mof adsorbents”, Industrial & Engineering Chemistry Research **56**, 750–764 (2017).

[157] K. S. Park, Z. Ni, A. P. Côté, J. Y. Choi, R. Huang, F. J. Uribe-Romo, H. K. Chae, M. O’Keeffe, and O. M. Yaghi, “Exceptional chemical and thermal stability of zeolitic imidazolate frameworks”, Proceedings of the National Academy of Sciences **103**, 10186–10191 (2006).

[158] R. Banerjee, “High-Throughput Synthesis of Zeolitic Imidazolate Frameworks and Application to CO2 Capture”, ReVision **939**, 939–944 (2008).

[159] Y. Pan and Z. Lai, “Sharp separation of c2/c3 hydrocarbon mixtures by zeolitic imidazolate framework-8 (zif-8) membranes synthesized in aqueous solutions”, Chem. Commun. **47**, 10275–10277 (2011).

[160] Y. Pan, B. Wang, and Z. Lai, “Synthesis of ceramic hollow fiber supported zeolitic imidazolate framework-8 (zif-8) membranes with high hydrogen permeability”, Journal of Membrane Science **421-422**, 292–298 (2012).

[161] A. J. Brown, N. A. Brunelli, K. Eum, F. Rashidi, J. R. Johnson, W. J. Koros, C. W. Jones, and S. Nair, “Interfacial microfluidic processing of metal-organic framework hollow fiber membranes”, Science **345**, 72–75 (2014).

[162] K. Zhang, R. P. Lively, M. E. Dose, A. J. Brown, C. Zhang, J. Chung, S. Nair, W. J. Koros, and R. R. Chance, “Alcohol and water adsorption in zeolitic imidazolate frameworks”, Chemical Communications **49**, 3245–3247 (2013).

[163] K. Zhang, R. P. Lively, C. Zhang, W. J. Koros, and R. R. Chance, “Investigating the Intrinsic Ethanol/Water Separation Capability of ZIF-8: An Adsorption and Diffusion Study”, The Journal of Physical Chemistry C **117**, 7214–7225 (2013).

[164] K. Zhang, R. P. Lively, C. Zhang, R. R. Chance, W. J. Koros, D. S. Sholl, and S. Nair, “Exploring the framework hydrophobicity and flexibility of zif-8: from biofuel recovery to hydrocarbon separations”, The Journal of Physical Chemistry Letters **4**, 3618–3622 (2013).

[165] H. Huang, W. Zhang, D. Liu, B. Liu, G. Chen, and C. Zhong, “Effect of temperature on gas adsorption and separation in zif-8: a combined experimental and molecular simulation study”, Chemical Engineering Science **66**, 6297–6305 (2011).

[166] J. Pérez-Pellitero, H. Amrouche, F. R. Siperstein, G. Pirngruber, C. Nieto-Draghi, G. Chaplais, A. Simon-Masseron, D. Bazer-Bachi, D. Peralta, and N. Bats, "Adsorption of CO2, CH4, and N2 on zeolitic imidazolate frameworks: Experiments and simulations", Chemistry - A European Journal **16**, 1560–1571 (2010).

[167] X. Wu, J. Huang, W. Cai, and M. Jaroniec, "Force field for ZIF-8 flexible frameworks: Atomistic simulation of adsorption, diffusion of pure gases as CH4, H2, CO2 and N2", RSC Advances **4**, 16503–16511 (2014).

[168] Z. Hu, L. Zhang, and J. Jiang, "Development of a force field for zeolitic imidazolate framework-8 with structural flexibility", The Journal of Chemical Physics **136**, 244703 (2012).

[169] D. Danaci, R. Singh, P. Xiao, and P. A. Webley, "Assessment of zif materials for co2 capture from high pressure natural gas streams", Chemical Engineering Journal **280**, 486–493 (2015).

[170] X.-C. Huang, Y.-Y. Lin, J.-P. Zhang, and X.-M. Chen, "Ligand-directed strategy for zeolite-type metal–organic frameworks: zinc(ii) imidazolates with unusual zeolitic topologies", Angewandte Chemie International Edition **45**, 1557–1559 (2006).

[171] J.-P. Zhang, Y.-B. Zhang, J.-B. Lin, and X.-M. Chen, "Metal azolate frameworks: from crystal engineering to functional materials", Chemical Reviews **112**, 1001–1033 (2012).

[172] K. A. Cychosz and A. J. Matzger, "Water stability of microporous coordination polymers and the adsorption of pharmaceuticals from water", Langmuir **26**, 17198–17202 (2010).

[173] P. Küsgens, M. Rose, I. Senkovska, H. Fröde, A. Henschel, S. Siegle, and S. Kaskel, "Characterization of metal-organic frameworks by water adsorption", Microporous and Mesoporous Materials **120**, 325–330 (2009).

[174] X. Liu, Y. Li, Y. Ban, Y. Peng, H. Jin, H. Bux, L. Xu, J. Caro, and W. Yang, "Improvement of hydrothermal stability of zeolitic imidazolate frameworks", Chem. Commun. **49**, 9140–9142 (2013).

[175] C. Mottillo and T. Friščić, "Carbon dioxide sensitivity of zeolitic imidazolate frameworks", Angewandte Chemie International Edition **53**, 7471–7474 (2014).

[176] M. Jian, B. Liu, G. Zhang, R. Liu, and X. Zhang, "Adsorptive removal of arsenic from aqueous solution by zeolitic imidazolate framework-8 (ZIF-8) nanoparticles", Colloids and Surfaces A: Physicochemical and Engineering Aspects **465**, 67–76 (2015).

[177] S. H. Pang, C. Han, D. S. Sholl, C. W. Jones, and R. P. Lively, "Facet-Specific Stability of ZIF-8 in the Presence of Acid Gases Dissolved in Aqueous Solutions", Chemistry of Materials **28**, 6960–6967 (2016).

[178] T. Chokbunpiam, S. Fritzsche, C. Chmelik, J. Caro, W. Janke, and S. Hannongbua, "Gate Opening, Diffusion, and Adsorption of CO2 and N2 Mixtures in ZIF-8", Journal of Physical Chemistry C **120**, 23458–23468 (2016).

[179] D. Liu, Y. Wu, Q. Xia, Z. Li, and H. Xi, "Experimental and molecular simulation studies of CO2 adsorption on zeolitic imidazolate frameworks: ZIF-8 and amine-modified ZIF-8", Adsorption **19**, 25–37 (2013).

[180] L. Zhang, G. Wu, and J. Jiang, "Adsorption and diffusion of CO2 and CH4 in zeolitic imidazolate framework-8: Effect of structural flexibility", Journal of Physical Chemistry C **118**, 8788–8794 (2014).

[181] P. Puphasuk and T. Remsungnen, “Effect of the partial charge distributions in the ZIF-8 framework on the adsorption of CO2 as assessed by Gibbs Ensemble Monte Carlo simulations”, Chemical Physics Letters **647**, 20–25 (2016).

[182] Z. Yang, L. Liu, T. Gui, R. F. Zhou, and X. S. Chen, “Mean residence time of co2 molecules in flexible zif-8 cages explored by molecular dynamics simulations”, Chinese Journal of Chemical Physics **26**, 553–557 (2013).

[183] H. Amrouche, S. Aguado, J. Pérez-Pellitero, C. Chizallet, F. Siperstein, D. Farrusseng, N. Bats, and C. Nieto-Draghi, “Experimental and computational study of functionality impact on sodalite-zeolitic imidazolate frameworks for CO2 separation”, Journal of Physical Chemistry C **115**, 16425–16432 (2011).

[184] Z. Lei, C. Dai, and W. Song, “Adsorptive absorption: A preliminary experimental and modeling study on CO2 solubility”, Chemical Engineering Science **127**, 260–268 (2015).

[185] J. Hu, Y. Liu, J. Liu, and C. Gu, “Effects of water vapor and trace gas impurities in flue gas on CO2 capture in zeolitic imidazolate frameworksThe significant role of functional groups”, Fuel **200**, 244–251 (2017).

[186] A. Battisti, S. Taioli, and G. Garberoglio, “Zeolitic imidazolate frameworks for separation of binary mixtures of CO2, CH4, N2 and H2: A computer simulation investigation”, Microporous and Mesoporous Materials **143**, 46–53 (2011).

[187] Y. Liu, H. Liu, Y. Hu, and J. Jiang, “Density functional theory for adsorption of gas mixtures in metal-organic frameworks”, Journal of Physical Chemistry B **114**, 2820–2827 (2010).

[188] G. Ortiz, H. Nouali, C. Marichal, G. Chaplais, and J. Patarin, “Energetic performances of the metal-organic framework ZIF-8 obtained using high pressure water intrusion-extrusion experiments”, Physical Chemistry Chemical Physics **15**, 4888–4891 (2013).

[189] T. Chokbunpiam, S. Fritzsche, C. Chmelik, J. Caro, W. Janke, and S. Hannongbua, “Gate opening effect for carbon dioxide in ZIF-8 by molecular dynamics - Confirmed, but at high CO2 pressure”, Chemical Physics Letters **648**, 178–181 (2016).

[190] C. Sitprasert, F. Y. Wang, V. Rudolph, and Z. H. Zhu, “Ideal and mixture permeation selectivity of flexible prototypical zeolitic imidazolate framework - 8 Membranes”, Chemical Engineering Science **108**, 23–32 (2014).

[191] A. Gabrieli, M. Sant, P. Demontis, and G. B. Suffritti, “Fast and efficient optimization of Molecular Dynamics force fields for microporous materials: Bonded interactions via force matching”, Microporous and Mesoporous Materials **197**, 339–347 (2014).

[192] C. Zhang, J. A. Gee, D. S. Sholl, and R. P. Lively, “Crystal-Size-Dependent Structural Transitions in Nanoporous Crystals: Adsorption-Induced Transitions in ZIF-8”, The Journal of Physical Chemistry C **118**, 20727–20733 (2014).

[193] F. Tian, A. M. Mosier, A. Park, E. R. Webster, A. M. Cerro, R. S. Shine, and L. Benz, “In Situ Measurement of CO2 and H2O Adsorption by ZIF-8 Films”, Journal of Physical Chemistry C **119**, 15248–15253 (2015).

[194] H. Liu, P. Guo, T. Regueira, Z. Wang, J. Du, and G. Chen, “Irreversible Change of the Pore Structure of ZIF-8 in Carbon Dioxide Capture with Water Coexistence”, Journal of Physical Chemistry C **120**, 13287–13294 (2016).

[195] H. Zhang, M. Zhao, and Y. Lin, “Stability of zif-8 in water under ambient conditions”, Microporous and Mesoporous Materials **279**, 201–210 (2019).

[196] J. Cravillon, S. Münzer, S.-J. Lohmeier, A. Feldhoff, K. Huber, and M. Wiebcke, "Rapid Room-Temperature Synthesis and Characterization of Nanocrystals of a Prototypical Zeolitic Imidazolate Framework", Chemistry of Materials **21**, 1410–1412 (2009).

[197] S. Lazare, D. Bazer-bachi, F. Bonnier, E. Soyer, A.-a. Quoineaud, and N. Bats, "Catalysis by a non-functionalized MOF in transesterification : acido-basicity at the external surface of ZIF-8 probed by FTIR and ab initio calculations Supporting Information", J. Am. Chem. Soc., 1557–1559 (2006).

[198] M. Zhu, J. B. Jasinski, and M. A. Carreon, "Growth of zeolitic imidazolate framework-8 crystals from the solid-liquid interface", Journal of Materials Chemistry **22**, 7684–7686 (2012).

[199] Z. Li and H. C. Zeng, "Surface and Bulk Integrations of Single-Layered Au or Ag Nanoparticles onto Designated Crystal Planes {110} or {100} of ZIF-8", Chemistry of Materials **25**, 1761–1768 (2013).

[200] C. Chizallet and N. Bats, "External surface of zeolite imidazolate frameworks viewed ab initio: Multifunctionality at the organic-inorganic interface", Journal of Physical Chemistry Letters **1**, 349–353 (2010).

[201] L. Zhang, Z. Hu, and J. Jiang, "Sorption-induced structural transition of zeolitic imidazolate framework-8: A hybrid molecular simulation study", Journal of the American Chemical Society **135**, 3722–3728 (2013).

[202] J. Cravillon, C. A. Schröder, H. Bux, A. Rothkirch, J. Caro, and M. Wiebcke, "Formate modulated solvothermal synthesis of ZIF-8 investigated using time-resolved in situ X-ray diffraction and scanning electron microscopy", CrystEngComm **14**, 492–498 (2012).

[203] P. Raveendran, Y. Ikushima, and S. L. Wallen, "Polar attributes of supercritical carbon dioxide", Accounts of Chemical Research **38**, 478–485 (2005).

[204] J. M. Weber and H. Schneider, "Infrared spectra of x-·con·ar cluster anions (x=cl,br,l)", The Journal of chemical physics **120**, 10056–10061 (2004).

[205] B. Bonelli, B. Civalleri, B. Fubini, P. Ugliengo, C. O. Areán, and E. Garrone, "Experimental and quantum chemical studies on the adsorption of carbon dioxide on alkali-metal-exchanged zsm-5 zeolites", The Journal of Physical Chemistry B **104**, 10978–10988 (2000).

[206] E. Stavitski, E. A. Pidko, S. Couck, T. Remy, E. J. M. Hensen, B. M. Weckhuysen, J. Denayer, J. Gascon, and F. Kapteijn, "Complexity behind co2 capture on nh2-mil-53(al)", Langmuir **27**, 3970–3976 (2011).

[207] R. Vaidhyanathan, S. S. Iremonger, G. K. H. Shimizu, P. G. Boyd, S. Alavi, and T. K. Woo, "Direct observation and quantification of co2 binding within an amine-functionalized nanoporous solid", Science **330**, 650–653 (2010).

[208] J. G. Vitillo, M. Savonnet, G. Ricchiardi, and S. Bordiga, "Tailoring metal-organic frameworks for co2 capture: the amino effect", ChemSusChem **4**, 1281–1290 (2011).

[209] R. Boulmene, K. Boussouf, M. Prakash, N. Komiha, M. M. Al-Mogren, and M. Hochlaf, "Ab initio and dft studies on co2 interacting with zn(q+)-imidazole (q=0, 1, 2) complexes: prediction of charge transfer through sigma or pi-type models", ChemPhysChem **17**, 994–1005 (2016).

[210] B. Chang, P. Bristowe, and A. Cheetham, "Computational studies on the adsorption of co2 in the flexible perfluorinated metal–organic framework zinc 1,2-bis(4-pyridyl)ethane tetrafluoroterephthalate", Physical chemistry chemical physics : PCCP **15**, 176–182 (2012).

[211] G. Sastre, J. van den Bergh, F. Kapteijn, D. Denysenko, and D. Volkmer, "Unveiling the mechanism of selective gate-driven diffusion of co2 over n2 in mfu-4 metal-organic framework", Dalton Trans. **43**, 9612–9619 (2014).

[212] R. Q. Snurr, A. O. Yazaydin, D. Dubbeldam, and H. Frost, "Molecular modeling of adsorption and diffusion in metal-organic frameworks", in *Metal-organic frameworks: design and application* (2010).

[213] D. Frenkel and B. Smit, *Understanding molecular simulation : from algorithms to applications / daan frenkel, berend smit.* (2002).

[214] M. P. Allen and D. J. Tildesley, *Computer simulation of liquids: second edition* (2017).

[215] N. Metropolis, A. W. Rosenbluth, M. N. Rosenbluth, A. H. Teller, and E. Teller, "Equation of state calculations by fast computing machines", The Journal of Chemical Physics **21**, 1087–1092 (1953).

[216] M. Li, H.-B. Tang, J.-X. Ren, and T. M. York, "Modeling of plasma processes in the slowly diverging magnetic fields at the exit of an applied-field magnetoplasmadynamic thruster", Physics of Plasmas **20**, 103502 (2013).

[217] D. Case, I. Ben-Shalom, S. Brozell, D. Cerutti, T. Cheatham, III, V. Cruzeiro, T. Darden, R. Duke, D. Ghoreishi, M. Gilson, H. Gohlke, A. Goetz, D. Greene, R. Harris, N. Homeyer, S. Izadi, A. Kovalenko, T. Kurtzman, T. Lee, S. LeGrand, P. Li, C. Lin, J. Liu, T. Luchko, R. Luo, D. Mermelstein, K. Merz, Y. Miao, G. Monard, C. Nguyen, H. Nguyen, I. Omelyan, A. Onufriev, F. Pan, R. Qi, D. Roe, A. Roitberg, C. Sagui, S. Schott-Verdugo, J. Shen, C. Simmerling, J. Smith, R. Salomon-Ferrer, J. Swails, R. Walker, J. Wang, H. Wei, R. Wolf, X. Wu, L. Xiao, D. York, and P. Kollman, *Amber 2018*, San Francisco, 2018.

[218] B. Hess, H. Bekker, H. J. C. Berendsen, and J. G. E. M. Fraaije, "Lincs: a linear constraint solver for molecular simulations", Journal of Computational Chemistry **18**, 1463–1472 (1997).

[219] M. Abraham, D. van der Spoel, E. Lindahl, B. Hess, and GROMACS Development Team, *GROMACS User Manual version 5.1.4* (2016).

[220] G. Bussi, D. Donadio, and M. Parrinello, "Canonical sampling through velocity rescaling", The Journal of Chemical Physics **126**, 014101 (2007).

[221] D. Marx and J. Hutter, *Ab initio molecular dynamics: basic theory and advanced methods* (Cambridge University Press, 2009).

[222] J. Kohanoff, *Electronic structure calculations for solids and molecules: theory and computational methods* (Cambridge University Press, 2006).

[223] W. Koch and M. Holthausen, *A chemist's guide to density functional theory* (Wiley, 2015).

[224] R. Martin, *Electronic structure: basic theory and practical methods* (Cambridge University Press, 2020).

[225] J. P. Perdew, K. Burke, and M. Ernzerhof, "Generalized gradient approximation made simple", Phys. Rev. Lett. **77**, 3865–3868 (1996).

[226] S. Goedecker, M. Teter, and J. Hutter, “Separable dual-space gaussian pseudopotentials”, Phys. Rev. B **54**, 1703–1710 (1996).

[227] P. Hohenberg and W. Kohn, “Inhomogeneous electron gas”, Phys. Rev. **136**, B864–B871 (1964).

[228] W. Kohn and L. J. Sham, “Self-consistent equations including exchange and correlation effects”, Phys. Rev. **140**, A1133–A1138 (1965).

[229] J. C. Slater and J. C. Phillips, “Quantum Theory of Molecules and Solids Vol. 4: The Self-Consistent Field for Molecules and Solids”, Physics Today **27**, 49 (1974).

[230] A. D. Becke, “Density-functional exchange-energy approximation with correct asymptotic behavior”, Phys. Rev. A **38**, 3098–3100 (1988).

[231] C. Lee, W. Yang, and R. G. Parr, “Development of the colle-salvetti correlation-energy formula into a functional of the electron density”, Phys. Rev. B **37**, 785–789 (1988).

[232] B. Miehlich, A. Savin, H. Stoll, and H. Preuss, “Results obtained with the correlation energy density functionals of becke and lee, yang and parr”, Chemical Physics Letters **157**, 200–206 (1989).

[233] S. H. Vosko, L. Wilk, and M. Nusair, “Accurate spin-dependent electron liquid correlation energies for local spin density calculations: a critical analysis”, Canadian Journal of Physics **59**, 1200 (1980).

[234] T. H. Dunning, “Gaussian basis sets for use in correlated molecular calculations. i. the atoms boron through neon and hydrogen”, The Journal of Chemical Physics **90**, 1007–1023 (1989).

[235] A. Banerjee, N. Adams, J. Simons, and R. Shepard, “Search for stationary points on surfaces”, The Journal of Physical Chemistry **89**, 52–57 (1985).

[236] J. Simons and J. Nichols, “Strategies for walking on potential energy surfaces using local quadratic approximations”, International Journal of Quantum Chemistry **38**, 263–276 (1990).

[237] X. Li and M. J. Frisch, “Energy-represented direct inversion in the iterative subspace within a hybrid geometry optimization method”, Journal of Chemical Theory and Computation **2**, 835–839 (2006).

[238] Ö. Farkas and H. B. Schlegel, “Methods for optimizing large molecules. part iii. an improved algorithm for geometry optimization using direct inversion in the iterative subspace (gdiis)”, Phys. Chem. Chem. Phys. **4**, 11–15 (2002).

[239] C. M. Breneman and K. B. Wiberg, “Determining atom-centered monopoles from molecular electrostatic potentials. the need for high sampling density in formamide conformational analysis”, Journal of Computational Chemistry **11**, 361–373 (1990).

[240] A. J. Garza and G. E. Scuseria, “Comparison of self-consistent field convergence acceleration techniques”, The Journal of Chemical Physics **137**, 054110 (2012).

[241] S. Boys and F. Bernardi, “The calculation of small molecular interactions by the differences of separate total energies. some procedures with reduced errors”, Molecular Physics **19**, 553–566 (1970).

[242] X. Yue, A. Inoue, C.-T. Liu, and C. Fan, “The Development of Structure Model in Metallic Glasses”, en, Materials Research **20**, 326–338 (2017).

[243] H. M. Cezar, S. Canuto, and K. Coutinho, *DICE version 3.0: A Monte Carlo program for molecular liquid simulation*, 2018.

[244] M. J. Abraham, T. Murtola, R. Schulz, S. Páll, J. C. Smith, B. Hess, and E. Lindahl, "Gromacs: high performance molecular simulations through multi-level parallelism from laptops to supercomputers", SoftwareX **1-2**, 19–25 (2015).

[245] J. VandeVondele, M. Krack, F. Mohamed, M. Parrinello, T. Chassaing, and J. Hutter, "Quickstep: Fast and accurate density functional calculations using a mixed Gaussian and plane waves approach", Computer Physics Communications **167**, 103–128 (2005).

[246] M. J. Frisch, G. W. Trucks, H. B. Schlegel, G. E. Scuseria, M. A. Robb, J. R. Cheeseman, G. Scalmani, V. Barone, B. Mennucci, G. A. Petersson, H. Nakatsuji, M. Caricato, X. Li, H. P. Hratchian, A. F. Izmaylov, J. Bloino, G. Zheng, J. L. Sonnenberg, M. Hada, M. Ehara, K. Toyota, R. Fukuda, J. Hasegawa, M. Ishida, T. Nakajima, Y. Honda, O. Kitao, H. Nakai, T. Vreven, J. A. Montgomery Jr., J. E. Peralta, F. Ogliaro, M. Bearpark, J. J. Heyd, E. Brothers, K. N. Kudin, V. N. Staroverov, R. Kobayashi, J. Normand, K. Raghavachari, A. Rendell, J. C. Burant, S. S. Iyengar, J. Tomasi, M. Cossi, N. Rega, J. M. Millam, M. Klene, J. E. Knox, J. B. Cross, V. Bakken, C. Adamo, J. Jaramillo, R. Gomperts, R. E. Stratmann, O. Yazyev, A. J. Austin, R. Cammi, C. Pomelli, J. W. Ochterski, R. L. Martin, K. Morokuma, V. G. Zakrzewski, G. A. Voth, P. Salvador, J. J. Dannenberg, S. Dapprich, A. D. Daniels, Ö. Farkas, J. B. Foresman, J. V. Ortiz, J. Cioslowski, and D. J. Fox, *Gaussian09 Revision D.01*, Wallingford CT, 2013.

[247] B. Vujić and A. P. Lyubartsev, "Transferable force-field for modelling of CO2, n2, o2 and ar in all silica and na+ exchanged zeolites", Modelling and Simulation in Materials Science and Engineering **24**, 045002 (2016).

[248] H. J. Berendsen, J. R. Grigera, and T. P. Straatsma, "The missing term in effective pair potentials", Journal of Physical Chemistry **91**, 6269–6271 (1987).

[249] J. G. Harris and K. H. Yung, "Carbon dioxide's liquid-vapor coexistence curve and critical properties as predicted by a simple molecular model", Journal of Physical Chemistry **99**, 12021–12024 (1995).

[250] A. K. Rappe, C. J. Casewit, K. S. Colwell, W. A. Goddard, and W. M. Skiff, "Uff, a full periodic table force field for molecular mechanics and molecular dynamics simulations", Journal of the American Chemical Society **114**, 10024–10035 (1992).

[251] B. J. Cabral, R. Rivelino, K. Coutinho, and S. Canuto, "A first principles approach to the electronic properties of liquid and supercritical CO2", Journal of Chemical Physics **142**, 024504 (2015).

[252] H. Amrouche, B. Creton, F. Siperstein, and C. Nieto-Draghi, "Prediction of thermodynamic properties of adsorbed gases in zeolitic imidazolate frameworks", RSC Advances **2**, 6028–6035 (2012).

[253] A. U. Ortiz, A. P. Freitas, A. Boutin, A. H. Fuchs, and F.-X. Coudert, "What makes zeolitic imidazolate frameworks hydrophobic or hydrophilic? the impact of geometry and functionalization on water adsorption", Phys. Chem. Chem. Phys. **16**, 9940–9949 (2014).

[254]C. Chizallet, S. Lazare, D. Bazer-Bachi, F. Bonnier, V. Lecocq, E. Soyer, A.-A. Quoineaud, and N. Bats, "Catalysis of transesterification by a nonfunctionalized metal-organic framework: acido-basicity at the external surface of zif-8 probed by ftir and ab initio calculations", Journal of the American Chemical Society **132**, 12365–12377 (2010).

[255]C. F. Macrae, I. Sovago, S. J. Cottrell, P. T. A. Galek, P. McCabe, E. Pidcock, M. Platings, G. P. Shields, J. S. Stevens, M. Towler, and P. A. Wood, "Mercury 4.0: from visualization to analysis, design and prediction", Journal of Applied Crystallography **53**, 226–235 (2020).

[256]B. Russell, J. Villaroel, K. Sapag, and A. D. Migone, "O2 adsorption on ZIF-8: Temperature dependence of the gate-opening transition", Journal of Physical Chemistry C **118**, 28603–28608 (2014).

[257]C. O. Ania, E. García-Pérez, M. Haro, J. J. Gutiérrez-Sevillano, T. Valdés-Solís, J. B. Parra, and S. Calero, "Understanding gas-induced structural deformation of ZIF-8", Journal of Physical Chemistry Letters **3**, 1159–1164 (2012).

[258]R. Span and W. Wagner, "Equations of state for technical applications. i. simultaneously optimized functional forms for nonpolar and polar fluids", International Journal of Thermophysics **24**, 1–39 (2003).

[259]D. E. S. Santos, F. J. S. Pontes, R. D. Lins, K. Coutinho, and T. A. Soares, "Suave: a tool for analyzing curvature-dependent properties in chemical interfaces", Journal of Chemical Information and Modeling **60**, 473–484 (2020).

[260]D. Fairen-Jimenez, R. Galvelis, A. Torrisi, A. D. Gellan, M. T. Wharmby, P. A. Wright, C. Mellot-Draznieks, and T. Düren, "Flexibility and swing effect on the adsorption of energy-related gases on ZIF-8: Combined experimental and simulation study", Dalton Transactions **41**, 10752–10762 (2012).

[261]A.-K. Pusch, T. Splith, L. Moschkowitz, S. Karmakar, R. Biniwale, M. Sant, G. Suffritti, P. Demontis, J. Cravillon, E. Pantatosaki, and F. Stallmach, "Nmr studies of carbon dioxide and methane self-diffusion in zif-8 at elevated gas pressures", Adsorption **18**, 359–366 (2012).

[262]Z. Zhang, S. Xian, Q. Xia, H. Wang, Z. Li, and J. Li, "Enhancement of co2 adsorption and co2/n2 selectivity on zif-8 via postsynthetic modification", AIChE Journal **59**, 2195–2206 (2013).

[263]J. McEwen, J.-D. Hayman, and A. Ozgur Yazaydin, "A comparative study of co2, ch4 and n2 adsorption in zif-8, zeolite-13x and bpl activated carbon", Chemical Physics **412**, 72–76 (2013).

[264]M. Dudev, J. Wang, T. Dudev, and C. Lim, "Factors governing the metal coordination number in metal complexes from cambridge structural database analyses", The Journal of Physical Chemistry B **110**, 1889–1895 (2006).

[265]N. J. Ataie, Q. Q. Hoang, M. P. D. Zahniser, Y. Tu, A. Milne, G. A. Petsko, and D. Ringe, "Zinc coordination geometry and ligand binding affinity: the structural and kinetic analysis of the second-shell serine 228 residue and the methionine 180 residue of the aminopeptidase from vibrio proteolyticus", Biochemistry **47**, 7673–7683 (2008).